

This item was submitted to Loughborough University as a PhD thesis by the author and is made available in the Institutional Repository (<https://dspace.lboro.ac.uk/>) under the following Creative Commons Licence conditions.



For the full text of this licence, please go to:
<http://creativecommons.org/licenses/by-nc-nd/2.5/>

Absolute surface topography measurement with polarisation sensitive coherence scanning interferometry

By
Kanik Palodhi

A Doctoral Thesis Submitted in partial fulfilment of the requirements for the award of Doctor of
Philosophy of Loughborough University

June 2013

© Kanik Palodhi 2013

ABSTRACT

Traditionally, surface topography measurement was in the domain of quality control of engineering parts. With the advancement of manufacturing technology and affordable computational costs, different types of surfaces are produced with varied shapes and surface textures. These pose significant measurement problems, therefore, surface topography research is gaining momentum to achieve a better control of the surface. Coherence scanning interferometry (CSI) is one of the most common techniques used for measurement of surface topography. It is preferred over tactile and other non-contact techniques since it provides fast and accurate measurement with high vertical ($\sim 1 \text{ nm}$) and lateral ($\sim 1 \mu\text{m}$) resolutions over larger areas without any damage to the surface. Essentially, CSI is treated as one dimensional (1D) superposition of the light waves from an object and a reference that generates a three dimensional (3D) interferogram. Secondly, despite the advantages, there is no standard configuration of CSI that can provide absolute surface topography measurement of an engineering part with multiple materials. An effective solution to this problem will be particularly useful in the field of semiconductor and bio-related industries where chips and instruments are made of many materials.

In this Thesis, first, the CSI technique is analysed in terms of a wider theoretical framework of 3D linear filtering technique which shows the similarities among other seemingly disparate techniques such as confocal and optical coherence tomography. Due consideration to the spectral characteristic of the source and the effect of numerical aperture are given and important parameters such as vertical and lateral resolutions are computed to compare this theory with standard analysis methods. Additionally, it is shown that the 3D fringe pattern can be considered to be a superposition of a reference field and the scattered field from the top “foil-like” layer on the top the object. The scattered field from this “foil” object is dependent on the normal Fresnel reflection coefficients. Therefore, it explains the phase offset and the proportional height offset introduced by different materials, especially, metals. In an object, where multiple materials are present, each material introduces different phase to the fringe pattern and therefore, the surface topography of the entire object is altered.

To overcome this problem, the optical polarising properties of the material are exploited. A novel configuration of polarisation sensitive CSI is presented where

interferograms with orthogonal circular polarisations are recorded and analysed. The configuration, initially, needs to be calibrated with a material and after that at each point on the object, the refractive index and height offset can be calculated. Therefore, it can be dually used to identify unknown materials present on the object and also to compensate for the height offset introduced by each material to produce absolute surface topography of the entire object. The configuration provides good agreement with ellipsometric results for metals. Additionally, it retains the advantages of high vertical and lateral resolution same as other standard coherence scanning interferometers.

ACKNOWLEDGEMENTS

I offer my sincere gratitude to both the supervisors Prof. J. M. Coupland and Prof. R. K. Leach and without them this Thesis would not have been possible. Prof. Coupland has significantly contributed to this project in one way or the other. His intuitive approach to problems solving have reduced many problems to simple exercises. Prof. Leach has supported all my endeavours and has, always, extended valuable suggestions. Their attitude to life has created a lasting impression on me and my technical proficiency is a direct result of their guidance.

I would like to sincerely thank Danny Mansfield of Taylor and Hobson for providing the Mirau objective which is essential for my experiments and Prof. D. Kerr of Loughborough University for providing the frame-grabber card. I wish to thank Dr. Kavin Bass and Dr. Piotr Kaminski of CREST, Loughborough University for their help in the use of the ellipsometer.

I would also like to thank Rahul Mandal and Dr. Joshua Vande Hey and all other group members for creating a friendly and stimulating atmosphere. I should specially mention Khairul Fikri Tamrin and Dr. S. Andrew Wormald for the initial support they have provided when I joined the group.

My special thanks to Prof. Jon Petzing and Jagpal Singh for the help they provided in the metrology lab.

My sincere thanks go to EPSRC and NPL for providing the financial support to this project.

Finally, I want to express my deepest appreciation to my family for their unconditional love and support.

NOMENCLATURE

a	Number of lens elements within Mirau objective
A_0	Amplitude of the illuminating field in microellipsometry for horizontal polarisation
A_{90}	Amplitude of the illuminating field in microellipsometry for vertical polarisation
A	Analyser
$A(r)$	Total foil area
A_{xy}	The phase gap
$\langle A \rangle$	Field average of the phase gap
c	Speed of the light in vacuum
$C(x, y)$	DC term in intensity equation of microellipsometry
c_b	Constant for the block case
c_p	Constant for the pass case
D	Photodetector
D1 and D2	Diffusers
D1' and D2'	Images of D1 of D2 at the back focal plane
E^i	Illuminating field in ellipsometry
$E_p^i(r, \phi)$	p – component of the incident field in the back-focal-plane
$E_s^i(r, \phi)$	s – component of the incident field in the back-focal-plane
$E_p(r, \phi)$	p – component of the reflected fields
$E_s(r, \phi)$	s – component of the reflected fields

$E_0(r, \phi)$	Reflected field that is parallel to the incident field (microellipsometry)
$E_{90}(r, \phi)$	Reflected field for the case of vertical polarisation (microellipsometry)
$E(\vec{r})$	Complex amplitude of a monochromatic electric field complex (3 rd chapter)
$E^r(\vec{r})$	Reference field
$E^s(\vec{r})$	Scattered field coming from the object
$\tilde{E}^s(\vec{k})$	Scattered field in the spatial frequency domain
$E(\vec{r}_b)$	The field propagating from the source
$\tilde{E}_{ideal}(\vec{k})$	Ideal reconstructed field in the spatial frequency domain
$E^t(\vec{r})$	The transmitted field
E_{foil}^s	The scattered field due to foil area
E_{foil}^m	The measured field due to foil area
\vec{E}_b	The field of the block case (5 th Chapter)
$ \overline{E}_b^o $	The amplitude of the final field components passing through the analyser after it reflects from object
$ \overline{E}_b^m $	The polarised field component reflected from Mirau reflector
f	Focal distance
$f(r_x, r_y)$	The surface profile of foil
FR1, FR2	Fresnel rhombs
$G(\vec{r} - \vec{r}')$	Green's function
$\tilde{G}(\vec{k})$	Green's function in the spatial frequency domain

$\tilde{G}_{ideal}(\vec{k})$	$\tilde{G}(\vec{k})$ at a point of measurement close to the source
$G(\vec{r}_b - r_z \vec{z})$	The Green's function that describes the field at boundary
$\tilde{G}_{NA}(\vec{k})$	The measurement of the transfer function when the illumination is over the spatial frequency domain restricted by the aperture
$G_{NA}(\vec{k}_i)$	The measurement of transfer function over a single point at the edge of the back-focal-plane
$G_{NA}(\vec{r})$	The field propagated when the illumination is restricted by the aperture
$h(x, y)$	Local height on the sample surface with respect to the base plane ($z=0$)
$H_i^{mono}(\vec{r})$	Propagating field for i^{th} illumination wave due to restricted aperture
$\tilde{H}_i^{mono}(\vec{k})$	$H_i^{mono}(\vec{r})$ due to restricted aperture in k-space
$H_{CSI}^{poly}(\vec{r}, k_0)$	Point spread function (PSF) with broadband source
$H_{BS}^{mono}(\vec{r})$	Point spread function (PSF) with monochromatic source
$H_{foil}(r)$	PSF due to the foil model
$I_{mono}^m(\vec{r})$	Intensity for monochromatic illumination with restricted aperture
I_o	Background intensity due to the DC term
I_{out}	The light intensity at point P(x,y)
I_s	The light intensity at point P of the wave reflected on the sample
$I_{xy}(z)$	Intensity term
$I_i^{mono}(\vec{r})$	The overall intensity due to reconstruction for the i^{th} wave
$I_{poly}^m(\vec{r}, k_0)$	Intensity for polychromatic illumination with restricted aperture
$\tilde{I}(u, y)$	Intensity field in the spatial domain (microellipsometry)
$I_{fv}(x, y, z_0)$	The peak of the envelope for the surface topography for vertical

	polarisation
I_b	Complex analytic function of the block case
I_p	Complex analytic function of the pass case
$\tilde{I}_f(\mathbf{k})$	Frequency domain and the filtered intensity signal
$I_f(\mathbf{r})$	Noise free fringe signal (analytic function)
k	Spatial frequency
k_0	Spatial frequency
δk_0	Total k range
\bar{k}	Spatial frequency of effective wavelength
k_{max}	Maximum spatial frequency
δk_z	Axial resolution of the optical system
$\delta k_{x/y}$	Lateral resolution of the optical system
\vec{k}_i	A particular spatial frequency at the measurement point
l_1 and l_2	Amplitude brightness values of two LEDs.
L1 and L2	Collimating lenses
M_i	Characteristic constant for the instrument termed as multiplicative constant
$n(\vec{r})$	Complex refractive index of the medium
\hat{n}	The direction of outward normal
n_i	Refractive index of incident media
n_t	Refractive index of transmitted media
n_1, n_2	Refractive indices in different mediums

N_A	Numerical aperture of Zygo NewView CSI
$O(\vec{r})$	Object function
P, P1 and P2	Polarisers (collimated beams are passing through this)
$P(k)$	Frequency spectrum
$P(x,y)$	The point at the output of a two-beam interferometer
Q	Quarter wave plate
r	The radial distance from the origin of the back-focal-plane
r_p	Fresnel's reflection co-efficient for the p polarised light
r_s	Fresnel's reflection co-efficient for the s polarised light
r_0	Phase offset in Ellipsometry
R_a	Average surface roughness
$R_{expt}^{material}$	The ratio of the block to pass analytic functions
R_{expt}^{il}	The ratio of illumination constants of the block and the pass
R_{calc}^{obj}	The ratio of the complex constants of the block and the pass
R_{expt}^{mirau}	The ratio of the complex constants of the Mirau objective of the block
$S(k_0)$	The spectral variation of the source
S	An imaginary spherical boundary
\vec{r}_b	Radius at far field around the point source
r_z	The distance of point P from the origin
P	Point at which reconstructed field has been measured
t	The Fresnel amplitude transmission coefficient at normal incidence
t_p	Fresnel's transmission co-efficient for the p polarised light

t_s	Fresnel's transmission co-efficient for the s polarised light
$U^B(\vec{r})$	Reference field modified by the source terms
$\tilde{U}^B(\vec{k})$	$U^B(\vec{r})$ in spatial domain
$U^R(r_z\vec{z}, \vec{r}_b)$	The reconstructed field
$U(\vec{r})$	The source that is non-zero in the region of inhomogeneity
V	An imaginary volume at far-field (Chapter 3)
V	Fringe visibility (Chapter 2)
$W(r_x, r_y)$	Window function
\hat{x} and \hat{y}	The unit vectors along X and Y direction
X	Magnification
z	Base plane
z_b^o	Constant for the Mirau objective for the block case
z_p^o	Constant for the Mirau objective for the pass case
α	Dimensionless constant
ϵ	Dielectric constant
ρ	Ratio of the reflection coefficients in Ellipsometry
ϕ	The phase difference between the light intensities at P (Chapter 2)
$\Delta\phi_{MS}(x, y, k)$	The difference of phase changes on reflection at points P' and P'' (Chapter 2)
Δ	Ellipsometric parameter, relative phase change (Chapter 4)
Δ	Refractive index contrast (Chapter 3)
$\Delta_{foil}(r)$	The computed surface or the 'foil' model of the surface

Ψ	Ellipsometric parameters, relative amplitude change (Chapter 4)
λ_0	Wavelength of the light (Chapter 3)
λ	Wavelength of incident light
$\bar{\lambda}$	Effective wavelength
$\lambda_{min/max}$	Minimum wavelength and maximum wavelength
λ_g	Wavelength of the grating
λ_i	The effective wavelength for CSI with an oblique illumination (Chapter 4)
$\Delta\lambda$	Spectral width
θ_{xy}	The phase of the fringes at a height of h_{xy}
θ_i	Incidence angle
θ_r	Transmission angle
ν_0	Frequency of the light
$\delta(\vec{r})$	The 3D Dirac delta function
$\delta x, \delta y, \delta z$	Resolutions in X, Y and Z directions (Chapter 3)
da	Elemental aperture area of block in the back-focal-plane

ABBREVIATIONS

AFM	Atomic force microscope
BFP	Back focal plane
BS	Beam splitter
CCD	Charge coupled device
CCI	Coherence correlation interferometry
CCSM	Chromatic scanning confocal microscopy
CPM	Coherence probe microscope
CR	Coherence radar
CMOS	Complementary metal oxide semiconductor
CSI	Coherence scanning interferometry
CSM	Confocal scanning microscopy
D	Aperture stop
D'	Image of D
EM	Electron microscopy
FDA	Frequency domain analysis
FFT	Fast Fourier Transform
FPGA	Field programmable gate array
FR	Fresnel rhomb
FV	Focus variation
GDP	Gross domestic product
HIS	Height scanning interferometer
IFT	Inverse Fourier Transform

IM	Interference microscope
IR	Infra-red
LCI	Low coherence interferometry
LCP	Left circularly polarised
LCSM	Laser scanning confocal microscopy
LED	Light emitting diode
M	Mirror
MCM	Mirau correlation microscope
ME	Microellipsometry
MEMS	Micro-electro-mechanical system
MOEMS	Micro-opto-electro-mechanical system
NEMS	Nano-electro-mechanical system
NPL	National physical laboratory
NSOM	Near-field scanning optical microscope
OPD	Optical path difference
OCT	Optical coherence tomography
PBS	Pellicle beam splitter
PS-CSI	Polarisation sensitive coherence scanning interferometer
PSI	Phase shifting interferometry
PSF	Point spread function
PUPS	Pupil plane scanning white light interferometer
RCP	Right circularly polarised
SEM	Scanning electron microscope

SNR	Signal to noise ratio
SPM	Scanning probe microscope
SRWLI	Spectrally resolved white light interferometry
STM	Scanning tunnelling microscope
TEM	Transmission electron microscope
TF	Transfer function
UV	Ultra violet
VSI	Vertical scanning interferometry
WLI	White light interferometry
WLPSI	White light phase stepping interferometry
WLSI	White light scanning interferometry
WSI	Wavelength scanning interferometry
XRT	X-ray topography
2D	Two dimensional
3D	Three dimensional
4D	Four dimensional

LIST OF FIGURES

Figure 1.1 Classifications of surface metrological techniques	2
Figure 2.1 CSI instrumentation with Mirau objective	21
Figure 2.2 Different types of objective (a) Michelson, (b) Mirau and (c) Linnik	23
Figure 2.3 A typical vertical cross-section of white light fringe pattern	25
Figure 2.4 A basic interferometric set-up	25
Figure 2.5 Simulated interferometric signal with Gaussian illumination spectrum centred at 500 nm and a bandwidth of 100 nm for a low-numerical-aperture objective	27
Figure 2.6 Linear fitting to phase in FDA analysis for unambiguous height detection [43]	33
Figure 3.1 Schematic diagram of CSI	39
Figure 3.2 The Green's function in a) spatial domain (real) & b) k-space (absolute)	42
Figure 3.3 The reconstructed field due to a point source within a boundary at far-field	44
Figure 3.4 Ewald sphere and TF due to restricted N_A	46
Figure 3.5 Transfer function of CSI	50
Figure 3.6 Point spread function	51
Figure 3.7 Foil surface with reference, scattered and transmitted field	53
Figure 3.8 A CSI measurement of sinusoidal grating 8 μm pitch and 466nm amplitude (pk-pk)	56
Figure 3.9 Interferogram generated by the foil model for sinusoidal grating 8 μm pitch, 466 nm amplitude (pk-pk)	57
Figure 3.10 Interferogram generated by the foil model for sinusoidal grating 3.3 μm pitch, 466 nm amplitude (pk-pk)	57
Figure 4.1 Light beam incident on the interface of two isotropic media	61
Figure 4.2 Null ellipsometry with single wavelength	63
Figure 4.3 Geometry of the p – and s – component [15]	64
Figure 4.4 The p – and s – components of the reflected beam	65
Figure 4.5 The reflected field E_0 (horizontal polarisation) in the back-focal-plane of the objective for gold sample; (a) amplitude variation and (b) phase variation	66
Figure 4.6 Variation of the ratio in equation 4.13 around the back-focal-plane for gold with an objective of $N_A = 0.85$ (a) real, (b) imaginary, (c) absolute and (d) phase	68
Figure 4.7 Real and imaginary part of the ratio of equation 4.13 at the extreme of the aperture for $N_A = 0.85$ with refractive indices obtained from ellipsometer	69
Figure 4.8 Microellipsometry set-up	70
Figure 4.9 Interferogram modulated with carrier fringe for gold coated sample	70

Figure 4.10 Fourier domain representation of the interferogram for fixed y-coordinate	71
Figure 4.11 Experimental results of the variation of the ratio in equation 4.13 around the back-focal-plane for gold sample (a) real, (b) imaginary, (c) absolute and (d) phase	73
Figure 4.12 Polar images of the experimental results of the ratio in equation 4.13 for the gold sample, (a) the real part and (b) the imaginary part. (c) The real and imaginary parts of the ratio of equation 4.13 at the extreme of the aperture with refractive indices values obtained from microellipsometry”	74
Figure 4.13 Simplified configurations; (a) single-point, (b) whole-field [15]	77
Figure 4.14 Modified CSI system with laser illumination	78
Figure 4.15 The spatial frequency of the oblique plane wave	79
Figure 4.16 (a) Intensity along z-direction for a particular pixel and (b) absolute value of intensity along \mathbf{k}_z (peak at 16 th plane, $\mathbf{k}_z = \mathbf{k}_i$); both diagrams are for horizontal polarisations	80
Figure 4.17 Height variation in horizontal polarisation of gold interface	81
Figure 4.18 The orientations of the incident polarisations in the back-focal-plane	81
Figure 4.19 Relative height difference between gold and glass surface	82
Figure 4.20 Magnitude and phase pattern of the interferogram along z-direction for a pixel	84
Figure 4.21 Surface height map of gold interface	85
Figure 4.22 Relative height difference between gold and glass surface	85
Figure 5.1 Polarisation sensitive coherence scanning interferometer (PS-CSI)	89
Figure 5.2 Polarisation states at different positions for the block case	90
Figure 5.3 Polarisation states at different positions for the pass case	90
Figure 5.4 Image of the reflected beam after FR2 and P combination for LED1 arm and (b) image of the reflected beam after FR2 and P combination for LED2 arm	91
Figure 5.5(a) Interferogram recording in PS-CSI; (b) Resultant polarisation due to elemental area da	94
Figure 5.6 Amplitude plot w.r.t incidence angle for $r_p^o + r_s^o$	97
Figure 5.7 Phase plot w.r.t incidence angle for $r_p^o + r_s^o$	98
Figure 5.8 Amplitude plot w.r.t incidence angle for $r_p^o - r_s^o$	98
Figure 5.9 Phase plot w.r.t incidence angle for $r_p^o - r_s^o$	99
Figure 5.10 (a) The position of the actual surface, the pass surface and the block surface with respect to the white light fringe pattern along vertical axis through a pixel; (b) deviation of the surfaces for the pass and the block cases from the actual positions of surfaces for different materials (values are in nanometre)	103
Figure 5.11 (a) Recording of intensity with each vertical step height increase for pass and block, (b) total set of data for a pixel; four consecutive steps for block and the next four for pass and (c) after separating out block and pass data by choosing points from the total set mentioned above; top – pass and bottom – block	109
Figure 5.12 Real and absolute value of $I_f(x, y, z)$ for a pixel for both the pass (with higher peak) and the block	110
Figure 5.13 Experiment results of the ratio $R_{expt}^{material}$ for gold and silver sample (gold left and silver right) the magnitude (a.u.) and (b) the phase values (degrees)	112

Figure 5.14 Experiment to check the polarisation state of the beam coming out from Mirau	113
Figure 5.15 (a) Real part of the refractive indices and (b) imaginary part of refractive indices of gold – silver sample (gold on the left);(c) Real part of the refractive indices and (d) imaginary part of refractive indices of gold – aluminium (gold right) sample (theoretical values measured by ellipsometry from Table are 5.5 shown)	117
Figure 5.16 For gold-silver sample, (a) uncompensated height map, (b) compensated height map and (c) only height offset from the difference of the uncompensated and compensated height maps	119
Figure 5.17 For gold-aluminium sample, (a) uncompensated height map, (b) compensated height map and (c) only height offset from the difference of the uncompensated and compensated height maps	120
Figure 6.1 Shift of light cone for a tilt in the sample at the back focal plane	125
Figure 6.2 Actual V-groove (solid) with overestimated V-groove (dashed)	127

PUBLICATION LIST AND ORIGINAL CONTRIBUTIONS MADE

JOURNAL PAPER

Jeremy Coupland, Rahul Mandal, Kanik Palodhi, and Richard Leach, "Coherence scanning interferometry: linear theory of surface measurement," *Appl. Opt.* 52, (2013)
<http://www.opticsinfobase.org/ao/abstract.cfm?URI=ao-52-16-3662>

Part of the thesis is being considered for a patent and therefore, it is yet to be published.

INTERNATIONAL CONFERENCE PROCEEDINGS:

1. K. Palodhi, J. M. Coupland, R. K. Leach, "A linear model of fringe generation and analysis in coherence scanning interferometry", *Precision Interferometric Metrology*, ASPE, North Carolina, US, Jun 2010.
2. K. Palodhi, J. M. Coupland, R. K. Leach, "Experimental determination of the point spread function and its effect in coherence scanning interferometry", *PHOTON 10*, Southampton, UK, Aug 2010.
3. K. Palodhi, J. M. Coupland, R. K. Leach, "Measurement of complex refractive index using micro-ellipsometry and its relevance to surface measurement using coherence scanning interferometry", *Met&Props*, National Physical Laboratory, UK, Apr 2011.
4. K. Palodhi, J. M. Coupland, R. K. Leach, "Determination of the point spread function of a coherence scanning interferometer", *Met&Props*, National Physical Laboratory, UK, Apr 2011.
5. K. Palodhi, J. M. Coupland, R. K. Leach, "Absolute surface topography measurement of composite structures using coherence scanning interferometry", Como, Italy, EUSPEN, May 2011 (poster).
6. R. Mandal, K. Palodhi, J. M. Coupland, R. K. Leach, "Measurement of the point spread function in coherence scanning interferometry", *ICONTOP*, Kolkata, India, Dec 2011.
7. R. Mandal, K. Palodhi, J. M. Coupland, R. K. Leach, "Application of linear systems theory to characterize coherence scanning interferometry", *SPIE Photonics Europe*, Brussels, Apr, 2012.

In the existing literature, Coherence scanning interferometry (CSI) is mostly treated as a one dimensional (1D) superposition of a reference wave coming from the reference reflector and test wave coming from the object. Ideally, the interference fringes formed due to this superposition are three dimensional (3D) and in this thesis, CSI is treated in terms of a 3D linear filtering technique within the bounds of scalar diffraction theory. Essential parameters such as point spread function and effective wavelengths are measured from this technique to compare these with existing analysis methods.

In the later part of this thesis, the problem of height offsets arising out of the presence of dissimilar materials within an object under test is taken up and a novel rotationally symmetric polarisation sensitive CSI (PS-CSI) set-up is proposed. This can measure correct surface topography together with refractive index at each point on the object, which, essentially, enables the interferometer with a capability of an ellipsometer. We believe that the method of correct surface topography measurement using PS-CSI and the analytical treatment of the method is a first. Additionally, it retains the high vertical and lateral resolution capabilities of a CSI.

CONTENTS

<i>Abstract</i>	i
<i>Acknowledgements</i>	iii
<i>Nomenclature</i>	iv
<i>Abbreviations</i>	xi
<i>List of figures</i>	xiv
<i>Publication list and original contributions made</i>	xvii
<i>Chapter 1: Introduction and overview of coherence scanning interferometry (CSI)</i>	1
1.1 Background	1
1.2 Classification of surface metrological techniques	2
1.2.1 Contact measurement techniques	2
1.2.2 Non-contact measurement techniques	3
1.2.3 Optical measurement techniques	4
1.3 Coherence scanning interferometry (CSI)	6
1.3.1 Applications	8
1.3.1.1 Thickness measurement	8
1.3.1.2 Measurement of bio-structures	8
1.3.1.3 Topography of semiconductors	9
1.3.1.4 Measurement of high-aspect ratio structures	9
1.3.1.5 Characterisation of materials	10
1.3.2 Limitations	10
1.3.2.1 Fringe order errors	11
1.3.2.2 Multiple scattering	11
1.3.2.3 Dissimilar materials	12
1.4 Research objective and organisation of the chapters	13
1.5 Publications from the work in this thesis	14
References	16

4.1	Ellipsometry	60
4.1.1	Fresnel equations	61
4.1.2	Null ellipsometry	62
4.2	Microellipsometry	63
4.2.1	Microellipsometry set-up	69
4.2.2	Results and discussion	72
4.3	Whole-field measurement technique of phase offset by oblique illumination	76
4.3.1	Modified CSI with laser illumination	77
4.3.1.1	Result and discussion	78
4.3.2	Modified CSI with incoherent illumination	82
	Conclusion	86
	Reference	87
	<i>Chapter 5: Polarisation sensitive coherence scanning interferometry</i>	88
	Introduction	88
5.1	Experimental set-up	89
5.2	Theory of PS-CSI	92
5.2.1	Analysis of the block case	92
5.2.2	Analysis of the pass case	96
5.2.3	Evaluation of the ratio of the complex analytic functions due to block and pass cases	97
5.2.4	Calculation of the refractive indices	105
5.3	Experimental results	106
5.3.1	Details of the experiment	107
5.3.1.1	Synchronous source and vertical stage	107
5.3.1.2	Sampling rate and LED wavelength	108
5.3.2	Calculation of surface height and phase due to polarisation	108
5.3.2.1	Separation of the interferograms of the block and the pass	108
5.3.2.2	Processing of the interferograms for the block and the pass	110
5.3.3	Initial results: metallic objects	111

5.3.4	Corrections for the change in polarisation at the edge of the aperture of Mirau objective	113
5.3.5	Corrected refractive index calculation and surface height compensation	115
	Conclusion	121
	Reference	122
	<i>Chapter 6: Conclusion and future work</i>	123
	Introduction	123
6.1	Discussion of key findings	123
6.2	Future work	125
6.2.1	The effect of sample tilt	125
6.2.2	Lateral resolution	126
6.2.3	Multiple scattering	127
6.2.4	Grain orientation measurement	128
	Reference	129
	<i>Appendix</i>	130

CHAPTER 1: INTRODUCTION AND OVERVIEW OF COHERENCE SCANNING INTERFEROMETRY (CSI)

1.1 BACKGROUND

Measurement of different geometrical features of the surface in terms of variation of height with respect to a plane, are measured in surface metrology [1]. Surface finish of engineering parts remains an important aspect of quality control of different manufacturing processes such as, milling, turning and polishing. Friction can be controlled by surface finish resulting in reduction of wear and tear of the components [2, 3]. This principle is applied to different industries such as the optical industry (the surface quality of the optical components) and the automobile industry (the engine components have controlled surface texture for better performance), etc.

Advances in the manufacturing technology and the introduction of digital methods have prompted the need for better control of surface texture. Micro-electro-mechanical systems (MEMS) and nano-electro-mechanical system (NEMS) that are increasingly used in day-to-day applications need controlled surface topography. In the semi-conductor industry, surface topography is also of critical importance to increase the number of components, such as diodes and transistors, on a single chip. Next generation ultra-precision engineering and net-shape manufacturing techniques are now producing simple geometrical surfaces to complex free-form surfaces [4].

It has been proved that surface topography can be directly linked to the surface parameters such as, adhesion, gloss and biocompatibility [5, 6]. This has huge implications in the applications using biomaterials and nano-composites. In both of these cases, complex surfaces interact with each other and in certain cases, instead of a smooth surface; a specific surface texture is found to yield better results. For example, the surface texture of orthopaedic implants is found to have significant effects on the growth of cells [7]. Therefore, the

importance of surface metrology is growing in different domains of research and industry, but each application needs specific metrological solutions.

1.2 CLASSIFICATION OF SURFACE METROLOGICAL TECHNIQUES

Techniques used in surface metrology can broadly be classified used into two categories, contact and non-contact. Non-contact techniques can be again sub-divided into non-optical and optical categories depending upon the method of instrumentation, as illustrated in Figure 1.1.

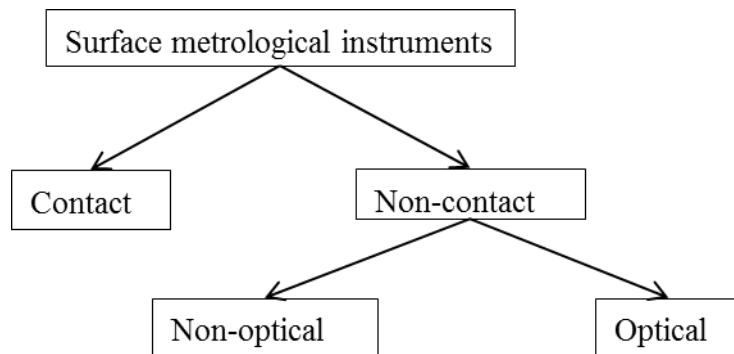


Figure 1.1 Classifications of surface metrological techniques

1.2.1 CONTACT MEASUREMENT TECHNIQUES

Traditionally, contact instruments such as the stylus, are widely used for surface metrological purposes. Recent developments of scanning probe microscopes (SPM) have increased the resolution of contact metrology to a high degree. The basic technique applied in the case of contact measurement is that a tip of a probe travels over the surface and the surface profile is measured from the displacement of the tip at each point from a reference. The movement of the tip is converted into an electrical signal by a transducer. The signal is amplified to a useful level and the data is recorded by an automated recorder or a computer. A modern stylus has lateral and vertical resolutions of the order of $1\ \mu m$ and $1\ nm$, respectively (for a chisel head stylus lateral resolution $\sim 0.2\ \mu m$). The measurement process is simple but suffers from the fact that there are chances of damage of the critically important

surface since the tip stays in contact. More importantly, it measures a one dimensional (1D) surface profile, which is time-consuming, if surface height maps need to be recorded [6, 8].

In 1982, with the invention of scanning tunnelling microscope (STM) by Binnig and Rohrer, the era of the scanning probe microscope (SPM) began [9]. In the case of SPM, a tiny probe (of tip radius $\sim 1 - 10 \text{ nm}$) moves relative to the surface staying very close to it [9]. During this movement, interaction between the probe and the surface is recorded and analysed to generate the profile. The form of the interaction can be varied and the most common of them are electrical, attractive and repulsive forces, optical, etc. [8]. STM uses a sharp conducting tip of gold or tungsten to pick up the electrical interaction with the surface once a bias voltage is applied between them [9]. The tip and the surface remain in close proximity as the tip traverses the sample and electrons from the surface tunnel through to the tip, according to the phenomenon known as quantum mechanical tunnelling. This technique generates a surface profile with excellent vertical resolution but the range of scan is limited to hundreds of microns. Therefore, high quality surface maps of relatively small areas of the surface can be reproduced.

In the case of the atomic force microscope (AFM), the interaction is via attractive and repulsive forces acting between the probe and the surface [10]. Vertical resolution can be less than a nanometre and different types of probes are used depending upon the measurement needs.

Emission of light very close to the surface is measured in the case of near-field scanning optical microscopes (NSOM) [11]. It requires a very small tip, such as a tapered ended fibre (end diameter of the order of tens of nanometre) through which the surface is illuminated and the scattered light from the surface is collected. The distance between the tip and the surface must remain less than the tip diameter to obtain images of the surface with sub-wavelength resolution.

1.2.2 NON-CONTACT MEASUREMENT TECHNIQUES

For a non-contact measurement technique, the surface is irradiated by an electromagnetic wave (such as light or X-ray) and the response is gathered by a detector system at a distance from the surface. Instead of measuring pure geometric path, these techniques measure the electromagnetic path. They can measure surface topography of an

area of the specimen quickly but are limited by diffraction. Non-contact measurement can further be sub-classified into two categories; non-optical and optical. Under the non-optical category, two techniques, electron microscopy (EM) and X-ray topography (XRT) are discussed.

Electron microscopy can be classified by two categories, scanning electron microscope (SEM) and transmission electron microscope (TEM). In case of the surface measurement, mostly SEM is used. A beam of high energy electrons is incident on the surface and the secondary electrons emitted are focussed onto a detector to form an image of the surface. The vertical resolution of the technique is of the order of 1 nm [12].

Recently, X-rays have been used to measure surface topography (XRT) [13]. A collimated beam of X-rays is incident on the surface and generates different diffracted patterns depending upon the surface microstructure of it. From these patterns surface topography is computed that works best for simple structures. It is an emerging field and the main advantage is potentially high resolution 3D images.

1.2.3 OPTICAL MEASUREMENT TECHNIQUES

Different optical measurement techniques such as focus variation (FV), confocal scanning microscopy (CSM), phase shifting interferometry (PSI), wavelength scanning interferometry (WSI) and coherence scanning interferometry (CSI) are used for surface topography. In all of these cases, either near monochromatic sources such as lasers or broadband sources such as LED are used for illumination. These techniques employ, in general, imaging and interferometric systems for recording a video of the surface. After that different computation algorithms are applied to the video frames to extract different parameters related to surface metrology. Hillman first reported that surface roughness measurements can differ significantly for optical techniques and stylus measurements [14]. Comparison of optical techniques with contact techniques is difficult due to the difference in the way of interaction of light with the surface.

Focus variation instruments measure the best focus position around the depth of focus. In this case, the sample surface is vertically scanned through the focus and a video is recorded for the entire field of view. The best focus position can be computed by finding the highest value of the standard deviation of the grey-scales for each frame of the video. The

focus variation instruments can measure high slopes of the objects but need a certain roughness of the surface to operate. It has a resolution dependent on the numerical aperture of the objective and sampling length of the filter used which provides, typically, a lateral resolution is of the order of $2\ \mu\text{m}$ and a vertical resolution of the order of $20\ \text{nm}$ [15, 64].

Confocal scanning microscopy (CSM) does not need any roughness and provides slightly better vertical resolution of the order of $10\ \text{nm}$. In case of laser CSM (LCSM), placing a pin-hole before the detector ensures that the light from the parts of object other than the focused plane is blocked. Therefore, finding the peak of the response along the vertical axis for a particular pixel provides the image plane. For building a map of the surface, a lateral scan has to be performed since in this case only a point is imaged at a time [16]. Another variant of CSM that uses a broadband light-emitting source and an objective as a chromatic probe is known as Chromatic CSM (CCSM). This probe uses chromatic aberration of the probe to focus different wavelengths at different positions on the surface e.g. blue wavelength ($400\ \text{nm}$) will be focused closer to the probe compared to the red wavelength ($700\ \text{nm}$). Due to the presence of a pin-hole before the detector, the surface is exactly focussed for a particular wavelength. This wavelength produces maximum response recorded in a spectrometer. Therefore, by finding the peak of the intensity curve for each wavelength for a particular pixel, the surface height can be measured. Again, to build a height map the surface needs to be scanned laterally. CCSM is specifically used for surface topography and texture measurements with vertical resolution of the order of $10\ \text{nm}$ [17].

Interferometric profilers claim a vertical resolution less than a nanometre [18]. Phase-shifting interferometers (PSI) can be used to obtain fast, three-dimensional profiles of surfaces with vertical resolutions of the order of a nanometre and the lateral resolution of the order of $20\ \mu\text{m}$. Determining phase in PSI typically involves sequential shifting of the optical path of the one arm (reference arm) of the interferometer relative to the other arm (test arm) by known distances. By measuring the resulting interference pattern a wrapped phase-map can be obtained. Applying a phase unwrapping method, absolute phase over the surface can be measured, but the common phase unwrapping methods presume a smooth continuous surface. This instrument is, therefore, typically limited to measurements of smooth, polished, homogeneous surfaces. Surfaces which introduce a phase shift of 2π between adjacent measurements result in phase ambiguity errors. When rougher surfaces or surfaces with dissimilar optical properties are measured, severe errors can arise [19-21].

These limitations can be overcome by using a wavelength scanning interferometer (WSI). In this case, a tunable laser source is used for illuminating the sample with multiple wavelengths together with a reference mirror so that an interference pattern for each wavelength is recorded in the CCD detector. By measuring the change of phase with respect to wave number (inverse of wavelength) the surface height for each pixel can be calculated. Another advantage of WSI is that the sample need not be mechanically moved for scanning and the height-resolution depends on the usable source bandwidth. With increase in the bandwidth higher accuracy can be obtained though, there are not many laser sources available which produce almost uniform power over a suitable wavelength range. Yamaguchi *et al* reported vertical resolution of the order of micrometres for step height measurements and they also reported measurement of diffused objects by this technique [22]. WSI is sometimes referred to as spectrally resolved white light interferometry which has also been reported as a profilometric tool [23].

With the brief descriptions of the above competing techniques, CSI, the focus of this thesis, will be described now. First there is a brief discussion of the history of CSI then the technique will be described in detail. The principles of white light interferometry are fundamental concepts of optics and have been known for many years. Michelson first used white light fringes for measuring the size of a series of step-shaped etalons in 1893, which was later compared to the wavelength of light with the international prototype meter [24]. With the advancement of electronic equipment and modern digital processing techniques, CSI is recently developed as an automated instrument using this principle.

1.3 COHERENCE SCANNING INTERFEROMETRY (CSI)

CSI is an interferometric measurement technique which provides both high vertical and lateral resolution. The heart of the optical profilometers based on CSI is the interference microscope and these types of automated profilometers began to develop much later, from the mid-1980s, after the introduction of PSI. Then, during 1987–1994, several researchers developed similar CSI instruments by incorporating a broadband source with the interference microscope but presented their techniques with different names such as,

CPM – coherence probe microscope

CSI – coherence scanning interferometry

CSM – coherence scanning microscope

CR-coherence radar

CCI – coherence correlation interferometry

MCM – Mirau correlation microscope

WLI – white light interferometry

WLSI – white light scanning interferometry

VSI – vertical scanning interferometry

HSI – height scanning interferometer [25-33], etc.

CSI has several advantages over previous approaches to profilometry. Its range is theoretically unlimited, with practical ranges easily exceeding hundreds of micrometres. It scans over the entire field rather than point to point and with stitching techniques topography of even bigger areas can be measured. The rigid design of CSI provides insulation to vibration and resonant frequencies, especially required in factory environments. The vertical resolution for CSI is of the order of 1 nm and lateral resolution depends on numerical aperture of the microscope but it can reach less than a micrometre (for example, for 100X Nikon CF IC Epi Plan DI Interferometry Objective with $N_A = 0.7$, the lateral resolution is $0.4\ \mu\text{m}$ [34]). With such high resolution and without the phase ambiguity of PSI, CSI is ideally suited for surface profiling.

CSI is essentially a low-coherence interferometer, which combines a low coherent source such as LED with an interference microscope. As the surface is vertically scanned through the focus of the interference microscope, the part of the surface in focus is superposed with the fringe pattern, which is recorded in a video. Due to the low coherence source, the fringes are localised close to the surface. In general, the maximum of the fringe intensity function closest to the surface provides the surface topography for each pixel. A detailed discussion of the working principle and theory of CSI will be presented in Chapter 2.

1.3.1 APPLICATIONS

CSI is predominantly used to measure surface profile, surface roughness and microstructures of the engineering parts [25-33], etc. In the last few years, new capabilities of CSI have been developed ranging from vibration and transient measurements to the performance testing of micro-electro-mechanical systems (MEMS) [35-37]. In addition, a few important emerging areas of measurement are discussed as follows.

1.3.1.1 THICKNESS MEASUREMENT

CSI measurements of surface topography together with coated layers of metallic and dielectric materials on different substrates are becoming popular. Kim *et al* proposed transparent film thickness measurement with topography where the multiple reflections from the upper and lower surfaces of the film were separated from the surface height using non-linear least square fitting together with frequency domain analysis [38]. Later, a spectrally resolved white light interferometer was used to measure topography with thickness of thin-layer structures with nanometre vertical resolution [39]. By using a CSI technique, employing a source in the IR region (1310 nm, bandwidth 60 nm) even the thickness of an oil-film over water can be measured with micrometre per step resolution [40].

The pupil plane scanning white light interferometric method (PUPS) designed by Zygo Corp. evaluates the thickness of the object by measuring the variation of amplitude and phase of the reflected wave from the surface at the back-focal-plane [41]. These are converted to ellipsometric parameters Δ and Ψ as a function of wavelength and incidence angle from which the thicknesses of mono or multi-layer stacks can be computed. The modifications to the usual CSI configuration are the replacement of the tube lens by a relay lens focused on the back-focal-plane and the addition of two polarizers before and after the interference microscope objective. For silicon substrates with oxide and nitride coatings, the measurement uncertainty remains around one nanometre for different thicknesses.

1.3.1.2 MEASUREMENT OF BIO-STRUCTURES

An interesting application of CSI is the measurement of the structures of complex biological tissue. In general measurement of bio-objects requires staining or other labelling techniques which can change the form of the substance, but CSI eliminates the need of that.

En face tomography, essentially a CSI technique, can be applied to the characterization of live cells and to measure their behaviours under stress [42].

1.3.1.3 TOPOGRAPHY OF SEMICONDUCTORS

A predominant use of CSI is in topography measurements in the semiconductor industries, where at every stage of manufacturing, shape and roughness measurements are required. Specifically, crystal defects and roughness of the epitaxial layers has to be monitored at all times [43-45]. Blunt reported the suitability of CSI for the roughness measurement of semiconductor wafers and showed that the CSI measurements can be compared well with AFM [43].

1.3.1.4 MEASUREMENT OF HIGH-ASPECT RATIO STRUCTURES

High aspect ratio structures, in engineering, generally refer to shapes with greater depth compared to width, such as steep V-grooves or deep trenches. Measurements of these structures pose challenges to both contact and non-contact metrological techniques. Specifically, these structures arise in case of MEMS where the dimensions of different patterns continue to scale down due to increase in wafer size and integration of new materials. This is really an extension of semiconductor topography measurements and many *ex situ* and *in situ* methods are currently being examined. The CSI technique, being non-contact with high vertical and lateral resolution, is one of the most useful techniques to measure these structures.

Mahony *et al* have outlined a number of areas in MEMS characterisation where measurement with CSI proves to be useful, such as structural analysis and deflection curve verification. The paper also illustrates that CSI can produce better trench profiles and eliminates the need to destroy a sample from the batch for investigation under SEM [46].

Montgomery *et al* have investigated the use of CSI in MOEMS structures containing deep trenches with micrometre precision, though the presence of “ghost fringes” affects the results. They have introduced certain modifications such as changing the objective from Mirau to Linnik to reduce the errors [37, 47]. Research on better post-processing algorithms are also going on in tandem. Chim *et al* have published about the pattern recognition techniques for deep trench arrays from the recordings made by CSM and CSI [48].

1.3.1.5 CHARACTERISATION OF MATERIALS

Traditionally, the method of ellipsometry is used to characterise the optical properties of materials [49, 50]. At present, in order to measure absolute surface topography of an object by CSI technique *a-priori* knowledge of the materials is required [51]. Without a-priori knowledge, surface topography of an object made of single material can be obtained but for an object with multiple materials topography is altered. In examining objects with multiple materials, specifically for metals, the brightest fringe closest to the surface will shift differently after reflection for each material resulting in surface offsets up to about 30 nm [52]. This is discussed in detail in Section 1.3.2.3.

The effect of dispersion on this phase introduction or in other words, phase change with wavelength is reported by Harasaki *et al* [53]. Dubois *et al* presented a study that shows that phase change on reflection is also affected a little (~ 10 nm) by numerical aperture [54].

Park *et al* presented a method for compensating the phase change on reflection for measuring step heights with the step and base made of separate metals by CSI technique. Essentially, after the phases from upper and bottom side of the steps are measured in quasi-monochromatic mode at two wavelengths, height compensations for each of the metals are computed [55]. This cannot be used, however, for an object where the multiple materials are distributed randomly.

1.3.2 LIMITATIONS

Despite its widespread use due to convenience and superior results over other methods of profilometry, CSI suffers a few limitations. These limitations arise out of the way light interacts with the surface or due to the way the surface topography is computed from the fringe video. Apart from the “ghost steps” that are erroneous steps of the order of half the mean wavelength generated from measuring flat objects, most of the errors due to limitations visible in objects with higher surface gradient [56]. In some of these limitation areas, active research is being pursued.

1.3.2.1 FRINGE ORDER ERRORS

Fringe order errors, more commonly, known as 2π -jumps are sudden jumps of the order of half the wavelength in topography [57]. The topography determined from CSI is proportional to the measured phase of the brightest fringe closest to the surface. Due to the inherent cyclic nature of the phase measurement, there is a fringe order ambiguity of $n \times 2\pi$, where n is any integer. In certain cases, the computation of the surface topography from fringe data fails to recognise the nature of this ambiguity, which might happen due to steep surface gradient, sharp edges or dispersion mismatch within optical component in the set-up [58]. For example, these errors are due to field dependent dispersion in the CSI optical set-up, especially, in case of Mirau and Linnik objectives or due to an object with higher surface gradient (tilt-dependent) such as sinusoidal gratings [1, 56, 57].

A similar phase jump, known as a “batwing”, can be observed in the cases of sharp edges of step heights and square gratings [1]. This is generally thought to be caused by interference between waves coming from the top and the bottom surfaces of the objects mentioned. Sometimes, errors similar to batwings can be caused by both field-dependent and tilt-dependent errors as mentioned earlier [59].

1.3.2.2 MULTIPLE SCATTERING

For objects such as V-grooves or deep trenches (high aspect ratio structures), the incident light is scattered multiple times due to the geometry of the object instead of coming back to the objective after a single scattering event. This causes erroneous geometries to be predicted for these sorts of objects, since in these cases surfaces are assumed to be weakly scattering (Born approximation) and multiple scattering is not considered [50]. This assumption holds true only for slowly varying surfaces but can hardly be justified in cases of steep surface gradients. For example, measurement of a silicon V-groove with Zygo NewView CSI with $N_A = 0.55$, computes a clear peak instead of a groove at the apex of the V-groove [60]. Lobera *et al* theoretically predicted the effect of multiple scattering for different types of artefacts such as V-grooves and step heights using 3D theory of CSI [61].

From the above articles, it is observed that multiple scattering causes an overestimation of the actual surface height. Rough surfaces can be thought of to be comprised of small V-grooves, each of which will be overestimated resulting in a significant change in

the actual topography [60, 61]. Therefore, great care should be taken while measuring high aspect ratio structures as they are prone to multiple scattering problems. In an industrial environment, scratches, digs and re-entrant features affect the measurement of surface topography as they cause multiple scattering [1].

1.3.2.3 DISSIMILAR MATERIALS

As discussed in section 1.3.1.5, examining dissimilar materials creates problems in the measurement of surface topography. Metallic surfaces introduce errors owing to their complex refractive index which shifts the brightest fringe closest to the surface [50]. For a surface made of a single material, the entire topography will shift vertically. On the other hand, for multiple materials, each material introduces different phases leading to significant errors in the measurement of topography [1, 53]. For example, an object with a chrome line deposited on glass was measured at *National Physical Laboratory* by both contact probe (NanoSurf IV) and by CSI. The contact probe measurement showed a height of 60.8 nm whereas, the CSI measurement consistently showed 37.3 nm [1]. Here, the chrome introduces a phase error which affects the topography by 23.5 nm. From the theoretical computation of the phase change, the expected height offset was about 19.5 nm, which agrees well with the measurement data, within experimental limits.

Lega *et al* reported that dissimilar materials in a single object can be measured with the PUPS techniques [41], discussed already. In this technique instead of imaging the focused plane of the objective, the back-focal-plane is imaged onto the CCD. Therefore, measuring surface topography together with material characterisation would be a two-step process, first by acquiring fringe patterns from the surface and second by acquiring the pattern in the back-focal-plane and then processing.

Rogala *et al* developed a PSI interferometer within a Twyman-Green set-up where using a polarisation pupil mask, selective transmission (vertical or horizontal) from the sample is modified. Using phase shifting technique phases are calculated for a “single” point on the sample from the fringe patterns generated by orthogonal polarisation (vertical or horizontal). Then evaluation of real part and imaginary part of refractive index together with surface height is done by using maximum likelihood technique. Results provide good estimates of the refractive index and surface topography [65].

Leonhardt *et al* published a two-part journal paper explaining a method with CSI, which they call as “interferometry for ellipso-height-topometry”. In this technique, a point in the back-focal-plane is illuminated by linearly polarised light so that an oblique parallel beam illuminates the object [62, 63]. The problem with this set-up is if the sample is tilted away from the objective (beyond maximum aperture), then a significant amount of light will be lost for rough surfaces and for smooth surfaces there won't be any light coming back to the objective. Therefore, this set-up has limited usage and the user has to be careful about the tilt setting of this variant of CSI. This will be discussed in detail in Chapter 4 and subsequent chapters.

1.4 RESEARCH OBJECTIVE AND ORGANISATION OF THE CHAPTERS

In the previous section, the effect of dissimilar materials on CSI topography measurements has been presented. Although some attempts have been made to develop a solution, but they either need *a-priori* knowledge of the sample or there are restrictions on the object orientation and optical set-up. Therefore, there is a need for an instrument which can create a true surface height map of a composite sample (an object with dissimilar materials). For this purpose complex refractive index has to be calculated at each point on the surface.

A novel rotationally symmetric polarisation sensitive CSI set-up is proposed here, which can measure surface topography together with complex refractive index at each point on the sample. There is no restriction on the orientation of the sample or the need for specific directional illumination in this case. This set-up uses orthogonal circular polarised illumination and measures the change in amplitude and phase in the reflected fringe pattern from the sample to obtain the necessary information. This effectively combines an interferometer with the capabilities of an ellipsometer and this, we believe, is a first of its kind. The lateral and vertical resolution achieved in this set-up is of the order of $1\ \mu m$ and $1\ nm$, respectively. It is used not only to generate the material information of the sample but to compensate for the height offset made to represent true surface topography.

In the next chapter (Chapter 2), a brief introduction to the theory of CSI that is prevalent in the literature will be discussed. An overview of the CSI set-up and different techniques of surface topography computation will be discussed. In Chapter 3, CSI will be

described in terms of three dimensional imaging starting from Helmholtz equation assuming a weakly scattering approximation. A brief theory of behaviour of the smoothly varying surface will also be discussed, which is termed as “foil model”. In Chapter 4, the concept of height offset for metallic surfaces is introduced. A polarisation sensitive microellipsometry set-up together with its results will then be presented. Next, a CSI configuration with an oblique illumination set-up is described where a gold coated sample on a glass substrate is examined and height offset for gold is measured. In Chapter 5, the theory and experiment of the polarisation sensitive CSI set-up is described. In this case with two different composite objects, the surface topography with height offset and height compensation will be presented. Finally, Chapter 6 concludes by summarising the findings of the project and describes the key features of the entire project.

1.5 PUBLICATIONS FROM THE WORK IN THIS THESIS

JOURNAL PAPER

Jeremy Coupland, Rahul Mandal, Kanik Palodhi, and Richard Leach, "Coherence scanning interferometry: linear theory of surface measurement," *Appl. Opt.* 52, (2013) <http://www.opticsinfobase.org/ao/abstract.cfm?URI=ao-52-16-3662>

Part of the thesis is being considered for a patent and therefore, it is yet to be published.

INTERNATIONAL CONFERENCE PROCEEDINGS:

1. K. Palodhi, J. M. Coupland, R. K. Leach, “A linear model of fringe generation and analysis in coherence scanning interferometry”, Precision Interferometric Metrology, ASPE, North Carolina, US, Jun 2010.
2. K. Palodhi, J. M. Coupland, R. K. Leach, “Experimental determination of the point spread function and its effect in coherence scanning interferometry”, PHOTON 10, Southampton, UK, Aug 2010.
3. K. Palodhi, J. M. Coupland, R. K. Leach, “Measurement of complex refractive index using micro-ellipsometry and its relevance to surface measurement using coherence scanning interferometry”, Met&Props, National Physical Laboratory, UK, Apr 2011.
4. K. Palodhi, J. M. Coupland, R. K. Leach, “Determination of the point spread function

of a coherence scanning interferometer”, Met&Props, National Physical Laboratory, UK, Apr 2011.

5. K. Palodhi, J. M. Coupland, R. K. Leach, “Absolute surface topography measurement of composite structures using coherence scanning interferometry”, Como, Italy, EUSPEN, May 2011 (poster).

6. R. Mandal, K. Palodhi, J. M. Coupland, R. K. Leach, “Measurement of the point spread function in coherence scanning interferometry”, ICONTOP, Kolkata, India, Dec 2011.

7. R. Mandal, K. Palodhi, J. M. Coupland, R. K. Leach, “Application of linear systems theory to characterize coherence scanning interferometry”, SPIE Photonics Europe, Brussels, Apr, 2012.

The conference proceeding in PHOTON 10, 2010 (No. 2) is not included in the thesis since the work of experimental determination of PSF was later not continued by me and is taken up by Rahul Mandal, another member of our group. The proceedings presented the initial results of PSF measurement using Ruby balls used in Coordinate measuring machines (CMM).

The proceeding presented in Met&Props, 2011 (No. 4), primarily discussed the theoretical treatment of 3D linear filtering technique used for CSI and also presents some of the experimental results. The proceeding presented in ICONTOP, 2011 (No. 6) is on the other hand is predominantly based on the experimental results.

REFERENCES

1. R. K. Leach, Measurement good practice guide no. 37: The measurement of surface texture using stylus instruments (National Physical Laboratory, 2001).
2. X. Jiang, P. Scott, D. J. Whitehouse and L. Blunt, "Paradigm shifts in surface metrology: Part I. Historical philosophy", Proceedings of The Royal Society A, 463, 2085, (2007).
3. R. K. Leach, "Introduction to surface texture measurement" in *Optical measurement of surface topography*, R. K. Leach ed. (Springer, 2011).
4. X. Jiang, P. Scott, D. J. Whitehouse and L. Blunt, "Paradigm shifts in surface metrology: Part II. The current shift", Proceedings of The Royal Society A, 463, 2085 (2007).
5. H. Assender, V. Bliznyuk and K. Porfyrakis, "How surface topography relates to materials' properties", Science, 297, 5583 (2002).
6. D. J. Whitehouse, Handbook of surface and nanometrology, 2nd ed. (Boca Raton, FL: CRC Press, 2011).
7. A. Curtis and C. Wilkinson, "Topographical control of cells", Biomaterials, 18 (1997), 1573-1583.
8. R. K. Leach, Fundamental principle of nanometrology, 1st ed. (Elsevier, 2010)
9. G. Binnig and H. Rohrer, "Reprint: Scanning tunnelling microscopy", IBM Journal of Research and Development, 44, 1/2 (2000), 279-293.
10. G. Binnig and C. F. Quate, "Atomic force microscope", Physical Review Letters, 56, 9 (1986).
11. E. Betzig and J. K. Trautman, "Near-Field optics: microscopy, spectroscopy and surface modification beyond the diffraction Limit", Science, 257 (1992), 189-195.
12. P. J. Goodhew and F. J. Humphreys, Electron microscopy and analysis, 2nd ed. (Taylor and Francis, 1988)
13. D. R. Black and G. G. Long, NIST Recommended Practice Guide: X-Ray Topography, Special Publication 960-10 (National Institute of Standards and Technology, 2004).
14. W. Hillmann, "Surface profiles obtained by means of optical methods – are they true representations of the real surface", Annals CIRP, 39 (1990), 581-583.
15. Franz Helml, "Focus variation instruments", in *Optical measurement of surface topography*, R. K. Leach ed. (Springer, 2011).
16. J. Schmit, K. Creath, and J. C. Wyant, "Surface Profilers, Multiple Wavelength and White Light Interferometry", in *Optical shop testing*, D. Malacara ed. (John Wiley & Sons, 2007).
17. François Blateyron, "Chromatic confocal microscopes", in *Optical measurement of surface topography*, R. K. Leach ed. (Springer, 2011).
18. Zygo Corp., Technical Manual: NewView 5000.
19. B. Bhushan, J.C. Wyant, and C.L. Koliopoulos, "Measurement of surface topography of magnetic tapes by Mirau interferometry", Applied Optics, 24 (1985), 1489-1497.
20. J. C. Wyant, C. L. Koliopoulos, B. Bhushan, and O. E. George, "An optical profiler for surface characterization of magnetic media", ASLE Transactions, 27 (1984), 101-113.
21. J. C. Wyant and K. Creath, "Advances in interferometric optical profiling", International Journal of Machine Tools and Manufacture, 32 (1992), 5-10.

22. I. Yamaguchi and A. Yamamoto, "Surface profilometry by wavelength scanning interferometry", *Optical Engineering*, 39, 1 (2000), 40–46.
23. J. Calatroni, A. L. Guerrero, C. Sainz, and R. Esacalona, "Spectrally-resolved white light interferometry as a profilometry tool", *Optics and Laser Technology*, 28 (1996), 485-489.
24. H.J. Tiziani, "Optical Metrology of Engineering Surfaces: Scopes and Trends", in *Optical Measurement Techniques and Applications*, P.K. Rastogi ed. (Artech House Inc., 1997).
25. N. Balasubramanian, "Optical system for surface topography measurement", US Patent 4340306 (1982).
26. B. Bowe and V. Toal, "White light interferometric surface profiler", *Optical Engineering*, 37 (1998), 1796-1799.
27. P. J. Caber, "Interferometric profiler for rough surfaces", *Applied Optics*, 32 (1993), 3438 -3441.
28. B. L. Danielson and C. Y. Boisrobert, "Absolute optical ranging using low coherence interferometry", *Applied Optics*, 30 (1991), 2975-2979.
29. P. de Groot and J. W. Kramer, "Height scanning interferometry method and apparatus including phase gas analysis", US Patent 6775006 (2004).
30. L. Deck and P. de Groot, "High-speed noncontact profiler based on scanning white-light interferometry", *Applied Optics*, 33, 31 (1994), 7334-7338.
31. T. Dresel, G. Häusler, and H. Venzke, "Three-dimensional sensing of rough surfaces by coherence radar", *Applied Optics*, 31, 7 (1992), 919-925.
32. G. S. Kino and S. S. Chim, "Mirau correlation microscope", *Applied Optics*, 29, 26 (1990), 3775-3783.
33. B.S. Lee and T.C. Strand, "Profilometry with a coherence scanning microscope", *Applied Optics*, 29, 26 (1990), 3784 -3788.
34. Edmund Optics, Catalog of precision optical components, (Edmund Optics, 2012).
35. A. Bosseboeuf and S. Petitgrand, "Characterization of the static and dynamic behaviour of M(O)EMS by optical techniques: status and trends", *Journal of Micromechanics and Microengineering*, 13 (2003), S23-S33.
36. V. S. Damian, M. Bojan, P. Schiopu, I. Iordache, B. Ionita, and D. Apostol, "White light interferometry applications in nanometrology," in *Advanced topics in Optoelectronics, Microelectronics and Nanotechnologies IV*, P. Schiopu, G. Caruntu, and A. Manea eds., (SPIE, 2009).
37. P. C. Montgomery, F. Anstotz, G. Johnson, and R. Kiefer, "Real time surface morphology analysis of semiconductor materials and devices using 4D interference microscopy", *Journal of Materials Science: Materials in Electronics*, 19 (2007), 194-198.
38. S. Kim and G. Kim, "Thickness-profile measurement of transparent thin-film layers by white-light scanning interferometry", *Applied Optics*, 38, 28 (1999), 5968-5973.
39. Y. Ghim and S. Kim, "Spectrally resolved white-light interferometry for 3D inspection of a thin-film layer structure", *Applied optics*, 48, 4 (2009), 799-803.
40. C. Sun, L. Yu, Y. Sun, and Q. Yu, "Scanning white-light interferometer for measurement of the thickness of a transparent oil film on water," *Applied Optics*, 44, 25 (2005), 5202-5205.
41. X. C. de Lega and P. de Groot, "Characterization of materials and film stacks for accurate surface topography measurement using a white-light optical profiler", in

- Optical Micro- and Nanometrology in Microsystems Technology II*, W. O. C. Gorecki and A. K. Asundi eds., SPIE, 6995 (2008), 69950 P1 - P9.
42. A. Dubois, G. Moneron, K. Grieve, and A. C. Boccara, "High-resolution three-dimensional imaging inside biological media using white-light interference microscopy", *Proc. SPIE*, 5140 (2003), 43-50.
 43. R. T. Blunt, "White Light Interferometry – a production worthy technique for measuring surface roughness on semiconductor wafers", CS Mantech Conference, Vancouver, British Columbia, Canada (2006), 59-62.
 44. P. C. Montgomery, J. Fillard, N. Tchandjou, and S. M. Ardisasmita, "Three-dimensional nanoprofilng of semiconductor surfaces", in *Optical testing and metrology III: Recent advances in industrial optical inspection*, C.P. Grover ed., San Diego, CA, USA, *Proc. SPIE* (1991), 515-524.
 45. P.C. Montgomery and J. Fillard, "Peak fringe scanning microscopy: submicron 3D measurement of semiconductor components", in *Interferometry: techniques and analysis*, G. M. Brown, O. Y. Kwon, M. Kujawinska, and G. T. Reid eds., San Diego, CA, USA, *Proc. SPIE* (1993), 12-23.
 46. C. O. Mahony, M. Hill, M. Brunet, R. Duane, and A. Mathewson, "Characterization of micromechanical structures using white-light interferometry," *Measurement Science and Technology*, 14 (2003), 1807-1814.
 47. P.C. Montgomery, "The metrology of a miniature FT spectrometer MOEMS device using white light scanning interference microscopy," *Thin Solid Films*, 450 (2004), 79-83.
 48. S.S. Chim and G.S. Kino, "Optical pattern recognition measurements of trench arrays with submicrometer dimensions," *Applied Optics*, 33, 4 (1994), 678-685.
 49. M. Born and E. Wolf, *Principles of optics*, (Cambridge, 1999).
 50. Hiroyuki Fujiwara, *Spectroscopic ellipsometry*, (John Wiley & Sons, Ltd, 2003).
 51. K. Matsui, S. Kawata, "Fringe-scanning white-light microscope for surface profile measurement and material identification", *Proc. SPIE* 1720 (1992), 124-132
 52. K. Palodhi, J. M. Coupland and R. K. Leach, "Measurement of complex refractive index using micro-ellipsometry and its relevance to surface measurement using coherence scanning interferometry", *Met&Props*, National Physical Laboratory, UK (2011).
 53. A. Harasaki, J. Schmit and J. C. Wyant, "Offset of coherent envelope position due to phase change on reflection", *Applied Optics*, 40, 13 (2001), 2102-2106
 54. A. Dubois, "Effects of phase change on reflection in phase-measuring interference microscopy", *Applied Optics*, 43, 7 (2004), 1503-1507
 55. M. C. Park and S. W. Kim, "Compensation of phase change on reflection in white-light interferometry for step height measurement," *Optics letters*, 26, 7 (2001), 420-422.
 56. A. Prortner and J. Schwider, "Dispersion error in white-light Linnik interferometers and its implications for evaluation procedures", *Applied Optics*, 40, 34 (2001), 6223-6228
 57. F. Gao, R. K. Leach, J. Petzing and J. Coupland, "Surface measurement errors using commercial scanning white light interferometers", *Measurement science and technology*, 19, 015303 (2008).
 58. P. de Groot, X. C. de Lega, J. Kramer and M. Turzhitsky, "Determination of fringe order in white-light interference microscopy," *Applied Optics*, 41, 22 (2002), 4571-4578.

59. P. Lehmann, "Systematic effects in coherence peak and phase evaluation of signals obtained with a vertical scanning white-light Mirau interferometer", in *Optical micro- and nanometrology in microsystems technology*, C. Gorecki, A. K. Asundi, and W. Osten, eds., Proc. SPIE (2006), 618811-1 – 618811-11.
60. F. Gao, J. M. Coupland and J. Petzing, "V-Groove Measurements using White Light Interferometry", Photon06, Manchester (2006).
61. J. M. Coupland and J. Lobera, "Measurement of steep surfaces using white light interferometry, *Strain*, 46, 1(2010), 69-78.
62. K. Leonhardt, U. Droste and H. Tiziani, "Interferometry for ellipso-height-topometry Part 1: Coherence scanning on the base of spatial coherence", *Optik - International Journal for Light and Electron Optics*, 113, 12 (2003), 513-519.
63. K. Leonhardt, "Interferometry for ellipso-height-topometry Part 2: Measurement of the ellipsometric data, material identification, and correction of the measured height", *Optik*, 121 (2010), 623-632.
64. F. Hiersemenzel, J. Petzing, R. K. Leach, F. Helmli and J. Singh, "Areal texture and angle measurements of tilted surfaces using focus variation methods", *International Conference on Surface Metrology*, Annecy, France, (2012).
65. E. W Rogala and H. H. Barrett, "Phase-shifting interferometer/ellipsometer capable of measuring the complex index of refraction and the surface profile of a test surface", *Journal of the Optical Society of America A*, 15, 2, (1998), 538-548.

CHAPTER 2: CSI – THEORY AND FRINGE ANALYSIS TECHNIQUES

INTRODUCTION

CSI systems are actually part of a broader range of instruments that can be termed as low-coherence interferometry (LCI). The essential idea of low-coherence interferometry is that the reference surface within an interference microscope (IM) operated with a broadband light source generates a localised fringe pattern. This fringe pattern is superposed with the image of the object, which in turn, enables the localization of that surface that is identified with a particular depth range.

In this Chapter, the physical construction and the working principle of CSI is going to be discussed. CSI instrumentation is similar to a microscope set-up with the normal objective replaced by a compact interferometer, known as the interferometric objective. This is the heart of CSI instrumentation, from which both the object and the reference beams are derived. A video of the image of the sample superposed with the fringe pattern is acquired via a camera, as the sample is scanned through the focus. Later, the video is processed digitally to produce the surface map, details of which are presented in section 2.3.

2.1 CSI: PHYSICAL CONSTRUCTION

CSI combines vertical scanning techniques with 2D optical interferometry to achieve a three-dimensional (3D) surface measurement. It uses a source with broadband spectrum that is sometimes referred to as “white light source”, such as an LED or a tungsten lamp. This forms a part of an illumination arrangement followed by the interferometric objective (Mirau) through which the sample is illuminated as shown in Figure 2.1. By amplitude division of the incident light beam with a beam splitter within the Mirau objective, an object beam and a reference beam are generated. The reflected beams from both the object and a reference mirror recombine to produce an interference pattern, as the objective is focused onto the sample. This interference pattern (interferogram) is typically recorded with a CCD camera. A measurement, typically, consists of recording the fringe pattern generated at various heights. With the movement of a vertical stage, the sample is scanned through the focus of the interferometric objective (interferometer), as shown in Figure 2.1. The relative difference of

the position between the reference inside the interferometric objective and the object generates an optical path difference (OPD). Essentially, a set of 3D interferograms taken over a range of OPD between the object and reference light beams are acquired over the entire field of view during the vertical scan [1-9].

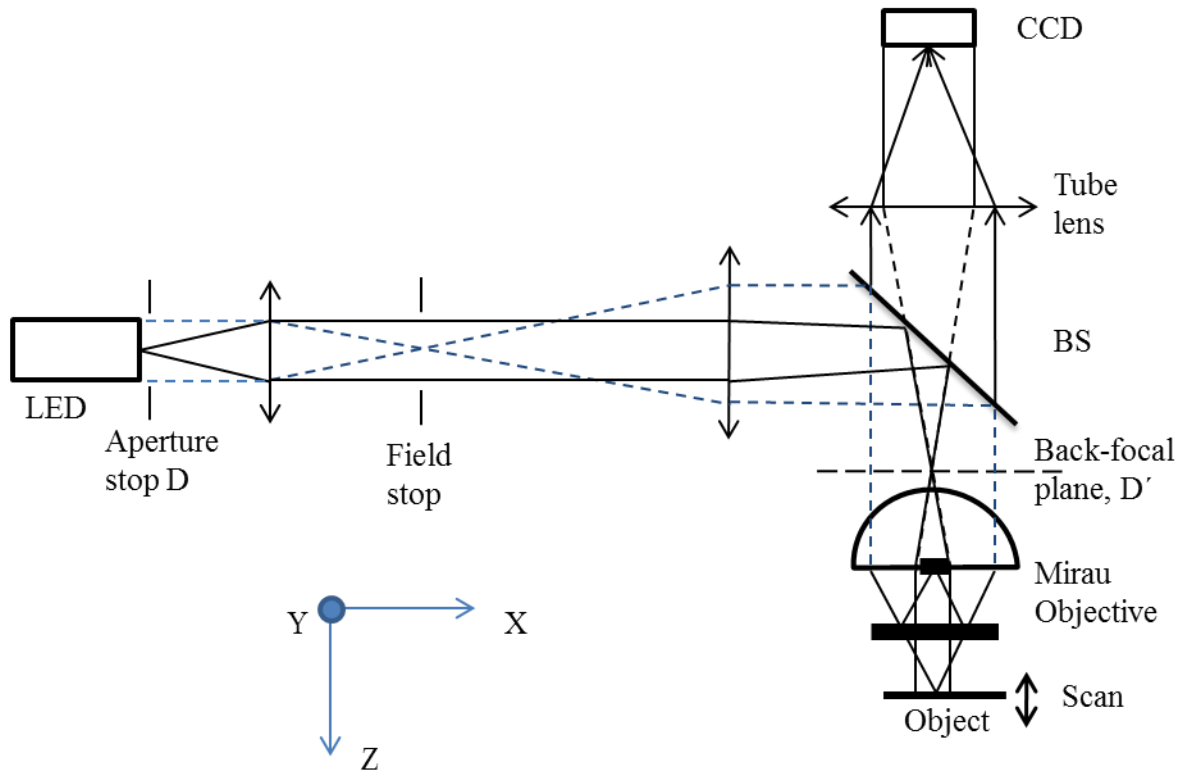


Figure 2.1 CSI instrumentation with Mirau objective

Depending upon the surface topography of the object, various parts of the object come to focus at different points of the scan. From the OPD and the positions of the focus, representative points of surface topography can be computed using various fringe pattern demodulation techniques. Next, the most important constituents of CSI, the sources, the objectives and the camera, will be discussed.

2.1.1 LIGHT SOURCES

For CSI measurements, the main idea is to use a low coherence source so that the interference fringes are localised very close to the focus of the objective. The choice of the

light source is guided by its central wavelength, its coherence length, the light power needed, and in certain cases, its pulsing capabilities. Generally, visible light sources are used, although interference microscopy in the deep-UV range was demonstrated recently [10, 11]. However, highly coherent laser sources are often avoided, as they tend to generate speckle and parasitic fringes, which degrade the measurements. Typically, a tungsten halogen white light source with band-pass-filter is the most common choice, but LEDs with broad spectrum (100 nm – 150 nm) are an interesting alternative. LEDs are now available at low cost with various wavelengths in the UV-visible-near-infrared range. In addition, they can easily be pulsed and have a low response time (20–50 ns) that is suitable for stroboscopic measurements [12, 13].

Generally speaking, as the signal-to-noise ratio of many optical detectors is proportional to the square root of light intensity, the highest possible light power must be used. With these sources, the coherence lengths are of the order of 3 μm which is suitable for most smooth surfaces with average surface roughness $R_a \sim 10 \text{ nm}$, such as polished optical surfaces measured. For rough surfaces or surfaces with higher slope angles such as engine parts or unpolished engineering parts ($R_a \sim 100 \text{ nm}$), the coherence length of the source needs to be increased. This can be achieved by a narrow-band optical filter ($\sim 40 \text{ nm}$) inserted in front of the source or by using a narrow-band LED, which increases the coherence length up to 10 μm [13].

2.1.2. INTERFEROMETRIC OBJECTIVE

Several types of interferometric objectives have been developed based on the configurations of Michelson, Mirau and Linnik interferometers. Interferometric objectives are generally composed of a microscope objective and a miniaturized interferometer placed within the objective to minimize the optical paths in the interferometer arms and obtain a high lateral resolution ($\sim 1 \mu\text{m}$). The sample acts as the second surface of a two-beam interferometer so that the interference between two waves can take place. In this way, their spatial coherence properties can be maintained and for this reason sometimes an IM is also called a coherence microscope [9].

Michelson-type interferometric objectives as shown in Figure 2.1(a) are of low magnifications ($\leq 5\text{X}$) and an optional compensator plate is used in the reference arm. The objective needs to be corrected for optical aberrations related to plate insertion. Mirau-type

interferometric objectives, as shown in Figure 2.2(b), are preferred for intermediate magnifications (10X–50X) because they are very compact. The disadvantage of Mirau objective is that the reference mirror is in the path of the image.

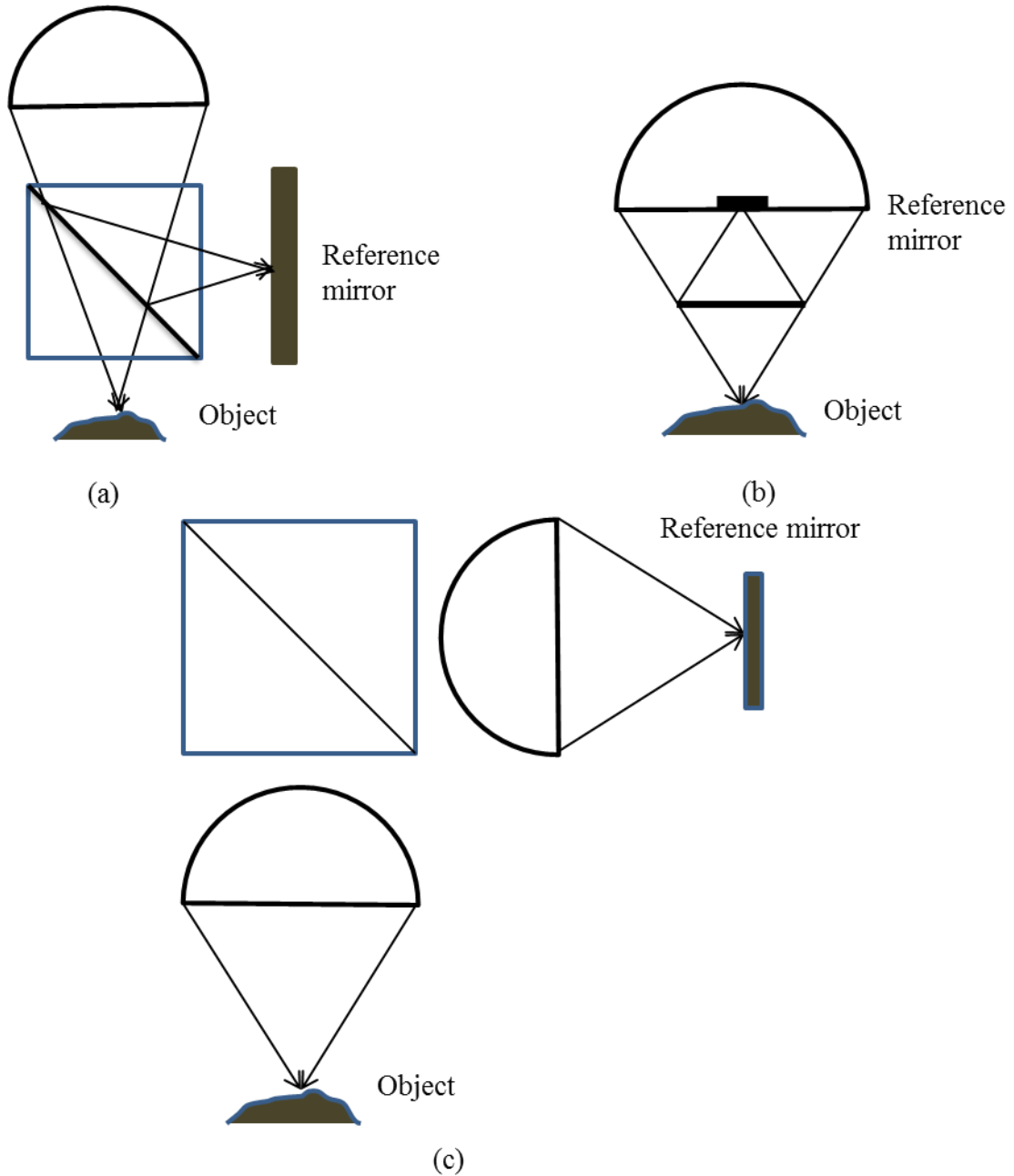


Figure 2.2 Different types of objectives (a) Michelson, (b) Mirau and (c) Linnik

Linnik interferometers, as shown in Figure 2.2(c), are based on two objectives used for the reference and the test arms with matched wave fronts and chromatic aberrations. Due

to the stringent requirements, they are more expensive. They are also quite difficult to align and tend to be heavier. The advantages are that they provide high magnifications (100X–200X) with the highest lateral resolution and the largest working distance.

One of the main requirements of an interferometric objective is that it should be compensated for dispersion for the two arms [14]. In Mirau and Linnik (two identical objectives) interferometers, the same objective is traversed by the object and reference beam, so chromatic aberrations and spherical aberrations of the objective have a small effect on the interference pattern [13, 15]. Michelson and Mirau objectives are less sensitive to external disturbances than Linnik interferometers, because they have short optical paths and are lighter. Michelson, Mirau, and Linnik interferometers can be used with both coherent and low-coherence illumination.

2.1.3 CAMERA

In general, a charged coupled device (CCD) is used for recording the data, which lends itself easily to digital computation. There are different resolutions of settings depending upon the mode used starting from 160 X 120 up to megapixels of array size. For higher resolutions, more pixels (320 X 240, 640 X 480, etc.) have to be used but that would also increase the processing time. Therefore, knowledge about the sample would aid the selection of the mode [13]. Essentially, the pixel size acts as a spatial sampling device and this sets a limit of two pixels per fringe on the screen.

2.2 FRINGE FORMATION

Surface profile of the object is calculated from the recorded interference fringes formed during a vertical scan. Figure 2.3 shows a typical cross-section along vertical direction (Z-X) taken from the scan of a flat polished artefact. The interference fringes are created from the interaction of the field scattered from the object and the reflected from the reference surface. The sample is scanned relative to the reference surface and the analysis of the data can be considered on a pixel to pixel basis, from intensity changes stored in the computer memory for each pixel on a plane by plane basis, as shown in Figure 2.3.

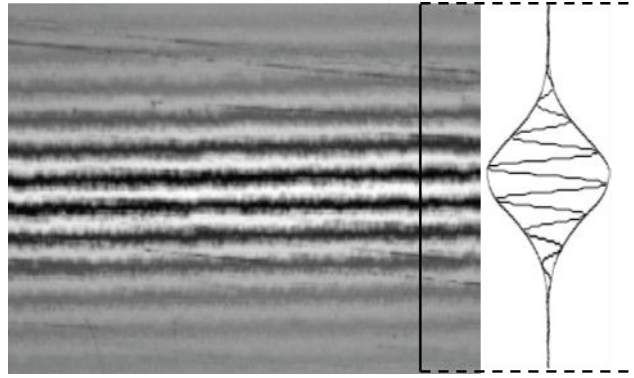


Figure 2.3 A typical vertical cross-section of white light fringe pattern

The conditions for interference require that the object and reference fields must have a degree of mutual coherence. Use of a white light (broadband and distributed) source limits the coherence length, and therefore, the path difference between the object and the reference has to be closely matched to obtain a fringe pattern. The envelope of the interference fringes can be thought of as a measure of the mutual coherence of the fields in the direction of the scan. The recorded intensity pattern or the interference pattern is due to the superposition of the scattered and the reference beams in all angles and all wavelengths. A basic interferometer is illustrated in Figure 2.4 which is used to develop the basic theory of CSI.

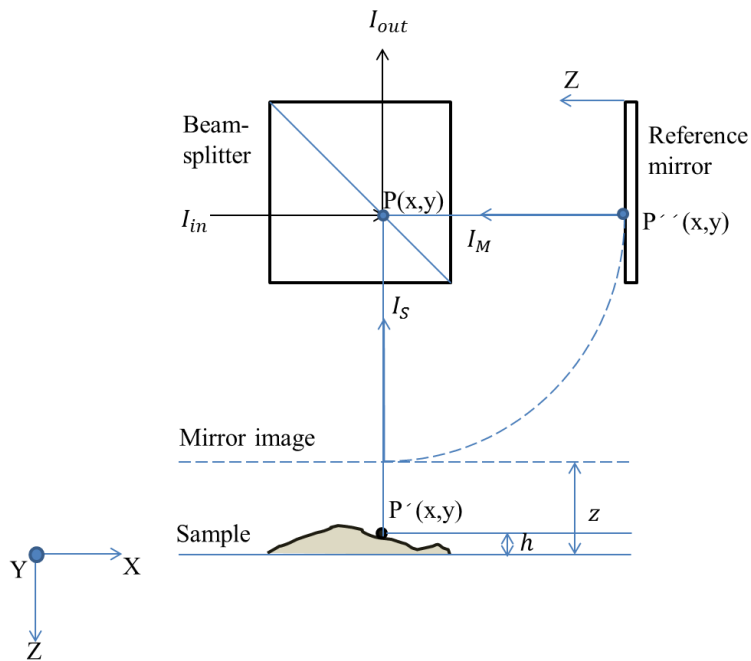


Figure 2.4 A basic interferometric set-up

The light intensity I_{out} at point P(x,y), as shown in Figure 2.4, at the output of a two-beam interferometer with a monochromatic light source of wavelength λ is given by the following well-known equation,

$$I_{out} = I_M + I_S + 2\sqrt{I_M I_S} \cos \phi \quad (2.1)$$

Where I_M and I_S are the light intensities at point P of the waves reflected on the reference mirror and on the sample, respectively, and ϕ is their phase difference. By considering propagation and reflection of these waves (Figure 2.4), it can be easily found that, the phase difference between these two waves at point P(x,y) is given by,

$$\phi(x, y, z, k) = 4\pi k[h(x, y) - z] + \Delta\phi_{MS}(x, y, k) \quad (2.2)$$

where, $h(x, y)$ is the local height on the sample surface with respect to the base plane ($z = 0$), $\Delta\phi_{MS}(x, y, k) = \phi_M - \phi_S$ is the difference of the phase changes on reflection at points P' and P'' and $k = 1/\lambda$ is the wavenumber.

By combining these equations,

$$I_{out}(x, y, z, k) = I_o(x, y, z)[1 + V(z) \cos\{4\pi k(h(x, y) - z) + \Delta\phi_{MS}(x, y, k)\}] \quad (2.3)$$

where, $I_o = I_M + I_S$ is the background intensity and $V = \frac{2\sqrt{I_M I_S}}{I_M + I_S}$ is known as fringe visibility which depends on the intensities of the two components and the degree of coherence.

When a two-beam interferometer is illuminated by a broadband light source, equations 2.1 – 2.3 must be modified to account for partial temporal coherence of the light source [14, 16, 17]. The intensity at the output of the interferometer can generally be put in the following form,

$$I(x, y, z) = \int_{-\infty}^{\infty} S(k) I_o [1 + V \cos[4\pi k(h - z) + \Delta\phi_{MS}] dk \quad (2.4)$$

where, $S(k)$ is the spectrum of the illumination source with respect to the wavenumber. In general, the integral (equation 2.4) is strictly true for low numerical apertures and has to be solved numerically. If $S(k)$ is assumed to be of Gaussian form (i.e. the illumination spectrum is Gaussian) then the second part of the integral will be a cosinusoidal variation multiplied by a Gaussian. This acts as an envelope of the fringe pattern and termed as the envelope function. It is maximum when the optical path difference is zero (i.e. $[h(x, y) - z] = 0$) and

decreases from both sides of the maximum. This is illustrated in Figure 2.5 for a simulated interferogram I_{out} with a white light source with Gaussian spectrum centred at 500 nm with bandwidth of 100 nm . The coherence length is of the order of $2.5\text{ }\mu\text{m}$. Considering Figure 2.5, if the total unwrapped phase difference is $\Delta\phi_u$ and the scan movement within fringe visibility is Δz then Sandoz *et al* suggested a measure of the effective wavenumber \bar{k} given by [16],

$$\bar{k} = \frac{1}{4\pi} \frac{\Delta\phi_u}{\Delta z} \quad (2.5)$$

From equation 2.5, considering the values of the above example, as expected an effective wavelength can be found out to be $\bar{\lambda} = \frac{1}{\bar{k}} = 500\text{ nm}$, which is approximately twice the length of the central fringe as shown in Figure 2.5.

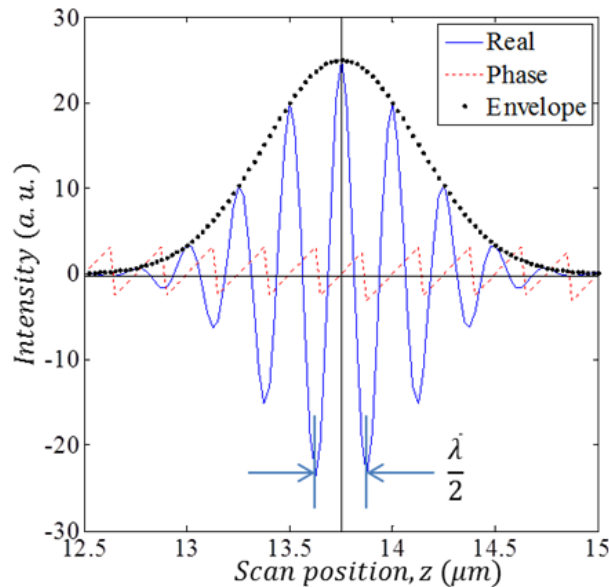


Figure 2.5 Simulated interferometric signal with Gaussian illumination spectrum centred at 500 nm and a bandwidth of 100 nm for a low-numerical-aperture objective

In the absence of dispersion the strongest interference is observed when the path length difference is zero and consequently, the modulation envelope provides an estimate of the position of the object surface. While the modulation envelope provides a broad estimate of the position of the object surface, the relatively high spatial frequencies within the fringe modulation provide a better measure. For this reason most CSI instrumentation uses the modulation envelope to estimate fringe order and subsequently, the object surface is deduced from the phase of the underlying fringe pattern. The different techniques are discussed in

Section 2.3. In these cases, the inherent assumption is that each pixel is independent of each other and data processing techniques are applied on interferometric signals along z-direction (Figure 2.5) separated out for each pixel. This is a simplification to the real situation and interference patterns, generally, have a coupling effect in adjacent pixels.

For more accurate modelling of fringe formation, dispersion of the system must be considered since it can change $\Delta\phi_{MS}(x, y, k)$ in equation 2.2. Even if the dispersion of the Mirau objective is compensated, a dispersive object can change $\Delta\phi_{MS}(x, y, k)$. This induces a shift to the coherence envelope and an additional phase shift of the position of the interference fringes within the coherence envelope [18-20].

2.3 FRINGE ANALYSIS

There are several ways to extract surface topography data from a CSI signal, but the most popular methods are detection of the modulation envelope, phase estimation or a combination of these. The fringe pattern intensity is given by equation 2.4. It is worth noting that real fringe data is likely to deviate from this ideal form for reasons including aberrations and dispersion introduced by the objective lens, surface tilt, roughness, multiple scattering effects and the noise introduced during the measurement process.

2.3.1 ENVELOPE DETECTION

Envelope detection is one of the most popular methods for the generation of surface topography and is deduced by calculating the modulation envelope in equation 2.4 [3, 7, 9]. The envelope term can be extracted in several ways that in essence demodulate the signal around the fringe frequency k . In general, envelope detection is made more robust (less noise prone) by fitting a curve to the envelope function or by calculating a centroid rather than to rely on its peak value [21]. Later, in Section 2.3.3, it will be discussed that centroid calculation is prone to noise, as well.

Caber has adapted digital filter concepts from communication theory to recover fringe contrast envelopes to produce fast and noncontact profiles of a wide range of surface roughness [3]. The modulation function is extracted from the fringe signal and its peak is detected. The relative surface height at that point can be measured by amplitude demodulation using high-speed digital hardware comprising a square law detector and filters.

Lee *et al* showed the coherence function is given by the envelope of the fringes. The fringes can be demodulated to find the peak amplitude of the envelope and the scan location z of the peak [9]. The method performed over all points provides a high lateral resolution image of the object. The increased lateral resolution results also from reduced crosstalk between laterally adjacent points due to the spatial incoherence of the illumination and the coherence detection scheme.

The method by Dresel *et al* is in a certain sense, a combination of time of flight and interferometry [7]. Instead of measuring the phase, they measured only the occurrence of interference. Because of the short coherence length, interference occurs only within those speckles that correspond to the surface elements close to the plane of the sample. These regions are detected and stored, while the object is moved slowly along the z axis.

2.3.2 PHASE ESTIMATION

The phase of the fringes depends on the path difference in two arms of the interferometer as well as the complex refractive index of the surface (equation 2.2). Generally, a phase estimation method is commonly used in the profilers who use spectrally resolved WLI methods, but there are other application areas [11, 22-28].

Since phase can only be determined unambiguously over the interval $0 - 2\pi$, the method can only be used in isolation, if the surface deviation is less than half the mean effective wavelength $\left(\frac{\bar{\lambda}}{2}\right)$. Phase unwrapping methods can be used for continuous surfaces for surface deviations more than $\frac{\bar{\lambda}}{2}$ (equivalently, phases more than 2π). The envelope detection is used to identify the zero order fringe and for the ideal case with no dispersion, the zero order fringe is the central bright fringe that corresponds to equal object and reference paths.

Bhushan *et al* have shown that phase measurement can be done by a method known as the integrating bucket method, where the relative phase between the test arm and the reference arm is varied at a constant rate rather than discrete steps resulting in less vibration related errors similar to PSI [22]. A similar system based on interference microscopy by Montgomery *et al* used phase stepping for automatic fringe analysis [27, 28]. The resolution obtained with this technique ($\sim 10 \text{ nm}$) was better than the predecessors of this working area.

A spectrally resolved white light interferometry (SRWLI) technique by Calatroni *et al* analyses the light spectrum of the recorded interference pattern from CSI and the surface profile along a line [23]. The set-up consists of a Mirau objective and a spectrometer before CCD, which separates out fringe patterns for different wavelengths from white light fringes. For this technique first the phase is estimated from the cosine (according to equation 2.4) and a linear fitting to the phase is done. In a second stage, the surface profile is computed since the phase is only $4\pi k$ times the profile and then the order of the fringes are matched with the profile to produce more accurate estimation ($\sim 1 \text{ nm}$) of surface profile. The paper reported by Schwider *et al* [24] introduces a similar method where interferometric profiler is based on a Fizeau interferometer. The method used here is termed as four step grating evaluation method where the phases of the fringe pattern (equation 2.2) are obtained by a Fast Fourier Transform (FFT) algorithm with appropriate filtering.

Hariharan *et al* proposed a method where a phase shifting technique is applied to overcome the error generated due to non-uniform contrast or modulation generated by moving the reference mirror for varying optical path [25]. Here, additional phase shifts are introduced in ϕ with the use of an arrangement of quarter-wave plates and half-wave plates, which works as an achromatic phase shifter to always maintain the central fringe as dark. They have also used this technique to overcome the problem of “batwings” or spurious diffraction errors [29].

Using a dispersive white-light interferometer, Schnell *et al* propose a similar phase estimation technique with linear fitting for measurement of absolute distance (essentially, the surface profile) together with the thicknesses of dielectric multilayer systems on the target [26]. Here, according to equation 2.2, they take into account that $\Delta\phi_{MS}$ is a nonlinear function of the surface profile, thicknesses of the layers and known refractive indices of the dielectric materials for the measurement of phase ϕ . The measurement with this technique is compared with “mechanically measured” distances and thicknesses for one and two layers of photoresist and SiO_2 upon silicon including the effects of thin films deposited upon the target and they conform within 10 nm accuracy.

2.3.3 ENVELOPE DETECTION WITH PHASE ESTIMATION

Most of the above techniques achieve a vertical resolution of the order of tens of nanometres but due to the phase ambiguities there is a need to combine phase estimation with

envelope detection. In all of the above techniques, the concern is to find the surface closest to the coherence peak from the discrete intensity data points so that the scanning-step distance ($\sim 0.1 \mu m$) does not limit the height resolution [3, 6, 30-32].

In 1995, further improvement of the height resolution ($3 nm$) was proposed by Hariharan *et al* with a technique that uses the PSI algorithms in white light interferometry, known as white light phase stepping interferometry (WLPSI) [33, 34]. The technique uses an achromatic phase shifter to shift (for four different phases) the white light fringe pattern or the correlogram at the best focus, the highest-contrast position during axial-scanning. Using a four point algorithm from the corresponding phases, known as the fractional phase, the overall phase information can be estimated. This technique significantly reduces computation need. The constraints on this technique are that the mechanical resolution of the steps needs to be better than the mean wavelength, $\bar{\lambda}$ and phase information computed is sensitive to the precision of the step rather than coherence-peak-sensing techniques. Secondly, the phase unwrapping procedure is required for the measured fractional phase from the best-focus to retrieve height information [30, 31, 33, 34].

Larkin in his seminal paper proposed a non-linear five-point algorithm, which is able to efficiently compute surface profile from the correlogram [30]. He introduced the idea of measuring coherence envelope peak together with computing the fractional phase to evaluate surface profile. Sandoz *et al* proposed an improvement in height-resolution ($\sim 1 nm$) by introducing a seven-point algorithm with identification of the fractional fringe order in WLPSI [16]. In this way, they were able to remove the 2π -ambiguities that showed well-separated values for different fringe orders in the case of low noise. The main assumption in this case is that the coherence envelope of the object is varying smoothly so that locally it can be considered as linear [31].

Instead of using WLPSI, the coherence-peak position between frames from the recorded discrete correlogram can be found by two methods. The first one is a least-squares fitting method for the coherence envelope from the source distribution [3, 31]. Kino *et al* proposed the other method of calculating the centroid from the correlogram for each pixel that yielded identical results for low noise [8, 35, 36]. However, Larkin and Harasaki argue that the centroid of the correlogram recorded for each pixel is not the best estimate of the focus due to noise. The centroid could deviate from the actual envelope peak at positions on or close to a discontinuity and then the fractional phase obtained from it would contain false

information. As a result, the phase measurement should be taken from the actual coherence-peak position rather than from the centroid position [30, 37, 38].

A less computationally intensive but powerful WLPSI technique by Harasaki *et al* is used for removal of ghost steps and fringe order identification errors [38]. In this paper an intuitive way to correct 2π ambiguities is proposed by finding the coherence-peak using linear fitting and then, evaluating the profile. A second profile is obtained by measuring the phase near zero phase condition using a five point algorithm. The ambiguity in the profile is removed by comparing the profiles obtained in these two cases assuring the differences between them is kept below $\lambda/4$.

The basic idea of all of these reports is that envelope detection can be combined with phase estimation using different computational techniques. The modulation envelope is used as the means to identify the fringe order with the phase analysis providing more accurate information of surface height. For mathematical formalism, let us suppose two sets of data, a) surface height estimate h_{xy} obtained from measuring the modulation envelope and b) θ_{xy} is the phase of the fringes at a height of h_{xy} . It is usual to define the phase gap, A_{xy} , as the differences,

$$A_{xy} = \theta_{xy} - 4\pi k h_{xy} \quad (2.6)$$

The two sets of data may be combined to produce a map of surface elevation h_{xy} given by,

$$h_{xy} = \frac{\theta_{xy}}{4\pi k} + \frac{1}{k} \text{round} \left(\frac{A_{xy} - \langle A \rangle}{4\pi} \right) \quad (2.7)$$

In this expression $\langle A \rangle$ is the field average of the phase gap A_{xy} , and the function $\text{round}()$ denotes the nearest integer value [13]. With the help of modern computers, this technique can provide nanometric resolution with less computational time.

2.3.4 FREQUENCY DOMAIN ANALYSIS (FDA)

Any source with a large, continuous range of frequencies can be loosely described as a white light source. Such a source is also said to have a *broadband spectrum*, composed of a continuous band of colours or wavelengths. In the case of white light interferograms, therefore, a whole range of sinusoidal patterns are superimposed on each other. It is still possible to extract phases for the individual frequencies contributing to the interference

effect. This is done by means of a Fourier Transform or more specifically, by the computationally efficient Fast Fourier Transform [39-41]. The phase can be described as a linear function of spatial frequency k and from the slope the surface height can be calculated as described later. A series of interference phase values for each of the spatial frequencies is needed to estimate the linear fit. Otherwise, there would be an ambiguity in uniquely defining the slope due to insufficiency of data [5, 6, 41, 42]. For a suitable dataset, there would be only one possible line in the frequency domain graph as shown in Figure 2.6.

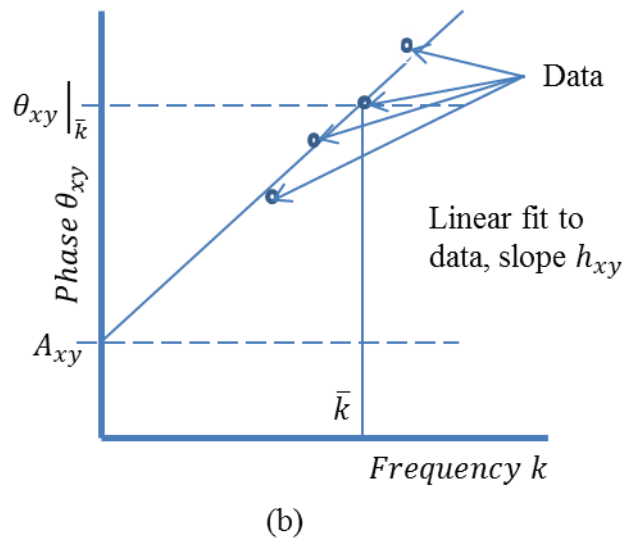


Figure 2.6 Linear fitting to phase in FDA analysis for unambiguous height detection [43]

Danielson *et al* have described a simple technique with a fibre Michelson low coherence interferometer and the ranging information is obtained by a Fourier transform method [4]. The authors suggest that if there is dispersion then the best possible way to analyse fringe data is by FDA. This information may be extracted from the intensity of a pixel $I_{xy}(z)$ through the normalized Fourier transform

$$P(k) = \int_{-\infty}^{\infty} I_{xy}(z) \exp(-j2\pi kz) dz \quad (2.8)$$

The desired phase evaluation is then given by,

$$\theta(k) = \tan \left[\frac{\text{Im}\{P(k)\}}{\text{Re}\{P(k)\}} \right] \quad (2.9)$$

Note that the phase gap A_{xy} , previously identified when calculating optical phase, is simply the axis intercept of the best fit line. Therefore, the optical phase is given by,

$$\theta_{xy} = A_{xy} + 2\pi k h_{xy} \quad (2.10)$$

where, h_{xy} is the gradient of the optical phase.

If this function is plotted against a range of white light frequencies k , then an estimate of the surface height at a pixel h_{xy} can be deduced from the gradient of the line best fit, as shown in Figure 2.6. From equation 2.10, for the effective wavenumber \bar{k} , this can be written as,

$$h_{xy} = \frac{\theta_{xy}|\bar{k} - A_{xy}}{2\pi\bar{k}} \quad (2.11)$$

The Fourier transform of each individual interference pattern results in a sequence of phase values that can be used to determine the local surface height. The high frequency content of the signal can be directly analysed using Fast Fourier transform (FFT) since an FFT of the intensity term $I_{xy}(z)$ generates the frequency spectrum $P(k)$. In principle, the measurement of surface topography without relying on fringe contrast is possible with FDA, because the analysis takes place entirely in the spatial frequency domain where the fringe contrast is never calculated [41-43]. The vertical resolution obtained is of the order of a nanometre [43].

CONCLUSION

In this chapter, the present state-of-the-art design and physical principles of CSI were discussed in detail. Interference fringes superimposed with image-stacks are recorded during vertical scan and computation techniques are applied for calculating surface topography. In all of the cases, it is assumed that the object is smoothly varying, therefore, higher slopes and sudden discontinuities are neglected. The second assumption is that the correlogram at each pixel does not perturb the correlogram at a neighbouring pixel. Depending upon the computation technique, the vertical resolution of the CSI is determined. On the other hand, the lateral resolution of the CSI is determined by the numerical aperture of the interferometric objective. In the next chapter, our analysis of CSI will be in terms 3D imaging theory.

REFERENCES

1. N. Balasubramanian, "Optical system for surface topography measurement", US Patent 4340306 (1982).
2. B. Bowe and V. Toal, "White light interferometric surface profiler", *Optical Engineering*, 37 (1998), 1796-1799.
3. P. J. Caber, "Interferometric profiler for rough surfaces", *Applied Optics*, 32 (1993), 3438-3441.
4. B. L. Danielson and C. Y. Boisrobert, "Absolute optical ranging using low coherence interferometry", *Applied Optics*, 30 (1991), 2975-2979.
5. P. de Groot and W. Kramer, J, "Height scanning interferometry method and apparatus including phase gas analysis", US Patent 6775006 (2004).
6. L. Deck and P. de Groot, "High-speed noncontact profiler based on scanning white-light interferometry", *Applied Optics*, 33, 31 (1994), 7334-7338.
7. T. Dresel, G. Häusler, and H. Venzke, "Three-dimensional sensing of rough surfaces by coherence radar", *Applied Optics*, 31, 7 (1992), 919-925.
8. G. S. Kino and S. S. Chim, "Mirau correlation microscope", *Applied Optics*, 29, 26 (1990), 3775-3783.
9. B.S. Lee and T.C. Strand, "Profilometry with a coherence scanning microscope", *Applied Optics*, 29, 26 (1990), 3784-3788.
10. A. Bosseboeuf and S. Petitgrand, "Characterization of the static and dynamic behaviour of M(O)EMS by optical techniques: status and trends", *Journal of Micromechanics and Microengineering*, 13 (2003), S23-S33.
11. J. Schwider, "White-light Fizeau interferometer", *Applied Optics*, 36, 7 (1997), 1433-1437.
12. M. R. Hart, R. A. Conant, K. Y. Lau and R. S. Muller, "Stroboscopic interferometer system for dynamic MEMS characterization", *Journal of microelectromechanical systems*, 9, 4 (2000), 409-418.
13. J. Petzing, J. M. Coupland and R. K. Leach, *Measurement good practice guide no. 116: The measurement of rough surface topography using coherence scanning interferometry* (National Physical Laboratory, 2010).
14. P. de Groot, "Coherence scanning interferometry", in *Optical characterisation of surface topography*, R. K. Leach ed. (Springer, 2011).
15. P. Hariharan, *Optical interferometry*, (Academic Press, 2003).
16. P. Sandoz, R. Devillers and A. Plata, "Unambiguous profilometry by fringe-order identification in white-light phase-shifting interferometry", *Journal of Modern Optics*, 44, 3 (1997), 519-534.
17. M. Born and E. Wolf, *Principles of Optics*, (Cambridge University Press, 1999).
18. A. Harasaki, J. Schmit and J. C. Wyant, "Offset of coherent envelope position due to phase change on reflection", *Applied Optics*, 40, 13 (2001), 2102-2106.
19. P. de Groot, X. C. de Lega, J. W. Kramer and M. Turzhitsky, "Determination of fringe order in white-light interference microscopy", *Applied Optics*, 41, 22 (2002), 4571-4578.
20. A. Pfortner and J. Schwider, "Dispersion error in white-light linnik interferometers and its implications for evaluation procedures", *Applied Optics*, 40, 34 (2001), 6223-6238.
21. R. Windecker, P. Haible and H. J. Tiziani, "Fast coherence scanning interferometry for measuring smooth, rough and spherical surfaces", *Journal of Modern Optics*, 42, 10 (1995), 2059-2069.

22. B. Bhushan, J. C. Wyant, and C. L. Koliopoulos, "Measurement of surface topography of magnetic tapes by Mirau interferometry", *Applied Optics*, 24, 10 (1985), 1489-1497.
23. J. Calatroni, A. L. Guerrero, C. Sainz, and R. Esacalona, "Spectrally-resolved white light interferometry as a profilometry tool", *Optics and Laser Technology*, 28, 7 (1996), 485-489.
24. J. Schwider and L. Zhou, "Dispersive interferometric profilometer", *Optics letters*, 19, 13 (1994), 995-997.
25. P. Hariharan, K. G. Larkin and M. Roy, "The geometric phase: interferometric observations with white light", *Journal of Modern Optics*, 41, 4 (1996), 663-637.
26. U. Schnell, R. Dändliker, and S. Gray, "Dispersive white-light interferometry for absolute distance measurement with dielectric multilayer systems on the target", *Optics letters*, 21, 7 (1996), 528-30.
27. P. C. Montgomery and J. Fillard, "Peak fringe scanning microscopy: submicron 3D measurement of semiconductor components", in *Interferometry: Techniques and Analysis*, G. M. Brown, O. Y. Kwon, M. Kujawinska, and G.T. Reid eds., San Diego, CA, USA: SPIE (1993), 12-23.
28. P. C. Montgomery, F. Anstotz, G. Johnson, and R. Kiefer, "Real time surface morphology analysis of semiconductor materials and devices using 4D interference microscopy", *Journal of Materials Science: Materials in Electronics*, 19 (2007), S194-S198.
29. M. Roy, J. Schmit and P. Hariharan, "White-light interference microscopy: minimization of spurious diffraction effects by geometric phase-shifting", *Optics Express*, 17, 6 (2009), 4495-4499.
30. K. G. Larkin, "Efficient nonlinear algorithm for envelope detection in white light interferometry", *Journal of Optical Society of America-A*, 13, 4 (1996), 832-843.
31. P. Sandoz, "Wavelet transform as a processing tool in white-light interferometry", *Optics letters*, 22, 14 (1997), 1065-1067.
32. R. Recknagel and G. Notni, "Analysis of white light interferograms using wavelet methods", *Optics Communications*, 148 (1998), 122-128.
33. P. Hariharan and M. Roy, "White-light phase-stepping interferometry: measurement of the fractional interference order", *Journal of Modern Optics*, 42, 11 (1995), 2357-2360.
34. P. Hariharan and M. Roy, "White-light phase-stepping interferometry for surface profiling" *Journal of Modern Optics*, 41, 11 (1994), 2197-2201.
35. S. S. C. Chim and G. S. Kino, "Correlation microscope", *Optics Letters*, 15, 10 (1990), 579-581.
36. S. S. C. Chim and G. S. Kino, "Three-dimensional image realization in interference microscopy", *Applied Optics*, 31, 14 (1992), 2550-2553.
37. A. Harasaki and J. C. Wyant, "Fringe modulation skewing effect in white-light vertical scanning interferometry", *Applied Optics*, 39, 13 (2000), 2101-2106.
38. A. Harasaki, J. Schmit and J. C. Wyant, "Improved vertical scanning interferometry" *Applied Optics*, 39, 13 (2000), 2107-2115.
39. J. D. Gaskill, *Linear systems, Fourier transforms and optics*, (John Wiley and Sons, Inc., 1978)..
40. J. W. Goodman, *An introduction to Fourier optics*, (The McGraw Hill Companies, Inc., 1996)
41. P. de Groot, "What is Frequency Domain Analysis", *Zygo Technical Bulletin*, (1993).
42. P. de Groot, "Method and apparatus for surface topography measurement by spatial frequency analysis of interferograms", *US Patent*, 5,398,118 (1995).

43. P. de Groot and X. C. de Lega, "Signal modelling for low-coherence height-scanning interference microscopy", *Applied Optics*, 43, 25 (2004), 4821-4830.

CHAPTER 3: THREE DIMENSIONAL LINEAR FILTERING THEORY OF CSI

INTRODUCTION

In the previous chapter the theory of CSI was based on a one dimensional (1D) treatment of optical imaging in the spatial domain. In this case the interference fringe pattern recorded was considered as the superposition of the scattered field from the object and a reference field at each vertical step as the object was scanned through the focus of the Mirau objective. This essentially constituted a stack of images which contained both amplitude and phase information about the scattered field. Different techniques to find the surface topography were also discussed. In all of these techniques, the combined effect of spectral variation of the source and illumination variation due to N_A over the envelope function are not taken into account. This can be viewed, however, as a three dimensional (3D) imaging problem to include all of the above effects. Essentially, in that case a coherent response is measured by the instrument once an optical radiation is incident on an object. The measured response for a point-like object would be the 3D point-spread-function (PSF) in the spatial domain, or equivalently, the transfer function (TF) in the spatial frequency domain. The response measured in spatial frequency domain can be obtained by a 3D Fourier transform technique.

In this chapter it will be shown that the 3D TF can be computed by a simple geometric construction related to the Ewald sphere in X-ray crystallography assuming electric fields to be scalar. The TF thus considered provides important parameters such as, the vertical and lateral resolutions and is a useful demonstration of the *illumination and observation* processes in CSI. This theoretical framework is also valid for other 3D imaging techniques such as, holography, confocal imaging and optical coherence tomography and CSI can be compared to these techniques in this way. [1-7].

3.1 THREE DIMENSIONAL LINEAR IMAGING

Here, starting from scalar diffraction theory CSI is described as a 3D linear imaging technique which is a simplification of the actual physical problem yet maintains the rigour and generality. Figure 3.1 shows a schematic diagram of the Mirau objective, which is at the heart of CSI. The light that illuminates the object forms the reference field ($E^r(\vec{r})$) (the field when object is absent) which is mixed with the scattered field ($E^s(\vec{r})$) coming from the object. The reference field ($E^r(\vec{r})$) is inverted to consider the reflection from the Mirau reflector ($-E^r(\vec{r})$). If the wavelength of the light is given by λ_0 then wavenumber is defined as $k_0 = \frac{1}{\lambda_0} = n \frac{\nu_0}{c}$ where, n is the refractive index of the medium, ν_0 is the frequency of the light and c is the speed of light in vacuum. The incident light rays on the object are from all possible angles within N_A of the Mirau objective and the scattered rays collected by the objective are restricted by N_A .

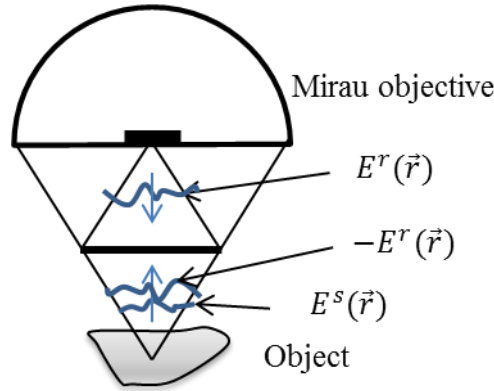


Figure 3.1 Schematic diagram of CSI

3.1.1 SCALAR DIFFRACTION THEORY

CSI provides a measure of the time-independent macroscopic properties of the object such as, dielectric constant or complex refractive index. Assuming scalar diffraction theory, the 3D point spread function (PSF) of CSI is calculated using of 3D linear filtering, here. At first a guide to the essential steps is provided with short descriptions of the tasks.

Assuming scalar diffraction theory, the 3D point spread function (PSF) of CSI is calculated using 3D linear filtering, here. At first a guide to the essential steps is provided with short descriptions of the tasks.

1. Assuming these macroscopic parameters (e.g. refractive index) vary slowly over a wavelength interval, one can arrive at the time-independent wave equation known as *Helmholtz equation* [8], which is central to the scalar diffraction theory. The *Helmholtz equation*, is solved in its integral form using the Green's function ($G(\vec{r})$).
2. From the Born approximation, the scattered field ($E^S(\vec{r})$) is expressed in terms of a convolution of Green's function with the field arising from the source.
3. The reconstructed field from the field measured at the boundary is then shown to be equivalent to a further linear filtering operation.
4. The restrictive nature of the aperture of Mirau objective is considered afterwards and from that the real measured field $E^m(\vec{r})$ is computed.
5. The 3D fringe pattern generated by CSI is the measured field superposed by all possible plane waves coming from different points on the aperture which is obtained by integrating (for all possible plane waves) the interference pattern due to one plane wave. Separating the term due to the object, namely, refractive index contrast Δ , a 3D PSF can be computed for monochromatic back-scattered case.
6. Further consideration of bandwidth of the illumination provides an expression for 3D PSF for CSI for the polychromatic case.

A monochromatic electric field with complex amplitude $E(\vec{r})$ propagating within a medium with complex refractive index $n(\vec{r})$ satisfies the *Helmholtz equation* given by,

$$\nabla^2 E(\vec{r}) + k_0^2 n^2(\vec{r}) E(\vec{r}) = 0 \quad (3.1)$$

The total field at any point $E(\vec{r})$ can be expressed as superposition of the reference field ($E^r(\vec{r})$), the illumination that would be present without the object and the scattered field ($E^S(\vec{r})$) due to the object such that,

$$E(\vec{r}) = E^r(\vec{r}) + E^S(\vec{r}) \quad (3.2)$$

The object, a region of inhomogeneity, encountered by $E^r(\vec{r})$ is defined by the *refractive index contrast* which is given by,

$$\Delta = \frac{(1 - n^2(\vec{r}))}{2} \quad (3.3)$$

An important point to be noted here that is assuming the light outside the region of inhomogeneity is travelling through vacuum, Δ would be zero outside. The reference field $E^r(\vec{r})$ must satisfy Helmholtz equation,

$$(\nabla^2 + k_0^2)E^r(\vec{r}) = 0 \quad (3.4)$$

Substituting equation 3.2 and equation 3.3 into equation 3.1 gives,

$$(\nabla^2 + k_0^2)E^s(\vec{r}) = 2k_0^2\Delta(\vec{r})(E^r(\vec{r}) + E^s(\vec{r})) = U(\vec{r}) \quad (3.5)$$

where, $U(\vec{r})$ defines the source that is non-zero in the region of inhomogeneity. The Green's function $G(\vec{r} - \vec{r}')$ for the *Helmholtz equation* is by definition the solution of the equation,

$$(\nabla^2 + k_0^2)G(\vec{r} - \vec{r}') = -\delta(\vec{r} - \vec{r}') \quad (3.6)$$

where, $\delta(\vec{r})$ is the 3D Dirac delta function and the negative sign in front is by convention. Using equation 3.6, $E^s(\vec{r})$ can be written in an integral form as [8],

$$E^s(\vec{r}) = \int_{-\infty}^{\infty} G(\vec{r} - \vec{r}')U(\vec{r}')d^3\vec{r}' = G(\vec{r}) \otimes U(\vec{r}) \quad (3.7)$$

where, \otimes denotes 3D convolution.

Until now the form of the Green's function was not specified. The Green's function in the spatial frequency domain (henceforth called as *k-space*) can be derived from equation 3.6 and be written as [9],

$$\tilde{G}(\vec{k}) = \frac{1}{|\vec{k}|^2 - k_0^2} \quad (3.8)$$

where, \vec{k} is the variable spatial frequency in k-space and $\tilde{}$ denotes Fourier transform. From equation 3.8 by Fourier transformation the Green's function in the spatial domain can be expressed as [9],

$$G(\vec{r}) = \frac{e^{j2\pi k_0|\vec{r}|}}{4\pi|\vec{r}|} \quad (3.9)$$

This is a well-known form that defines the *outgoing free-space* Green's function for a point-source as shown in Figure 3.2(a) calculated with $\bar{\lambda} = 635 \text{ nm}$ & $\bar{k} = 1/\bar{\lambda}$. $\tilde{G}(\vec{k})$ is shown in Figure 3.2(b) with the same wavelength. The Born approximation or more strictly the *first order Born approximation* neglects the effect of multiple scattering and assumes that

the scattered field due to the region of inhomogeneity modifies the reference field but only slightly so that it can be viewed as weakly scattering. This can simply be achieved if the scattered field $E^S(\vec{r})$ is removed from the right hand side in equation 3.5 such that,

$$U^B(\vec{r}) = 2k_0^2 \Delta(\vec{r}) E^r(\vec{r}) \quad (3.10)$$

$U^B(\vec{r})$ contains only reference field modified by source terms. Substituting equation 3.10 into equation 3.7 the scattered field is given by the convolution,

$$E^S(\vec{r}) = G(\vec{r}) \otimes U^B(\vec{r}) \quad (3.11)$$

This can be equivalently represented in k-space representation given by,

$$\tilde{E}^S(\vec{k}) = \tilde{G}(\vec{k}) \tilde{U}^B(\vec{k}) \quad (3.12)$$

where, $\tilde{U}^B(\vec{k})$ is the 3D spectral distribution of the source and $\tilde{G}(\vec{k})$ is simply a thin spherical shell of radius k_0 as shown in Figure 3.2(b). The corresponding free space Green's function in the spatial domain $G(\vec{r})$ is illustrated in Figure 3.2(a). Therefore, $E^S(\vec{r})$ is simply a *3D linear filtering operation applied to the source terms*.

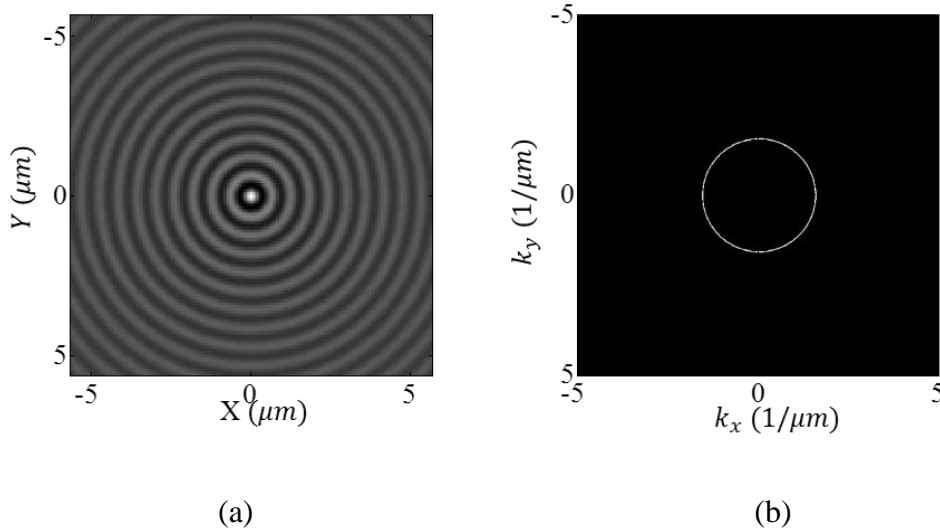


Figure 3.2 The Green's function in a) spatial domain (real) & b) k-space (absolute)

In practice the scattered field is only measured at a distant boundary. In the next section, a reconstruction of the scattered field from measurements at a distant spherical

boundary is computed. According to the Born Approximation, the field due to an arbitrary object can be considered as a linear supposition of fields due to suitably placed point sources. Therefore, a form of $\tilde{G}(\vec{k})$, termed as $\tilde{G}_{ideal}(\vec{k})$ will be derived at a point of measurement close to the source for the ideal case of a point source (the region of inhomogeneity). The reconstructed field due to an extended source can be computed from $\tilde{G}_{ideal}(\vec{k})$. From that the scattered field for an extended source, termed the *measured field*, can be expressed in terms of the reconstructed field and reference field from equation 3.12.

3.1.2 RECONSTRUCTION OF THE MEASURED FIELD DUE TO A POINT SOURCE

For computation of the reconstructed field from the field measured at the far-field in the ideal case of a point source the *integral theorem of Helmholtz and Kirchoff* is going to be used. In that case, an imaginary spherical boundary (S) with volume V in the far-field with radius \vec{r}_b ($|\vec{r}_b| = r_b$) around the point source is considered without the loss of generality, as shown in Figure 3.3. Therefore, from the measured field at a point P' on S (at far-field) due to the point-source, the field will be reconstructed at point P (close to the point-source) within V . The Cartesian co-ordinate system is suitably chosen so as to place P on the Z -axis. The distance of P from the origin is $r_z \cdot \vec{z}$ and $r_z \ll r_b$ and the angle of \vec{r}_b w.r.t. Z -axis is θ [9]. From the result of the *integral theorem of Helmholtz and Kirchoff* the reconstructed field $U^R(r_z \vec{z}, \vec{r}_b)$ at P can be calculated by,

$$U^R(r_z \vec{z}, \vec{r}_b) = \iint_S \left(G \frac{\partial E}{\partial n} - E \frac{\partial G}{\partial n} \right) dS \quad (3.13)$$

Let us consider a point source is placed at the origin. The field propagating from that source can be considered to be a spherical wave $E(\vec{r}_b)$ and can be written as,

$$E(\vec{r}_b) = \frac{e^{j2\pi k_0 r_b}}{4\pi r_b} \quad (3.14)$$

Differentiating equation 3.14,

$$\frac{\partial E(\vec{r}_b)}{\partial n} = (j2\pi k_0 - 1/r_b)E(\vec{r}_b)$$

For $r_b \gg 1$,

$$\frac{\partial E(\vec{r}_b)}{\partial n} = j2\pi k_0 E(\vec{r}_b) \quad (3.15)$$

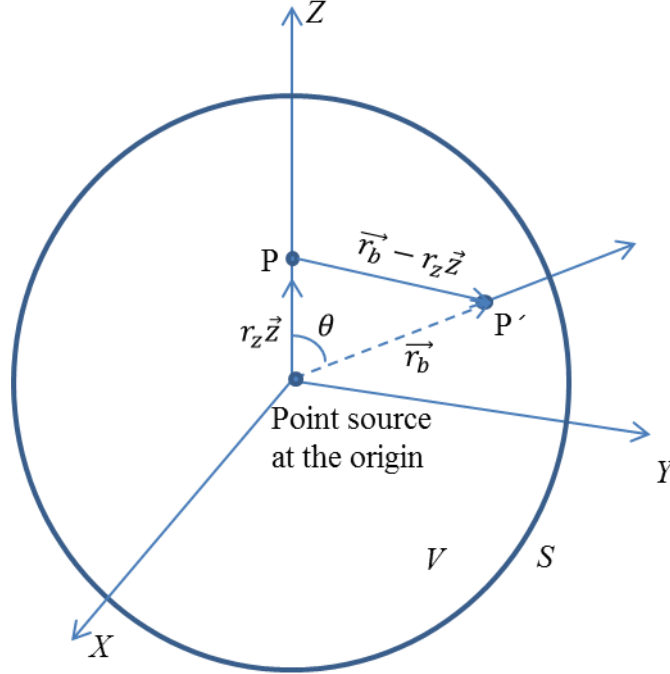


Figure 3.3 The reconstructed field due to a point source within a boundary at far-field

The Green's function that describes the propagation of the field from the boundary to P can be written as $G^*(\vec{r}_b - r_z \vec{z})$ and is given by,

$$G^*(\vec{r}_b - r_z \vec{z}) = \frac{e^{-j2\pi k_0 |\vec{r}_b - r_z \vec{z}|}}{4\pi |\vec{r}_b - r_z \vec{z}|} \quad (3.16)$$

If $r_z \ll r_b$, then $|\vec{r}_b - r_z \vec{z}| = r_b - \vec{r}_b \cdot r_z \vec{z} / r_b$, substituting into eqn. (3.16),

$$G^*(\vec{r}_b - r_z \vec{z}) = \frac{e^{-j2\pi k_0 r_b}}{4\pi r_b} \cdot e^{j2\pi k_0 \vec{r}_b \cdot r_z \vec{z} / r_b} \quad (3.17)$$

and the normal derivative is given by,

$$\frac{\partial G^*(\vec{r}_b - r_z \vec{z})}{\partial n} = -j2\pi k_0 G^*(\vec{r}_b - r_z \vec{z}) \quad (3.18)$$

Substituting equations 3.14 – 3.18 into equation 3.13

$$U^R(r_z \vec{z}, \vec{r}_b) = \iint_{S'} (2 \cdot j2\pi k_0 G^*(\vec{r}_b - r_z \vec{z}) \cdot E(\vec{r}_b)) dS$$

$$\begin{aligned}
&= j4\pi k_0 \iint_S \left(\frac{e^{j2\pi k_0 r_b}}{4\pi |\vec{r}_b|} \cdot \frac{e^{-j2\pi k_0 r_b}}{4\pi |\vec{r}_b|} \cdot e^{j2\pi k_0 \frac{\vec{r}_b}{r_b} \cdot r_z \vec{z}} \right) dS \\
\therefore U^R(r_z \vec{z}, \vec{r}_b) &= \frac{jk_0}{4\pi |\vec{r}_b|^2} \iint_S \left(e^{j2\pi k_0 \frac{\vec{r}_b}{r_b} \cdot r_z \vec{z}} \right) dS \tag{3.19}
\end{aligned}$$

Now to consider the field contribution only due to the boundary S , equation 3.19 the area element can be written as, $dS = \delta(r - r_b) dV$. Here, due to radial symmetry the coordinate system is converted from Cartesian to spherical polar to evaluate the integral in equation 3.19. Therefore, equation 3.19 can be rewritten as,

$$U^R(r_z \vec{z}, \vec{r}_b) = \frac{jk_0}{4\pi |\vec{r}_b|^2} \iiint_V \delta(r - r_b) \cdot \left(e^{j2\pi k_0 \frac{\vec{r}_b}{r_b} \cdot r_z \vec{z}} \right) \cdot r^2 \sin \theta \, d\theta d\varphi dr$$

and according to spherical polar co-ordinate from Figure 3.3, $\frac{\vec{r}_b}{r_b} \cdot r_z \vec{z} = r_z \cos \theta$, and it is found that,

$$U^R(r_z \vec{z}, \vec{r}_b) = \frac{jk_0}{4\pi |\vec{r}_b|^2} \int_{-\infty}^{\infty} \delta(r - r_b) \cdot r^2 \, dr \int_{-1}^1 e^{j2\pi k_0 r_z \cos \theta} d(\cos \theta) \int_0^{2\pi} d\varphi \tag{3.20}$$

Solving and putting all the limits the above integral can be written as,

$$U^R(r_z \vec{z}) = jk_0 \cdot \frac{\sin(2\pi k_0 r_z)}{(2\pi k_0 r_z)}$$

Therefore the above can be written as,

$$U^R(r_z) = jk_0 \operatorname{sinc}(2\pi k_0 r_z) \tag{3.21}$$

Since the system is spherically symmetric, r_z can be replaced with general notation of r and the reconstructed field in the spatial domain can be written as,

$$U^R(r) = jk_0 \operatorname{sinc}(2\pi k_0 r) \tag{3.22}$$

From equation 3.21, it can be clearly seen that even if the entire boundary values of the scattered field are measured at the far-field, the reconstruction of the field is a linear filtering process applied to the source distribution. In this case the PSF is a sinc function obtained from a delta function.

Note, here, Fourier transform (FT) is defined as, $\tilde{F}(\vec{k}) = \iiint_{\infty}^{\infty} f(\vec{r})e^{-j2\pi\vec{k}\cdot\vec{r}} d^3r$ and the inverse Fourier transform (IFT) as, $f(\vec{r}) = \iiint_{\infty}^{\infty} \tilde{F}(\vec{k})e^{j2\pi\vec{k}\cdot\vec{r}} d^3k$.

Taking FT of both sides of equation 3.22 and using the integral of δ -function from equation 3.20, FT of the reconstructed field can be written as,

$$\tilde{U}^R(\vec{k}) = \frac{j}{4\pi k_0} \delta(|\vec{k}| - k_0) \quad (3.23)$$

For the ideal case of a point source for which the whole of the scattered field components over the far-field boundary is measured, the transfer function $\tilde{G}_{ideal}(\vec{k})$ is given by,

$$\tilde{G}_{ideal}(\vec{k}) = \tilde{U}^R(\vec{k}) = \frac{j}{4\pi k_0} \delta(|\vec{k}| - k_0) \quad (3.24)$$

For the source distribution given by equation 3.10, the 3D source spectrum $\tilde{U}^B(\vec{k})$ can be written as,

$$\tilde{U}^B(\vec{k}) = \int_{\infty}^{-\infty} 2k_0^2 \Delta(\vec{r}) E^r(\vec{r}) e^{j.2\pi\vec{k}\cdot\vec{r}} d^3r \quad (3.25)$$

One can think of the source distribution as being comprised of an ensemble of point sources and therefore, from equation 3.12 the reconstructed field, which will henceforth be called as the ideal reconstructed field for ideal spherical boundary, $\tilde{E}_{ideal}(\vec{k})$ is given by,

$$\tilde{E}_{ideal}(\vec{k}) = \tilde{G}_{ideal}(\vec{k}) \tilde{U}^B(\vec{k}) \quad (3.26)$$

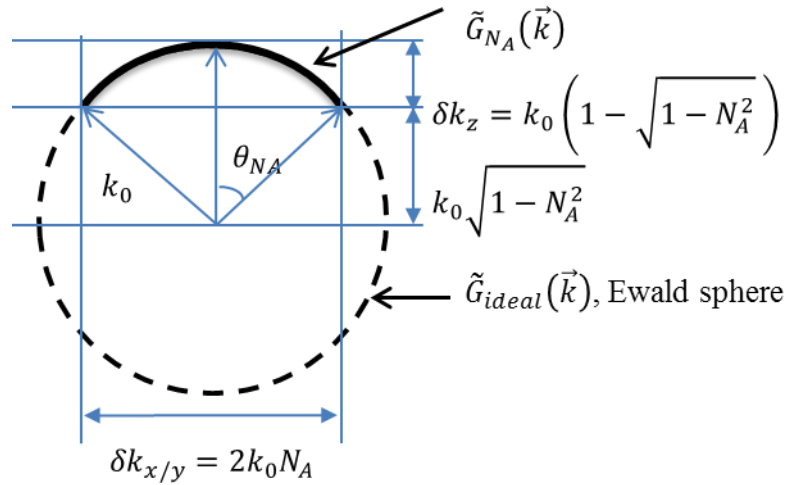


Figure 3.4 Ewald sphere and TF due to restricted N_A

From Figure 3.4, it can be seen that $\tilde{G}_{ideal}(\vec{k})$, the thin spherical shell covers all possible spatial frequencies with radius k_0 i.e. for a particular wavelength λ_0 . As in the case of holography, this thin spherical shell is termed the *Ewald sphere* in accordance to X-ray diffraction theory [7]. Optical instruments cannot measure field over the entire spatial frequency domain, however, due to the restriction of N_A . The TF due to this restricted N_A is termed as $\tilde{G}_{NA}(\vec{k})$ and it is only a part of the Ewald sphere as shown in Figure 3.4. A theoretical expression for $\tilde{G}_{NA}(\vec{k})$ can be written as [7],

$$\tilde{G}_{NA}(\vec{k}) = \frac{j}{4\pi k_0} \delta(|\vec{k}| - k_0) \cdot \text{step} \left(\frac{|\vec{k}|}{k_0} - k_0 \sqrt{1 - N_A^2} \right) \quad (3.27)$$

In the spatial domain, this can be expressed as,

$$G_{NA}(\vec{r}) = \frac{j}{4\pi k_0} \int_{-\infty}^{\infty} \delta(|\vec{k}| - k_0) \cdot \text{step} \left(\frac{|\vec{k}|}{k_0} - k_0 \sqrt{1 - N_A^2} \right) \cdot e^{-j2\pi\vec{k}\cdot\vec{r}} d^3 k \quad (3.28)$$

No closed form of solution of the above integral is available but some insight can be gained considering the direct representations of the axial and lateral resolutions of optical systems from the bandwidth of $\tilde{G}_{NA}(\vec{k})$ in the axial (δk_z) and lateral directions ($\delta k_{x/y}$), respectively. From Figure 3.4, the expressions for resolutions in different directions in terms of bandwidths in different directions can be expressed as,

$$\left. \begin{aligned} \delta x = \frac{1}{\delta k_x} &\Rightarrow \delta x = \frac{\lambda_0}{2N_A} \\ \delta y = \frac{1}{\delta k_y} &\Rightarrow \delta y = \frac{\lambda_0}{2N_A} \\ \delta z = \frac{1}{\delta k_z} &\Rightarrow \delta z = \frac{\lambda_0}{\left(1 - \sqrt{1 - N_A^2}\right)} \end{aligned} \right\} \quad (3.29)$$

Therefore, the maximum resolution in lateral directions would be half of the wavelength of the beam used for reconstruction considering $N_A^{max} = 1$, whereas, in axial direction it is λ_0 . The general measured field with a restricted aperture can be expressed as (from equation 3.26),

$$\tilde{E}^m(\vec{k}) = \tilde{G}_{NA}(\vec{k}) \tilde{U}^B(\vec{k}) \quad (3.30)$$

In the spatial domain equation 3.30 can be written as,

$$E^m(\vec{r}) = G_{NA}(\vec{r}) \otimes U^B(\vec{r}) \quad (3.31)$$

and the integral form of the measured field $E^m(\vec{r})$ from equation 3.27 and 3.30 can be expressed as,

$$E^m(\vec{r}) = \frac{j}{4\pi k_0} \int_{-\infty}^{\infty} \delta(|\vec{k}| - k_0) \cdot \text{step}\left(\frac{|\vec{k}|}{k_0} - k_0 \sqrt{1 - N_A^2}\right) \tilde{U}^B(\vec{k}) e^{-j2\pi\vec{k}\cdot\vec{r}} d^3 k \quad (3.32)$$

As before $E^m(\vec{r})$, the measured field due to the source spectrum distribution $\tilde{U}^B(\vec{k})$ for an optical system with restricted aperture can be expressed in terms of a 3D linear filtering process.

3.1.3 THREE DIMENSIONAL POINT SPREAD FUNCTION FOR CSI

For a monochromatic illumination equation 3.32 can be written in an integral form as,

$$E^m(\vec{r}) = 2k_0^2 \int_{-\infty}^{\infty} G_{NA}(\vec{r} - \vec{r}') \Delta(\vec{r}') E^r(\vec{r}') d^3 r' \quad (3.33)$$

In the case of CSI (from Figure 3.1) the recorded intensity (fringe pattern superposed with the object) at the CCD is due to the superposition of the reference field $-E^r(\vec{r})$ and the measured field $E^m(\vec{r})$. Since the measured field itself is a filtered version of the scattered field, CSI recordings are 3D linear filtering operations.

In 3D, the fringe pattern can be expressed as,

$$I(\vec{r}) = |E^m(\vec{r}) - E^r(\vec{r})|^2$$

For a monochromatic illumination with a particular plane wave (i^{th} wave) $E^r(\vec{r}) = e^{j2\pi\vec{k}_i\cdot\vec{r}}$, the above equation can be written as,

$$I_i(\vec{r}) = I(\vec{r}) = 1 + |E^m(\vec{r})|^2 - \underbrace{(E^m(\vec{r})^* e^{j2\pi\vec{k}_i\cdot\vec{r}} + E^m(\vec{r}) e^{-j2\pi\vec{k}_i\cdot\vec{r}})}_{\text{reconstruction term}} \quad (3.34)$$

In the case of CSI the intensity is comprised of these reconstruction terms for all possible plane waves with different spatial frequencies within the N_A of the Mirau objective. The overall intensity due to reconstruction for the i^{th} wave is given by substituting the expression of $E^m(\vec{r})$ from equation 3.33 into the reconstruction term in equation 3.34.

$$I_i^{\text{mono}}(\vec{r}) = 2k_0^2 \int_{-\infty}^{\infty} \underbrace{G_{NA}(\vec{r} - \vec{r}')}_{\text{CSI}} \underbrace{e^{j2\pi\vec{k}_i\cdot(\vec{r}-\vec{r}')} \Delta(\vec{r}')}_{\text{object}} d^3 r' \quad (3.35)$$

The term within the under-bracket as CSI is the convolution with refractive index contrast and this is similar to all optical instruments that follow back-scatter geometry. This is similar to the Green's function in case of the derivation of the scattered field as in equation 3.7.

For the i^{th} illumination wave, this can be expressed as,

$$H_i^{mono}(\vec{r}) = 2k_0^2 G_{NA}(\vec{r}) e^{j2\pi\vec{k}_i \cdot (\vec{r})} \quad (3.36)$$

In the frequency domain, equation 3.36 can be written as,

$$\tilde{H}_i^{mono}(\vec{k}) = 2k_0^2 \tilde{G}_{NA}(\vec{k} - \vec{k}_i) \quad (3.37)$$

In equation 3.36, the exponential term refers to different plane wave illuminations (i^{th} wave) with spatial frequency k_i . As with the observations, these plane waves are restricted within the aperture defined by the N_A and are given by $\tilde{G}_{NA}(\vec{k})$ as shown in Figure 3.4. Therefore, the exponential term (the plane waves) integrated over all possible spatial frequencies in backscatter is the same as $\tilde{G}_{NA}(\vec{k})$.

For all possible illumination spatial frequencies over an Ewald sphere with radius k_0 equation 3.37 can be written as [7],

$$\tilde{H}_{BS}^{mono}(\vec{k}) = \int_{-\infty}^{\infty} 2k_0^2 \tilde{G}_{NA}(\vec{k} - \vec{k}_i) \tilde{G}_{NA}(\vec{k}) d^3 k_i = 2k_0^2 \tilde{G}_{NA}(\vec{k}) \otimes \tilde{G}_{NA}(\vec{k}) \quad (3.38)$$

This is the transfer function (TF) of CSI if monochromatic illumination is used as shown in Figure 3.4. From equation 3.38 it can be seen that in the frequency domain $\tilde{G}_{NA}(\vec{k})$ is convolved with itself assuming there is no change in aperture in illumination side and recording side [7]. By writing this expression in the spatial domain one obtains an expression for the point spread function (PSF) which is the square of $G_{NA}(\vec{r})$ given by,

$$H_{BS}^{mono}(\vec{r}) = 2k_0^2 G_{NA}^2(\vec{r}) \quad (3.39)$$

In this case it can be seen that now the filtering is over the refractive index contrast rather than on the source terms and therefore, from equation 3.35 and 3.38, it can be written as,

$$I_m^{mono}(\vec{r}) = \int_{-\infty}^{\infty} \underbrace{H_{BS}^{mono}(\vec{r} - \vec{r}')}_{CSI} \underbrace{\Delta(\vec{r}')}_{object} d^3 r' \quad (3.40)$$

CSI uses polychromatic light by employing a broadband source and records fringe patterns simultaneously for all wavelengths with all possible spatial frequencies within N_A . Therefore, considering the spectral width of the source to be $S(k_0)$, the PSF can be expressed as,

$$H_{CSI}^{poly}(\vec{r}) = \int_{-\infty}^{\infty} S(k_0) 2k_0^2 G_{NA}^2(\vec{r} - \vec{r}') d^3 r' dk_0 \quad (3.41)$$

In the frequency domain the TF this can be expressed as,

$$\tilde{H}_{CSI}^{poly}(\vec{k}) = \int_{-\infty}^{\infty} S(k_0) 2k_0^2 [\tilde{G}_{NA}(\vec{k}) \otimes \tilde{G}_{NA}(\vec{k})] d^3 r' dk_0 \quad (3.42)$$

From Figure 3.5, the diagram of $\tilde{H}_{CSI}^{poly}(\vec{k})$ can be seen. Considering $k_{max/min} = \frac{1}{\lambda_{min/max}}$, the expressions for resolutions in different directions in terms of bandwidths in different directions is expressed in equation 3.43.

$$\left. \begin{aligned} \delta x = \frac{1}{\delta k_x} &\Rightarrow \delta x = \frac{\lambda_{min}}{4N_A} \\ \delta y = \frac{1}{\delta k_y} &\Rightarrow \delta y = \frac{\lambda_{min}}{4N_A} \\ \delta z = \frac{1}{\delta k_z + \delta k} &\Rightarrow \delta z = \frac{1}{\frac{N_A^2}{\lambda_{min}} + \frac{2\Delta\lambda}{\lambda_{min}\lambda_{max}}} \end{aligned} \right\} \quad (3.43)$$

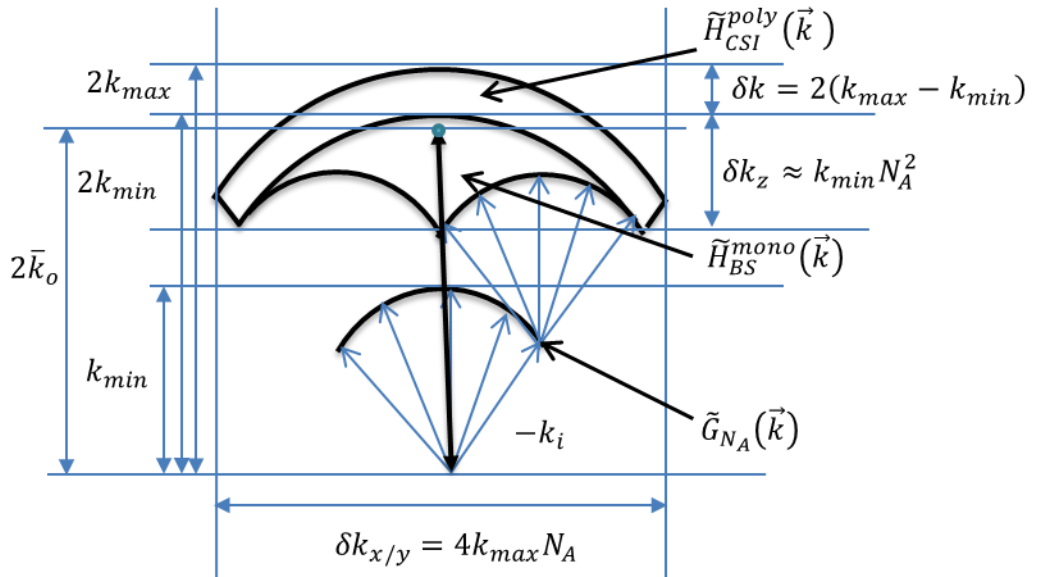


Figure 3.5 Transfer function of CSI

The spectrum $\Delta\lambda$ is small ($\sim 40\text{ nm}$) for LED illumination used for experiments performed later. Therefore, the vertical resolution δz for the set-up used is predominantly dependant on the N_A dependent term.

It is noted that the effective wavenumber \bar{k}_0 , defined in Section 2.2, is the z -component of the centroid of the TF given by,

$$\bar{k}_0 = \frac{1}{2} \cdot \frac{\int |\bar{k}| \tilde{H}_{CSI}^{poly}(\bar{k}) d^3 k}{\int \tilde{H}_{CSI}^{poly}(\bar{k}) d^3 k} \Bigg|_z \quad (3.44)$$

Finally, the fringe patterns or the intensity recorded for CSI with multiple wavelengths in terms of PSF can be written as,

$$I_{poly}^m(\vec{r}) = \int_{-\infty}^{\infty} H_{CSI}^{poly}(\vec{r} - \vec{r}') \Delta(\vec{r}') d^3 r' \quad (3.45)$$

Figure 3.6 presents a vertical cross-section through the PSF of an aberration free CSI instrument of $N_A = 0.55$ with a Gaussian spectral density with the central wavelength 600 nm and the bandwidth approximately 135 nm (at $1/e^2$).

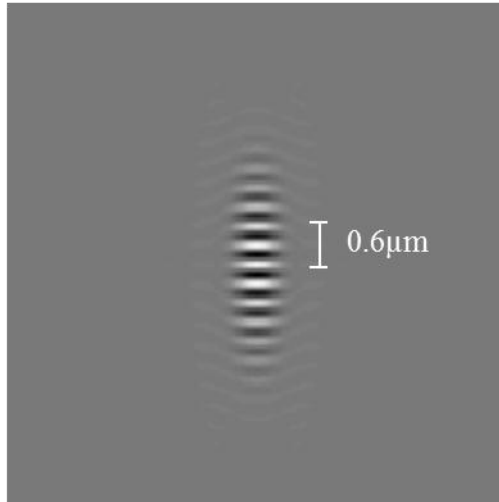


Figure 3.6 Real part of the point spread function

Until now the linear theory of CSI was described with the main focus on the instrument and its behaviour with a restricted aperture and a simplified model of weak scattering considering the Born approximation. The next section shows, however, that under certain conditions, a linear model of the object (refractive index contrast of the object) can be formulated without the Born approximation [11].

3.1.4 FOIL MODEL

For general inhomogeneous 3D objects, weak scattering can rarely be justified. This is because the wavelength of the field within an inhomogeneous bulk material generally varies significantly and after a propagation of just a few wavelengths the phase of the internal field will depart significantly from the illuminating field. In the case of CSI however, the situation is significantly different since the general concern is with the scattering from the surface of a homogeneous media. In this case, the assumption of weak scattering implies that the illuminating field at the surface is that which would be present in the absence of the object. In effect this means that the scattered field propagates from the surface via a single scattering event. Multiple scattering will occur predominantly when attempting to measure rough or high aspect ratio surfaces [10] but, it can often be neglected.

For surface scattering it is intuitive to consider only a thin “foil-like” layer on top of the object surface. Indeed, for the case of a metal object, the illuminating field is rapidly attenuated. The field is only of significance within the skin depth [8] and the remainder of the object has no measurable effect. If the metal is a perfect conductor then the skin depth is infinitesimally small while the complex refractive index contrast is infinitely large and the scattered field will be exactly that which would be scattered from a thin foil with the same profile.

In the following an *object function* defined by the convolution of the PSF and a refractive index contrast for this thin foil considering a near normal incident field for a smoothly varying object is presented. Consider a plane wave (as shown in Figure 3.7) to be an illumination field or reference field $E^r(\vec{r})$ from a distant source that is incident on a surface (S). The scattered field $E^s(\vec{r})$ reflects back towards the source, while the transmitted field $E^t(\vec{r})$ propagates into the bulk of the material of complex refractive index $n(\vec{r})$. The field at any point above S can be calculated by application of Kirchhoff’s theorem and proper selection of Green’s function. The outward normal direction is denoted by \hat{n} .

The boundary conditions in this case are,

$$\left. \begin{aligned} E^r + E^s &= E^t \\ \frac{\partial(E^r + E^s)}{\partial n} &= \frac{\partial E^t}{\partial n} \end{aligned} \right\} \quad (3.46)$$

From the Helmholtz equation it can be stated that,

$$\left. \begin{aligned} (\nabla^2 + n^2 k_0^2) E^t(\vec{r}) &= 0 \\ (\nabla^2 + k_0^2) G(\vec{r} - \vec{r}') &= 0 \end{aligned} \right\} \quad (3.47)$$

Multiplying first of equation 3.47 with $G(\vec{r} - \vec{r}')$ and second of equation 3.47 with $E^t(\vec{r})$ and simplifying,

$$G(\vec{r} - \vec{r}') E^t(\vec{r}) = \frac{1}{k_0^2(n^2 - 1)} (E^t(\vec{r}) \nabla^2 G(\vec{r} - \vec{r}') - G(\vec{r} - \vec{r}') \nabla^2 E^t(\vec{r})) \quad (3.48)$$

From equation 3.33 and the first boundary condition (equation 3.46) the scattered field in this case can be expressed as,

$$E^s(\vec{r}) = 2k_0^2 \int_{-\infty}^{\infty} G(\vec{r} - \vec{r}') \Delta(\vec{r}') E^t(\vec{r}') d^3 r' \quad (3.49)$$

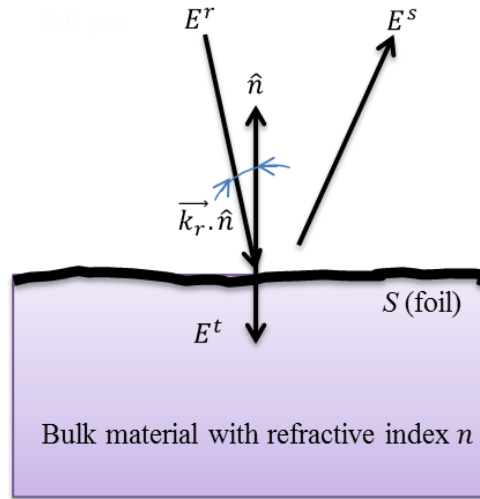


Figure 3.7 Foil surface with reference, scattered and transmitted field

Now, the contribution of the transmitted field is within the object volume. With the help of equation 3.48 and $\Delta(\vec{r}') = \frac{1-n^2(\vec{r}')}{2}$ this can be again written as,

$$E^s(\vec{r}) = - \int_V (E_t(\vec{r}') \nabla^2 G(\vec{r} - \vec{r}') - G(\vec{r} - \vec{r}') \nabla^2 E_t(\vec{r}')) d^3 r' \quad (3.50)$$

By applying Green's theorem to equation 3.50,

$$E^s(\vec{r}) = - \int_S \left(G \frac{\partial E^t}{\partial n} - E^t \frac{\partial G}{\partial n} \right) dS \quad (3.51)$$

This shows that the scattered field from a homogeneous medium can be written purely in terms of the field at the boundary. Since here the reference field is assumed to have near normal incidence ($\vec{k}_r \cdot \hat{n} \approx -k_r$), the variation with respect to the surface normal for the fields considered can then be simplified as,

$$\frac{\partial E^t}{\partial n} \sim -2\pi j n k_0 E^t \quad \& \quad \frac{\partial G}{\partial n} \sim -2\pi j k_0 G \quad (3.52)$$

The Fresnel amplitude transmission coefficient at normal incidence, considering the volume outside the object to be vacuum, is given by,

$$t = \frac{2}{1+n} \quad (3.53)$$

where n is refractive index of the transmitted medium.

The transmitted field can, therefore, be expressed as,

$$E_t = \frac{2E_r}{1+n} \quad (3.54)$$

Substituting equation 3.54 and 3.56 to equation 3.53

$$E^s(\vec{r}) = \int_S E^r(\vec{r}') \left\{ 4\pi j k_0 \left(\frac{n-1}{n+1} \right) \right\} G(\vec{r} - \vec{r}') dS \quad (3.55)$$

The main interest lies in finding the scattered field due to the uppermost layer of the material, the thin “foil”-like surface in the case of CSI. Therefore, the surface S in the Figure 3.7 can be thought of as an area under observation. At each point of observation on this area the foil is infinitesimally thin and the total area has a finite length in X and Y direction. This can be written as a window function $W(r_x, r_y)$ providing the finite width in lateral direction and with the delta function along Z direction for the infinitesimal thickness,

$$A(r) = W(r_x, r_y) \delta(r_z - f(r_x, r_y)) \quad (3.56)$$

where, $f(r_x, r_y)$ describes the surface profile.

From equation 3.56 the elemental surface area dS can be written as,

$$dS = \int_{-\infty}^{\infty} W(r_x, r_y) \delta(r_z - f(r_x, r_y)) dr_z \quad (3.57)$$

Finally, the scattered field due to the “foil” area is given by,

$$E_{foil}^S(\vec{r}) = \left\{ 4\pi j k_0 \left(\frac{n-1}{n+1} \right) \right\} \int_S E^r(\vec{r}') G(\vec{r} - \vec{r}') \left\{ \int_{-\infty}^{\infty} W(r_x, r_y) \delta(r_z - f(r_x, r_y)) dr_z \right\} \quad (3.58)$$

The field contribution due to the entire bulk of the material is due to the top-layer of the surface, in this case the foil area. The refractive index contrast is zero outside this region of interest and therefore, no contribution to the scattered field would come from outside. The limits of integration can, therefore, be extended to infinity in each lateral direction. From equation 3.58, in analogy with the measured field from equation 3.33, for the scattered field due to the foil can be expressed as,

$$E_{foil}^m(\vec{r}, k_0) = k_0 \int_{-\infty}^{+\infty} G_{NA}(\vec{r} - \vec{r}') \Delta_{foil}(r') E(\vec{r}') d^3 r' \quad (3.59)$$

where $\Delta_{foil}(r)$ is the computed surface or the ‘foil’ model of the surface and it is defined as,

$$\Delta_{foil}(r) = 4\pi j \underbrace{\left(\frac{n-1}{n+1} \right)}_{\substack{\text{Fresnel} \\ \text{reflection} \\ \text{coefficient}}} W(r_x, r_y) \delta(r_z - f(r_x, r_y)) \quad (3.60)$$

The computed surface clearly shows terms containing Fresnel reflection coefficient for normal incidence, which would in turn modify the measured field.

For the foil model therefore, the PSF can be expressed from equation 3.59 in analogy to equation 3.41 as,

$$H_{foil}(\vec{r}) = \int_{-\infty}^{+\infty} k_0 S(k_0) G_{NA}^2(\vec{r}) d^3 r dk_0 \quad (3.61)$$

In the case of CSI, therefore, the PSF from equation 3.61 together with the foil surface defined from equation 3.60 generates fringe formation for different profiles (equation 3.45) given by,

$$O(\vec{r}) = \int_{-\infty}^{\infty} H_{foil}(\vec{r} - \vec{r}') \Delta_{foil}(r') d^3 r' \quad (3.62)$$

This is the expression for the simulated fringe pattern (interferograms) for CSI or in other words, the output of CSI.

In the case of a perfect conductor the reflection coefficient is unity and does not change with angle. In the case of a real metal, however, the inhomogeneous field within the skin depth affects the phase and amplitude of the scattered field. This results in a variation of

the reflection coefficient with the angle of incidence making it polarization dependent [8]. For the case of CSI, however, the variation is small for the range of angles accepted by the numerical aperture of a typical instrument and the phase change results in an apparent movement of the object surface in an axial direction. For the case of a dielectric surface, the situation is similar however, there is no phase change and although the magnitude of reflection coefficient is quite small it is reasonably constant over the range of angles accepted by the N_A of the instrument. Consequently, providing that there is no multiple scattering from internal surfaces (such as thick films), scattering from dielectric and metal surfaces will closely resemble that from a perfect conductor and the foil model will remain valid.

3.1.4.1 APPLICATION OF THE FOIL MODEL WITH SINUSOIDAL PROFILE

For comparison with real-life measurement applications, the foil model is considered for a sinusoidal surface. In Figure 3.8 an experimental measurement with CSI of a metallic sinusoidal grating with $8 \mu m$ pitch, $466 nm$ amplitude (pk-pk) is presented. The ideal form is shown by the dashed line and measurement profile with shown with continuous line. It clearly shows a fringe order errors of $300 nm$ whenever higher gradient is encountered.

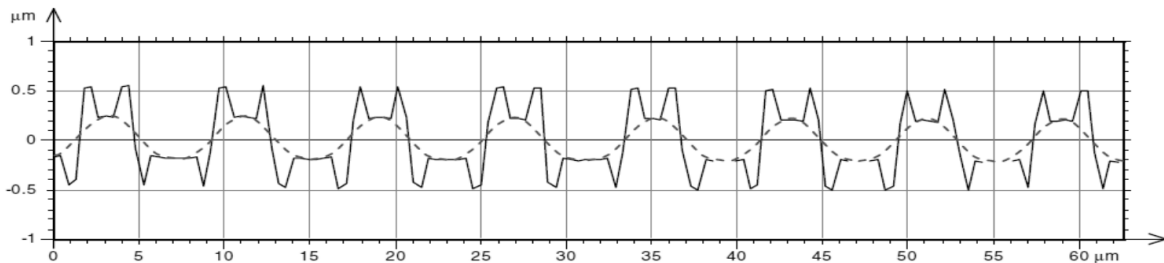


Figure 3.8 A CSI measurement of sinusoidal grating $8 \mu m$ pitch and $466 nm$ amplitude (pk-pk)

A sinusoidal surface is considered to illustrate the fringe generation process and the effect of the PSF when it is investigated using an ideal CSI instrument that is free from aberration. The sinusoidal profile is modelled as the foil defined by the profile,

$$f(r_x, r_y) = a_0 \sin\left(\frac{2\pi r_x}{\lambda_g}\right) \quad (3.63)$$

where, a_0 and λ_g are the amplitude and wavelength of the grating respectively. In this work the 3D convolution of equation 3.62 was evaluated numerically using an FFT algorithm implemented in MATLAB software.

Figure 3.9 shows the interferogram generated by the foil model of CSI for the case of an ideal system mentioned in Section 3.1.3 (Figure 3.6) when the instrument is used to measure a grating with the same pitch and amplitude as that illustrated in Figure 3.8. The white dotted line, shown in Figure 3.9 shows the surface profile that is obtained by finding the peak in the fringe envelope. It can be seen that ideal optics should be capable of identifying the correct fringe and consequently, should provide a good measurement of the surface profile as shown in Figure 3.9. It can be seen that near the higher gradient areas it tends to be less accurate [11].

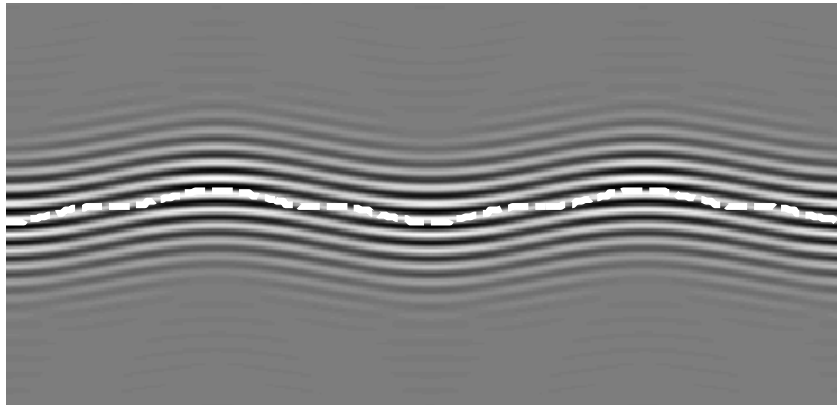


Figure 3.9 Interferogram generated by the foil model for sinusoidal grating 8 μm pitch, 466 nm amplitude (pk-pk)

The effect of the PSF becomes more noticeable as the surface gradient increases. For example if the pitch of the sinusoidal profile is decreased to 3.3 μm the foil model with ideal PSF generates the fringe pattern shown in Figure 3.10. Fringe order errors similar to that shown in Figure 3.8 are now apparent at points where the gradient is steep.

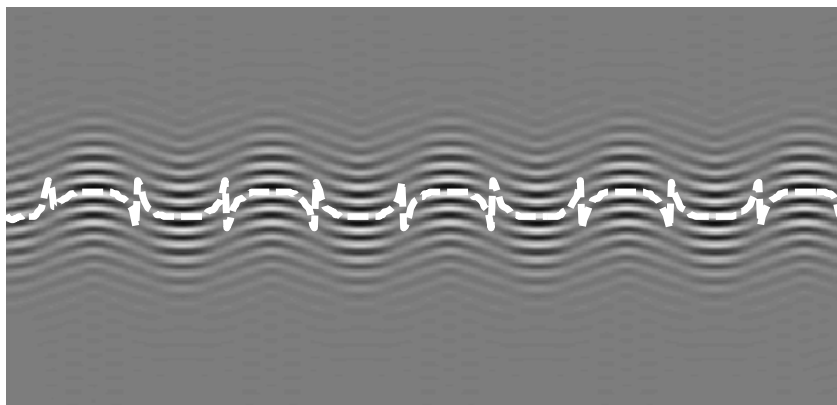


Figure 3.10 Interferogram generated by the foil model for sinusoidal grating 3.3 μm pitch, 466 nm amplitude (pk-pk)

The pitch of the grating in Figure 3.8 and Figure 3.10 are not the same, therefore, it was just used to illustrate the match between a real-life measurement and a simulation. It seems that the jumps are opposite in polarity which was not recognised before. At this moment, this cannot be explained and further work is required to understand this.

CONCLUSION

In this chapter a linear theory of CSI instrumentation, in which the system response can be characterised by its 3D point spread function (PSF), was considered. This is appropriate to surface profilometry providing that multiple scattering effects are negligible. In this case the scattering from the object surface is equivalent to that from a foil-like object with the same surface profile. The application of the linear theory to an analogous foil-like surface is termed as “the foil model of CSI”. From the 3D linear imaging technique different parameters of CSI can be easily obtained. Fringe patterns due to different object geometries can also be generated and examined. Another important aspect is that the refractive index contrast of the foil surface is dependent on the complex Fresnel reflection coefficient of the object material (especially, metal). In the case of metals, the reflection coefficient will introduce additional phase to the interference pattern which will shift the fringes. These effects will be discussed in detail for the next two chapters.

REFERENCES

1. C. W. McCutchen, "Generalized aperture and the three-dimensional diffraction image", *Journal of Optical Society of America*, 54 (1964), 240-244.
2. E. Wolf, "Three-dimensional structure determination of semi-transparent objects from holographic data", *Optics Communication*, 1 (1969), 153-156.
3. R. Dändliker and K. Weiss, "Reconstruction of the three-dimensional refractive index from scattered waves", *Optics Communication*, 1 (1970), 323-328.
4. B. R. Frieden, "Optical transfer of the three-dimensional object", *Journal of Optical Society of America – A*, 57(1967), 56-66.
5. C. J. R. Sheppard, "General considerations of diffraction theory of 3-D imaging", *European Journal of Cell Biology Supplement*, 25 (1989), 29-32.
6. C. J. R. Sheppard and C. J. Cogswell, "Three-dimensional image formation in confocal microscopy", *Journal of Microscopy*, 159 (1990), 179-194.
7. J. M. Coupland and J. Lobera, "Holography, tomography and 3D microscopy as linear filtering operations," *Measurement Science and Technology*, 19 (2008), 1-12.
8. M. Born & E. Wolf, *Principles of Optics*, (Cambridge University Press, 2005)
9. J. W. Goodman, *Introduction to Fourier Optics*, (Roberts and Company, 2005)
10. J. M. Coupland and J. Lobera, "Measurement of Steep Surfaces Using White Light Interferometry," *Strain*, 46 (2010), 69-78.
11. K. Palodhi, J. M. Coupland, R. K. Leach, "A linear model of fringe generation and analysis in coherence scanning interferometry," *ASPE Summer Topical Meeting*, (2010).

CHAPTER 4: MEASUREMENT OF SURFACE HEIGHT OFFSET FOR AN OBJECT WITH MULTIPLE MATERIALS

INTRODUCTION

In the previous chapter CSI was described as a 3D linear imaging method with the object defined as a foil-like surface and the fringe pattern produced as the convolution of this foil with a 3D PSF. In the foil-model, it was mentioned that the fringe pattern changes for metallic objects when measured under CSI due to the complex refractive indices. This results in a surface height offset and there is an apparent shift of surface topography in the axial direction. For a homogeneous object, i.e., an object made of a single material, the entire profile is shifted axially with no change in the profile whereas for an inhomogeneous object made of a number of materials, each material introduces different height offset and therefore, an inaccurate surface profile will be measured. The measurement of this phase offset by different materials with a CSI using modified optical configuration will be explored in this and the subsequent chapters.

First, ellipsometry which is widely used for the measurement of complex refractive index will be discussed [1, 2]. The same information, however, can be obtained in the back-focal-plane of an objective by the method known as microellipsometry (ME) described by See *et al* [3] and there are other variant techniques reported based on similar concepts [4-6]. In this chapter, a microellipsometry set-up will be described for a *single-point* measurement of the phase offset from which complex refractive index of the material can be calculated. Ellipsometry and ME already exist in literature and were done to prepare the basis for whole-field polarisation sensitive CSI. Later, a new polarisation-sensitive CSI configuration enabling *whole-field* measurement of phase offset and surface topography will be discussed.

4.1 ELLIPSOMETRY

Ellipsometry, invented by Drude in 1887, is one of the most popular and high-precision techniques for measurement of a variety of optical parameters and material

properties such as, complex refractive index \mathbf{n} , dielectric constant $\boldsymbol{\epsilon}$, etc. In ellipsometry, a surface is illuminated with polarised light and from the change of polarisation in the reflected light the properties mentioned above are computed. There are variants of ellipsometric techniques, such as the spectroscopic ellipsometer, the real-time spectroscopic ellipsometer and the real-time spectroscopic ellipsometer with photodetector array [7-11]. The following section introduces the fundamental physics that governs reflection from a planar surface and the ellipsometric technique.

4.1.1 FRESNEL EQUATIONS

When a light beam (plane wave) is incident on the interface of two isotropic media, part of the beam reflects back to the medium of refractive index \mathbf{n}_1 from which the light is coming and the other part will be transmitted into the second medium of refractive index \mathbf{n}_2 as shown in Figure 4.1 [12].

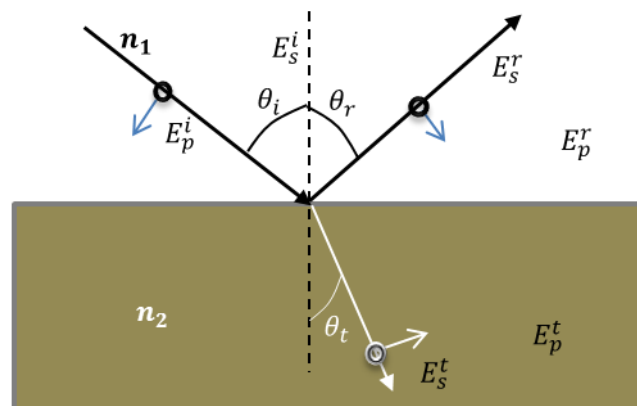


Figure 4.1 Light beam incident on the interface of two isotropic media

The light beams can be represented with a combination of orthogonal components. As shown in Figure 4.1, the component with its electric vector contained within the plane of incidence is known the p – polarised component (shown with an arrow) and the other with its electric vector perpendicular to the plane of incidence (shown with an annular circle) is known as the s – polarised component [13]. The superscripts “i”, “r” and “t” in Figure 4.1 denote the incident, reflected and transmitted field, respectively. The fractions of light amplitude reflected or transmitted for these two components are determined by the well-known Fresnel equations and the amplitude reflection coefficients and the amplitude transmission coefficients are given by,

$$\mathbf{r}_p = \frac{E_p^r}{E_p^i} = \frac{\tan(\theta_i - \theta_r)}{\tan(\theta_i + \theta_r)} \quad (4.1)$$

$$\mathbf{t}_p = \frac{E_p^t}{E_p^i} = \frac{2 \sin \theta_r \cos \theta_i}{\sin(\theta_i + \theta_r) \cos(\theta_i - \theta_r)} \quad (4.2)$$

$$\mathbf{r}_s = \frac{E_s^r}{E_s^i} = -\frac{\sin(\theta_i - \theta_r)}{\sin(\theta_i + \theta_r)} \quad (4.3)$$

$$\mathbf{t}_s = \frac{E_s^t}{E_s^i} = \frac{2 \sin \theta_r \cos \theta_i}{\sin(\theta_i + \theta_r)} \quad (4.4)$$

where, θ_i is incidence angle, θ_r is the transmission angle given by, $\theta_r = \sin^{-1} \left(\frac{n_1 \sin \theta_i}{n_2} \right)$ and \mathbf{r}_p & \mathbf{t}_p and \mathbf{r}_s & \mathbf{t}_s are the reflection and transmission coefficients for p – and s – polarised light, respectively. The refractive indices of the two media are, in general, complex quantities and can be written as \mathbf{n}_1 & \mathbf{n}_2 , where, the refractive index is denoted as $\mathbf{n} = n + j\kappa$. The complex part is known as extinction coefficient which measures the amount of absorption by the material. For dielectrics, the reflection and transmission coefficients are real-valued but, in general, they are complex.

4.1.2 NULL ELLIPSOMETRY

In general, when a linearly polarised light beam reflects from a metal surface, it produces an elliptically polarised reflected beam. In ellipsometry this change of the polarisation is measured in terms of the relative amplitude change ψ , and the relative phase change Δ , which are known as the ellipsometric parameters. The ratio of the Fresnel reflection coefficients can be written directly in terms of ellipsometric parameters [1, 2, 13] such that,

$$\boldsymbol{\rho} = \frac{r_p}{r_s} = \tan \psi \exp(j\Delta) \quad (4.5)$$

where, ρ the ratio of the reflection coefficients, a complex constant that depends on the incidence angle. For ellipsometric consideration the relative phase is conventionally written as $\Delta = 180^\circ + \arg \left(\frac{r_p}{r_s} \right)$ where $\arg(\mathbf{z})$ means argument of a complex number \mathbf{z} [13].

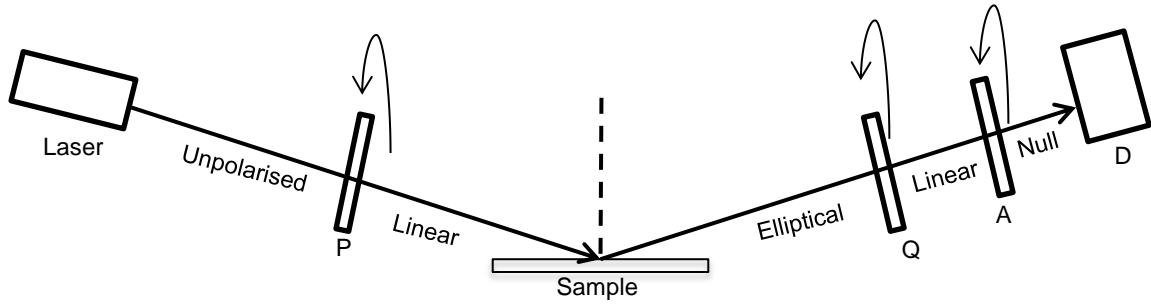


Figure 4.2 Null ellipsometry with single wavelength

In null ellipsometry, as shown in Figure 4.2, a laser source illuminates a sample with plane polarised light after it passes through the polariser (P). In general, a reflected beam would be elliptically polarised and the quarter wave plate Q is rotated so that this elliptically polarised beam becomes plane-polarised. Finally, the beam passes through a linear polariser called an analyser (A), which is rotated to register a null intensity at the photodetector D.

From the rotation angles of P, Q and A, ψ and Δ can be computed to produce ρ . The refractive index of the sample surface can then be calculated by the expression [13],

$$n_2 = \left(n_1^2 \sin^2 \theta_i \left[1 + \left(\frac{1-\rho}{1+\rho} \right)^2 \tan^2 \theta_i \right] \right)^{1/2} \quad (4.6)$$

In ellipsometry, the incident beam illuminates an area of the sample depending on the laser beam diameter and therefore, the results obtained are averaged over this illumination area with low spatial resolution of the order of 10 mm. The same information, however, can be retrieved from the back-focal-plane of a microscope objective used to focus and acquire reflected light from the object. This technique, known as microellipsometry, has a much higher spatial resolution compared to the ellipsometer of the order of 10 μm .

4.2 MICROELLIPSOMETRY

Single point measurement of ellipsometric parameters using microellipsometry was first proposed by See *et al* and later a modified version of that was reported by Feke *et al* [3, 4]. A generic configuration capable of microellipsometry is shown in Figure 4.3. In this set-up a plane polarised beam is brought to focus by a microscope objective on the surface of an object.

In this way the object is simultaneously illuminated by a field containing all plane wave components that propagate through the numerical aperture of the objective as shown in Figure 4.3. If it is assumed that the surface normal is parallel to the optical axis, the angle of incidence (and also reflection) of each plane wave component is uniquely defined by position in the back focal plane of the objective. By measuring the phase and amplitude changes between the field at one or more points in the back focal plane, when the source polarisation is rotated by 90° , the ellipsometric parameters can be deduced. More generally, if the local surface gradient is known, the incidence angle can be deduced and a similar analysis provides the ellipsometric parameters.

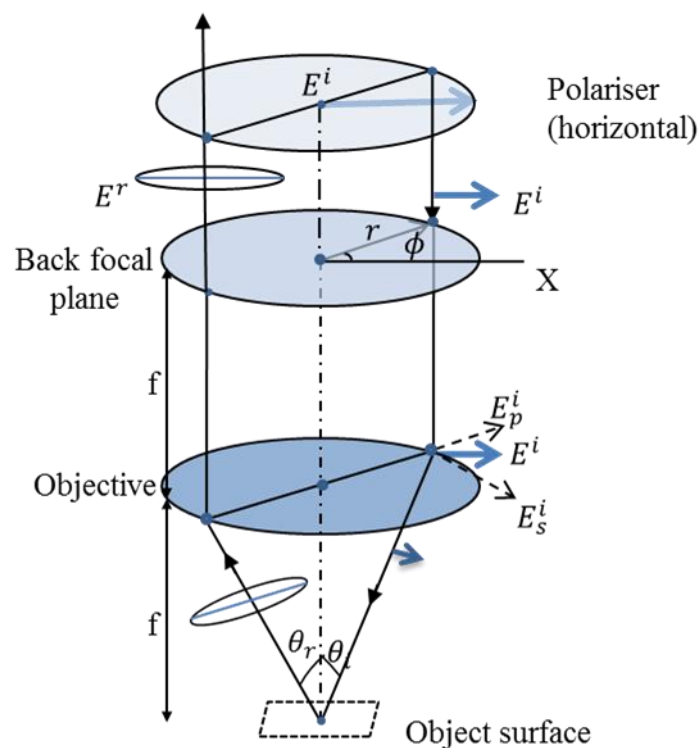


Figure 4.3 Geometry of the p – and s – component [15]

With reference to Figure 4.3 an expression for the phase and amplitude of the component of the reflected field in the back focal plane can be derived as follows. Consider a laser source that provides plane polarised, plane wave illumination in the back focal plane of the objective through the polariser, such that it is focused to a point on the flat metal coated sample as shown in Figure 4.3. It is noted that the p – and s – components are aligned in the radial and transverse directions in the back-focal-plane. Here, r is the radial distance and the angle measured from X-axis in the back-focal-plane is given by azimuth ϕ . A particular ray

passing through the edge of the aperture of the objective reflects from the sample and upon reflection a phase change between the p – and s – components causes the polarisation state to become elliptical, as shown in Figure 4.3. In this way each point in the back focal plane corresponds to a plane wave component in the sample illumination.

The horizontal and vertical polarisation can be described as polarisations in azimuth $\phi = 0^\circ$ and $\phi = 90^\circ$ direction, respectively. The phase change upon reflection due to the orthogonal polarisations mentioned above is measured at a point at the edge of the aperture on X-axis i.e. at $\phi = 0^\circ$. The phase offset is calculated from the difference in phase for each orthogonal polarisation and the expressions of these phase changes will be derived in the following.

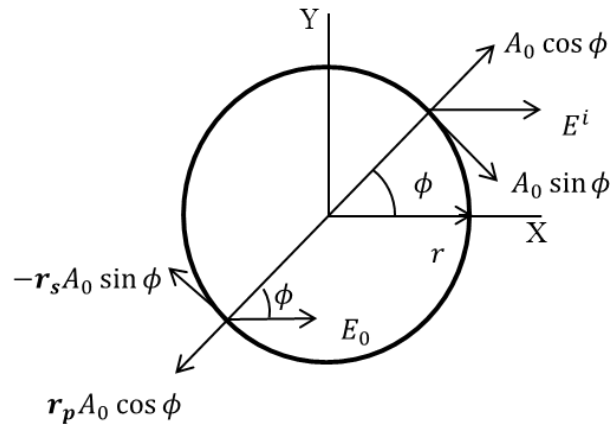


Figure 4.4 The p – and s – components of the reflected beam

Consider first the case of illumination with amplitude $E^i = A_0 e^{j\Phi(r,\phi)}$, in the back-focal-plane with the plane of polarisation in $\phi = 0^\circ$ direction as shown in Figure 4.4 where the phase term $\Phi(r, \phi)$ is introduced due to all aberrations in the optical system. The p – and s – components of the incident field in the back-focal-plane are $E_p^i(r, \phi)$ and $E_s^i(r, \phi)$, respectively, and they are given by,

$$\left. \begin{aligned} E_p^i(r, \phi) &= A_0 e^{j\Phi} \cos \phi \\ E_s^i(r, \phi) &= A_0 e^{j\Phi} \sin \phi \end{aligned} \right\} \quad (4.7)$$

The angle of incidence in this case is $\theta_i = \tan^{-1} \left(\frac{r}{f} \right)$ where, f is the focal length of the objective (Figure 4.3). The p – and s – components of the reflected fields $E_p(r, \phi)$ and $E_s(r, \phi)$, respectively, in the back focal plane can be written as,

$$\left. \begin{aligned} E_p^r(r, \phi) &= \mathbf{r}_p A_0 e^{j\Phi} \cos \phi \\ E_s^r(r, \phi) &= -\mathbf{r}_s A_0 e^{j\Phi} \sin \phi \end{aligned} \right\} \quad (4.8)$$

where, $\mathbf{r}_p, \mathbf{r}_s$ are the amplitude reflection coefficients.

From Figure 4.4 the component of the reflected field $E_0(r, \phi)$ that is parallel to the incident field is expressed as,

$$E_0(r, \phi) = -A_0 e^{j\Phi} (\mathbf{r}_p \cos^2 \phi - \mathbf{r}_s \sin^2 \phi) \quad (4.9)$$

Similarly, the reflected field $E_{90}(r, \phi)$, for the case of field normal to the incident field, can be written as,

$$E_{90}(r, \phi) = -A_{90} e^{j\Phi} (\mathbf{r}_p \sin^2 \phi - \mathbf{r}_s \cos^2 \phi) \quad (4.10)$$

where, the incident field is $E^i = A_{90} e^{j\Phi}$.

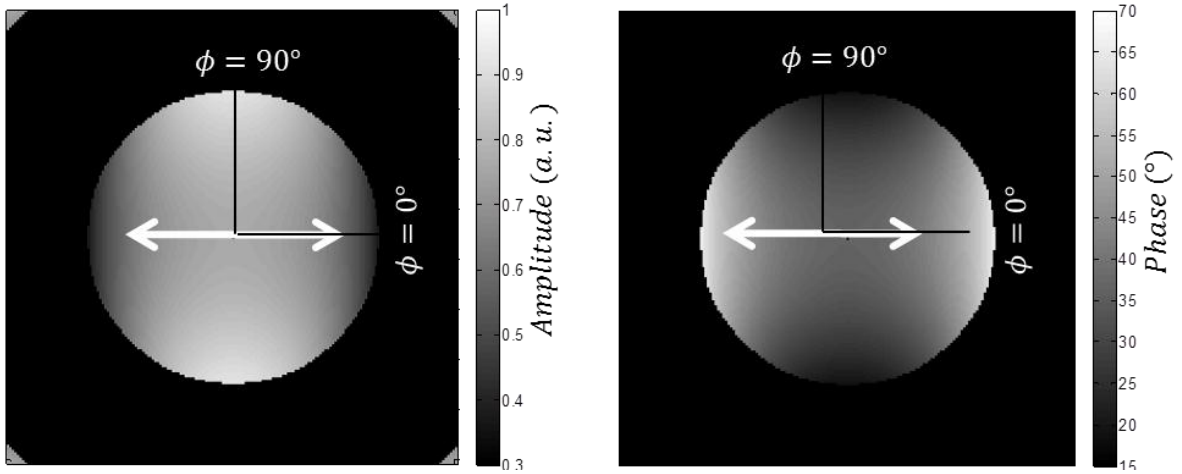


Figure 4.5 The reflected field E_0 (horizontal polarisation) in the back-focal-plane of the objective for gold sample; (a) amplitude variation and (b) phase variation

The phase error due to aberration $e^{j\Phi(r, \phi)}$ is assumed to be same for both E_0 and E_{90} . In Figure 4.5(a) and 4.5(b), the amplitude and phase variations of the reflected field E_0 due to a gold object are shown, respectively. The complex refractive index of the gold object is $\mathbf{n} = 0.27 + 3.01j$ measured by an ellipsometer. From equation 4.9, it is noted that the reflected field $E_0(r, 0^\circ) = A_0 e^{j\Phi(r, \phi)} \mathbf{r}_p$ and $E_0(r, 90^\circ) = -A_0 e^{j\Phi(r, \phi)} \mathbf{r}_s$, or in other words, the horizontal polarisation along $\phi = 0^\circ$ provides a completely p-polarised illumination

whereas, at $\phi = 90^\circ$, it becomes completely s-polarised as shown in Figure 4.5. In this way, the amplitude and phase variation for E_{90} are simply the respective patterns for E_0 , rotated 90° around the azimuth ϕ .

From equation 4.9 and 4.10, the ratio of the fields can be written as,

$$\frac{E_0(r,\phi)}{E_{90}(r,\phi)} = \frac{A_0}{A_{90}} \cdot \frac{r_p \cos^2 \phi - r_s \sin^2 \phi}{r_p \sin^2 \phi - r_s \cos^2 \phi} \quad (4.11)$$

Since, $1 + \cos 2\phi = 2 \cos^2 \phi$ and $1 - \cos 2\phi = 2 \sin^2 \phi$,

$$\frac{E_0(r,\phi)/A_0}{E_{90}(r,\phi)/A_{90}} = \frac{(r_p - r_s) + (r_p + r_s) \cos 2\phi}{(r_p - r_s) - (r_p + r_s) \cos 2\phi} \quad (4.12)$$

By elementary manipulation above, a ratio can be written as,

$$\frac{E_0(r,\phi)/A_0 - E_{90}(r,\phi)/A_{90}}{E_0(r,\phi)/A_0 + E_{90}(r,\phi)/A_{90}} = \frac{(r_p + r_s) \cos 2\phi}{(r_p - r_s)} \quad (4.13)$$

The real, imaginary, magnitude and phase-maps obtained from equation 4.13, in the back-focal-plane ($\theta_i^{max} \cong 58^\circ$) are shown in Figure 4.6(a), 4.6(b), 4.6(c) and 4.6(d), respectively. The real and imaginary images show a two-cycle variation, whereas, the magnitude (absolute) image shows a four-cycle variation. Interestingly, the phase-map variation is a square wave variation around azimuth ϕ between -85° to 95° as shown in Figure 4.6(d).

For high N_A objectives, aberrations can cause significant phase error, which affects the refractive index and subsequent phase offset measurement. Therefore, measurement of both the reflected fields E_0 and E_{90} is advantageous, so that an equation of the form of the ratio of the two can be obtained. The phase error $\Phi(r, \phi)$ due to aberrations is cancelled in equation 4.13 and effectively the ratio gives a result free from the phase errors due to aberrations of the optical system.

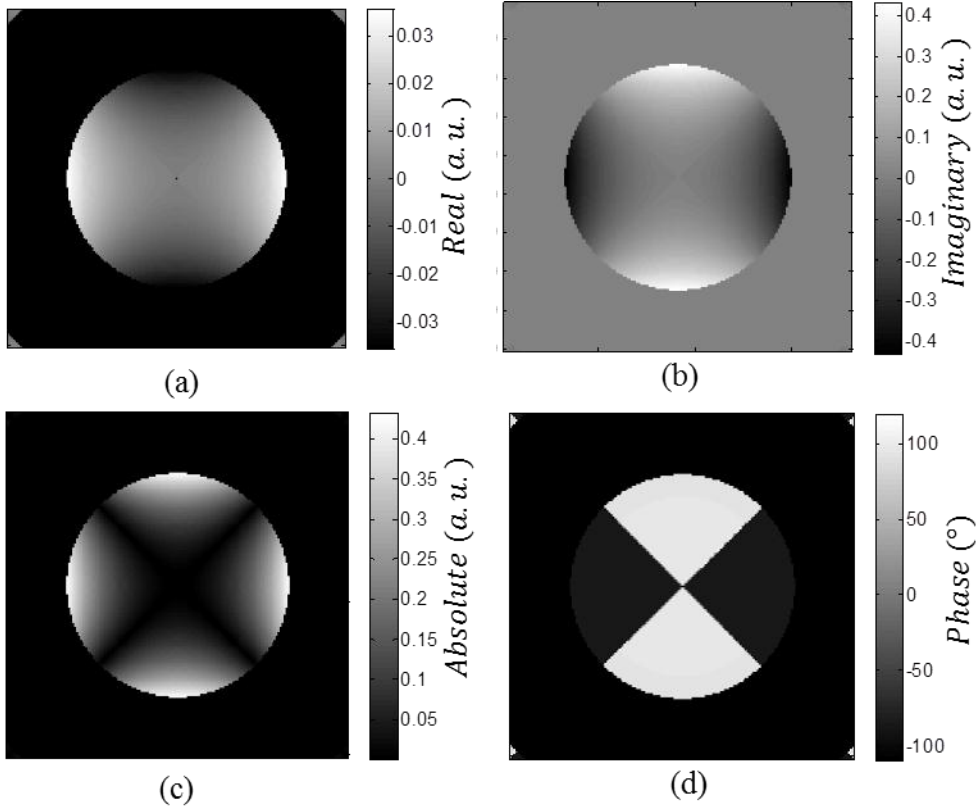


Figure 4.6 Variation of the ratio in equation 4.13 around the back-focal-plane for gold with an objective of $N_A = 0.85$ (a) real, (b) imaginary, (c) absolute and (d) phase

From the ratio in equation 4.13 in the Fourier domain the second cycle can be separated from the real and imaginary part to reduce the noise. After that at the perimeter of the back-focal-plane for $\phi = 0^\circ$ and $r = r_{max}$ equation 4.13 reduces to

$$\frac{E_0(r_{max}, 0^\circ)/A_0 - E_{90}(r_{max}, 0^\circ)(r, \phi)/A_{90}}{E_0(r_{max}, 0^\circ)/A_0 + E_{90}(r_{max}, 0^\circ)/A_{90}} = \frac{r_p(r_{max}, 0^\circ) + r_s(r_{max}, 0^\circ)}{r_p(r_{max}, 0^\circ) - r_s(r_{max}, 0^\circ)}$$

It is clear that at the perimeter, $r_p(r_{max}, 0^\circ) = r_p(\theta_i^{max})$ and $r_s(r_{max}, 0^\circ) = r_s(\theta_i^{max})$ and therefore, the above ratio can be written as,

$$\frac{r_p(r_{max}, 0^\circ) + r_s(r_{max}, 0^\circ)}{r_p(r_{max}, 0^\circ) - r_s(r_{max}, 0^\circ)} = \frac{r_p(\theta_i^{max}) + r_s(\theta_i^{max})}{r_p(\theta_i^{max}) - r_s(\theta_i^{max})} = \mathbf{z} \quad (4.14)$$

From the value of the complex number \mathbf{z} , the ratio of the reflection coefficients ρ is calculated as,

$$\frac{z+1}{z-1} = \frac{r_p}{r_s} = \tan \psi e^{j\Delta} \quad (4.15)$$

From equation 4.15, after obtaining the ratio of the reflection coefficients ρ , the complex refractive index \mathbf{n} can be calculated by equation 4.6.

The variations of the real and imaginary part of the ratio in equations 4.13 at the perimeter of the back-focal-plane is shown in Figure 4.7 for gold, silver and aluminium. Clearly, the real part of the ratio of silver is much less compared to the other metals, whereas, the imaginary part of the ratio according to descending order of values are, gold, silver and aluminium.

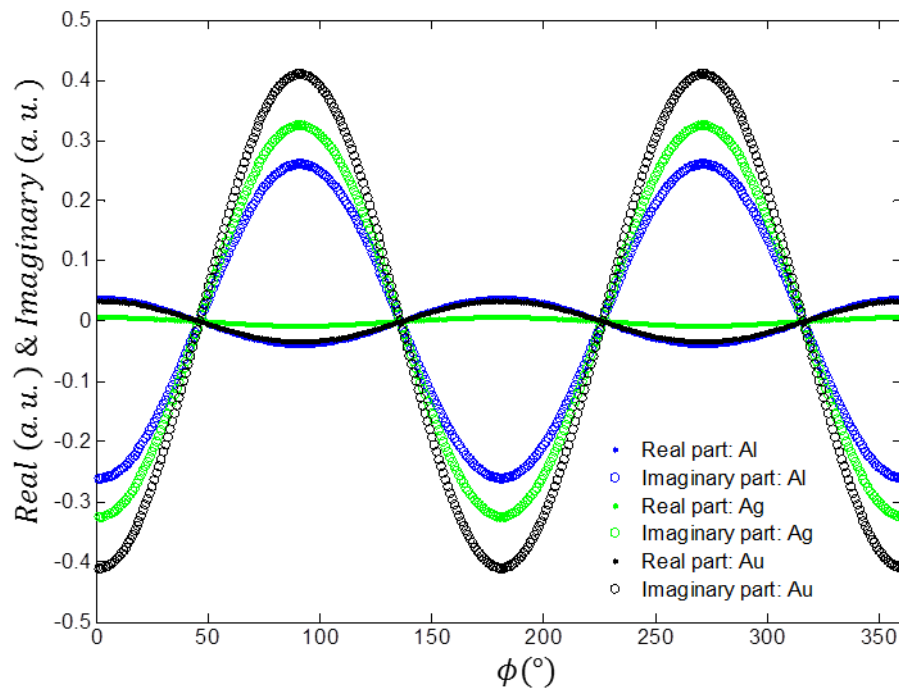


Figure 4.7 Real and imaginary part of the ratio of equation 4.13 at the extreme of the aperture for $N_A = 0.85$ with refractive indices obtained from ellipsometer

4.2.1 MICROELLIPSOMETRY SET-UP

The microellipsometry set-up with a He-Ne laser (wavelength $\lambda_0 = 0.633 \mu m$) is shown in Figure 4.8 [15]. The polariser P was used to control the illumination level of the laser and by rotating the half-wave plate ($\lambda/2$) the orientation of the plane of polarisation can be rotated. After the plane polarised light passes through the beam expander, lens L_1 collimates the beam and the plate beam-splitter (BS) divides the wavefront into two plane waves, one towards the reference mirror (M) and the other towards the objective. The objective (from Comar Optics – catalogue no. 60 OA 85, standard achromat corrected for spherical aberration in green ($546 nm$)) has high $N_A = 0.85$ with low focal length

(2.91 mm). The linearly polarised collimated light, therefore, gets focused on the metal coated sample placed at the focus of the objective.

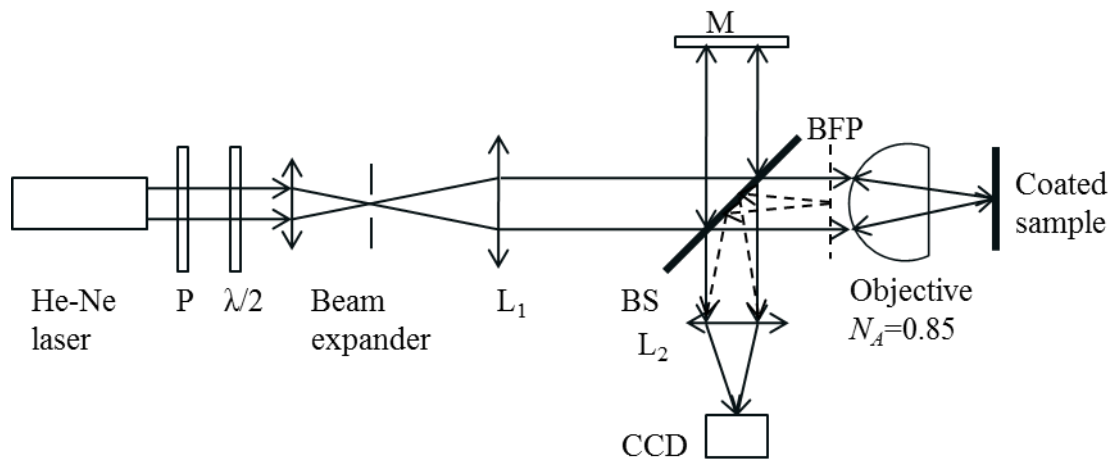


Figure 4.8 Microellipsometry set-up

The lens L_2 is focused at the back-focal-plane (BFP); therefore, in the CCD an interference pattern between the reference wave from M and the reflected field at the back-focal-plane is recorded. Circular fringes formed, initially, are used to align the optical axis. A tilt is given to the mirror to produce carrier modulated fringes as shown in Figure 4.9 and this interferogram is analysed to obtain the field measured at the back-focal-plane. From two interferograms in orthogonal polarisation, the ellipsometric parameters can be computed by measuring these fields (E_0 and E_{90}). The analysis method will be discussed below [14].

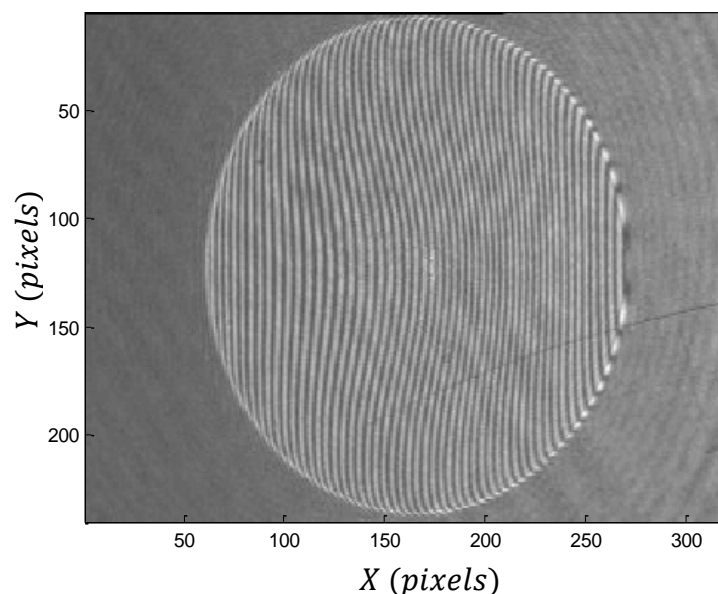


Figure 4.9 Interferogram modulated with carrier fringe for gold coated sample

By providing a tilt in the reference mirror, a titled plane wave is generated, which superposes with the wave coming from the back-focal-plane. Let us denote the field due to orthogonal polarisation (E_0 and E_{90}) as $E_p(x, y)$ and the reference beam with tilt as $E_r(x, y)$. If the intensity of the interferogram is $I(x, y)$ then it can be written as,

$$I(x, y) = |E_p(x, y)|^2 + |E_r(x, y)|^2 + E_p(x, y).E_r^*(x, y) + E_p^*(x, y).E_r(x, y)$$

Similar to the fringe pattern shown in Figure 4.10, without loss of generality, it can be assumed that the carrier fringes are along X-axis with a plane wave of carrier frequency u_c where the field of the titled reference wave is given by $E_r(x, y) = e^{j2\pi u_c x}$. Therefore, the above equation can be written as,

$$I(x, y) = C(x, y) + E_p(x, y)e^{-j2\pi u_c x} + E_p^*(x, y)e^{j2\pi u_c x} \quad (4.16)$$

where, $C(x, y) = |E_p(x, y)|^2 + |E_r(x, y)|^2$ is the dc term. By taking the Fourier transform along X-axis in both sides of the equation 4.16, the intensity in the spatial frequency domain $\tilde{I}(u, y) = \int_{-\infty}^{\infty} I(x, y)e^{j2\pi ux} dx$, can be expressed as,

$$\tilde{I}(u, y) = \tilde{C}(u, y) + \tilde{E}_p(u - u_c, y) + \tilde{E}_p^*(u + u_c, y) \quad (4.17)$$

where, $\tilde{\cdot}$ denotes the Fourier transform of the corresponding terms in spatial domain. Equation 4.17 is illustrated with Figure 4.10 when $\tilde{I}(u, y) = \tilde{I}(u, y_f)$ for a fixed y-coordinate y_f i.e. In Figure 4.10 therefore, y-coordinate is not mentioned explicitly.

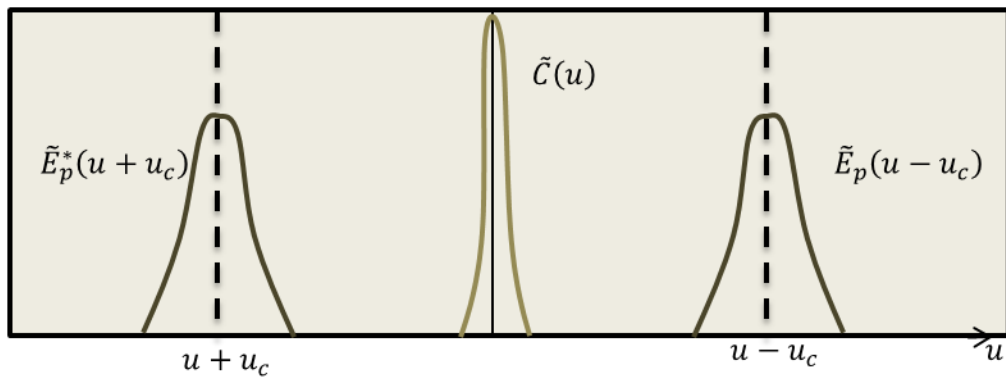


Figure 4.10 Fourier domain representation of the interferogram for fixed y-coordinate

The carrier frequency u_c due to the tilt of the reference wave needs to be more than the spatial bandwidth of $E_p(x, y)$ so that $\tilde{C}(u)$, $\tilde{E}_p(u - u_c)$ and $\tilde{E}_p^*(u + u_c)$ are separated

along the u -axis which is ensured by providing a large tilt. Using a bandpass filter $\tilde{E}_p(u - u_c, y)$ can then be selected and the inverse Fourier transform of that produces the demodulated field with carrier fringes $E_p(x, y)e^{-j2\pi u_c x}$. The demodulated field $E_p(u, y)$ is obtained both in magnitude and phase taking off the carrier fringes by multiplying it with $e^{j2\pi u_c x}$ for orthogonal polarisation (E_0 and E_{90}). By applying equation 4.14, the ratio of the reflection coefficients (ρ) is calculated from which by applying equation 4.6 and the refractive indices of the metal coated samples are computed.

4.2.2 RESULTS AND DISCUSSION

From the demodulated fields in orthogonal polarisation E_0 and E_{90} obtained from the carrier fringe analysis, first the amplitude of the demodulated fields were calculated over the image,

$$A_0 = \sum_{y=1}^{y_{max}} \sum_{x=1}^{x_{max}} E_0(x, y) / \Delta_x \Delta_y \quad (4.18)$$

$$A_{90} = \sum_{y=1}^{y_{max}} \sum_{x=1}^{x_{max}} E_{90}(x, y) / \Delta_x \Delta_y \quad (4.19)$$

where, $\Delta_x = x_{max} - 1$, $\Delta_y = y_{max} - 1$.

After obtaining the amplitudes of the demodulated fields, the ratio $\frac{\frac{E_0}{A_0} - \frac{E_{90}}{A_{90}}}{\frac{E_0}{A_0} + \frac{E_{90}}{A_{90}}}$ was computed. The real, imaginary, absolute and phase patterns of the ratio for gold sample are shown in Figure 4.11, which can be compared to the similar simulated patterns of Figure 4.6.

For the real and imaginary part, a two-cycle variation with respect to the azimuth is evident, though due to small values the real part is affected by noise much more compared to the imaginary part. The absolute part of the ratio shows a four cycle variation whereas phase shows a square wave variation with respect to azimuth ϕ . The variations become prominent as the radial co-ordinate increases which is consistent with the microellipsometry theory described in Section 4.2.

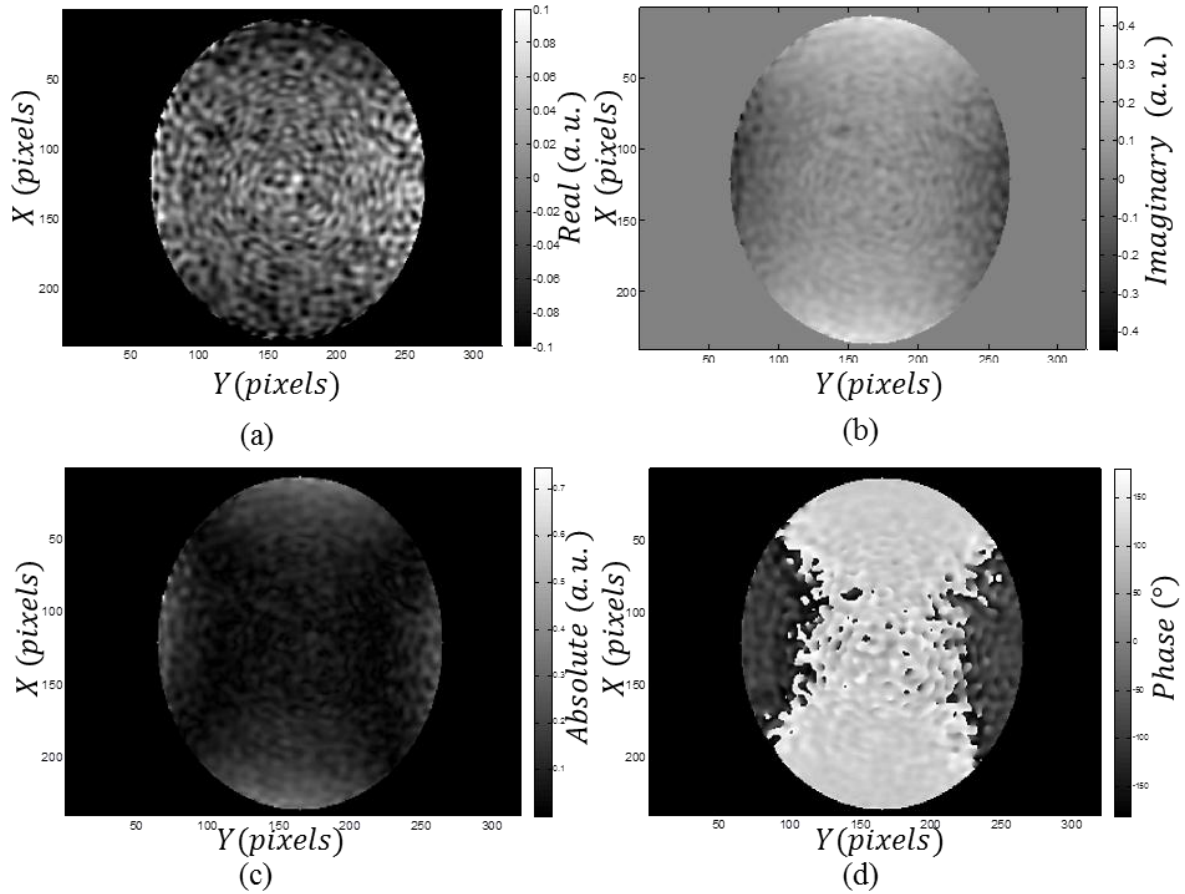


Figure 4.11 Experimental results of the variation of the ratio in equation 4.13 around the back-focal-plane for gold sample (a) real, (b) imaginary, (c) absolute and (d) phase

The demodulated real part and imaginary part of the ratio were then converted to polar coordinates to obtain the variations over the entire azimuth ($\phi = 0^\circ - 360^\circ$) and a third order polynomial was fitted to the radial dependence in the back focal plane. Since a two-cycle pattern over the azimuth is expected, these polar patterns are also filtered in the Fourier domain for the second cycle to remove noise. The filtering is done by 1D “fft” along azimuth (ϕ) direction and selecting out the 2nd cycle.

The polar real and imaginary part of the ratio for gold, calculated in this manner is shown in Figure 4.12(a) and 4.12(b), respectively. Figure 4.12(c) shows the plots of the same at the extreme of the aperture, which correspond to the maximum radius of Figure 4.12(a) and 4.12(b) (bottommost line) for all the samples i.e. gold, silver and aluminium. These plots can be compared to the similar phase difference plots derived from measurements of the refractive index from the ellipsometer in Figure 4.7.

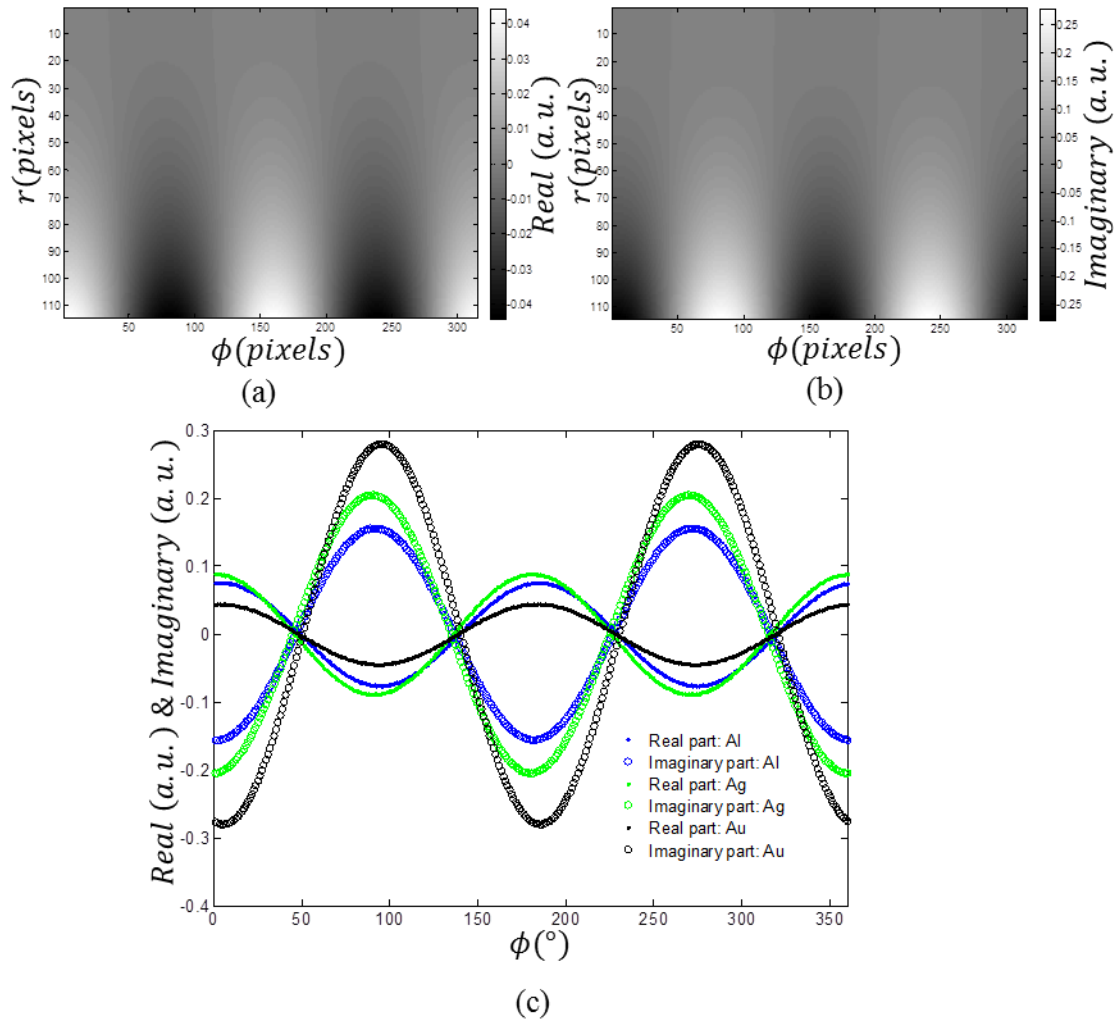


Figure 4.12 Polar images of the experimental results of the ratio in equation 4.13 for the gold sample, (a) the real part and (b) the imaginary part. (c) The real and imaginary parts of the ratio of equation 4.13 at the extreme of the aperture with refractive indices values obtained from microellipsometry

It can be seen that the phase values measured from microellipsometry experiments follow the correct trend but are consistently smaller than those predicted by the theory. The real and imaginary parts increase sharply with incidence angle and it is thought that the full N_A of the objective may not have been properly filled with the incident light. The experimental results fit well with the theory at $N_A = 0.76$. Secondly, due to the inaccuracies of the half-wave plate and polarizer, the starting of the periods of the plots in Figure 4.12(c) are not exactly multiples of $\pi/2$.

Table 4.1 shows the comparison of the complex refractive indices and phase offsets for all the samples calculated from microellipsometry experiments and from the ellipsometric

measurements [15]. The phase offset can be approximated to be the phase of the reflection coefficient at normal incidence for $N_A = 0.85$ given by [4],

$$\mathbf{r}_0 = \frac{n-1}{n+1} \quad (4.20)$$

In Table 4.1, the phase of \mathbf{r}_0 is given by $\arg(\mathbf{r}_0)$ in degrees.

Table 4.1. Comparison of complex refractive indices by microellipsometry and ellipsometry

Sample surface materials	Refractive index measured by micro-ellipsometry for 633 nm	Refractive index by ellipsometry measured for 633 nm	Phase offset from micro-ellipsometry (°)	Phase offset from ellipsometry (°)
Au	$0.51 + 3.01j$	$0.27 + 3.01j$	35.9	36.5
Ag	$1.62 + 3.60j$	$0.09 + 3.88j$	26.3	28.9
Al	$2.27 + 4.58j$	$0.74 + 4.76j$	20.0	23.2

Though good agreement can be seen for the imaginary part of the refractive index from both measurements, some discrepancy is observed in the real part. This is due to the amplitude noise generated from the reference wave coming from the mirror and this introduces errors in the calculation of A_0 and A_{90} in equation 4.18 and 4.19. This affects the real part of the refractive index more than the imaginary part. Despite this variation in real part, the imaginary part is close to the ellipsometric value. The phase offsets for both measurements show good agreement with $\sim 3^\circ$ phase variation for each of the samples, which corresponds to $\sim 3 \text{ nm}$ height variation from the predicted height offset. Therefore, the measured phase offset obtained from microellipsometry experiments remains accurate within experimental limit. To find out the reasons for this, one needs to simplify the normal reflection coefficient. The phase obtained from perpendicular reflection coefficient from complex refractive index after rationalisation can be written as,

$$\mathbf{r}_0 = \frac{n-1}{n+1} = \frac{(a+jb-1)}{(a+jb+1)} = \frac{a^2+b^2-1}{(a+1)^2+b^2} + j \frac{2b}{(a+1)^2+b^2} \quad (4.21)$$

where, a and b are the real part and imaginary part of the refractive index, respectively. The real part a is much smaller than the imaginary part b for metals.

Therefore the phase obtained from equation 4.21 can be written as,

$$\phi \approx \tan^{-1} \frac{2b}{b^2-1} \quad (4.22)$$

This shows that phase is not dependent on the real part. Therefore, even if the real part is not accurate still the phase remains sufficiently accurate to estimate height.

Though microellipsometry offers high spatial resolution and accurate measurement of surface height offset, it suffers from the fact that it is a single point technique. In this case, the surface needs to be laterally scanned to build a map of the phase offset and true topography of the surface cannot be measured from this technique. Next, the ways to extend microellipsometry to *whole-field* measurement will be explored. If the measurement of the refractive index can be used to calculate the phase change observed while measuring the topography of metallic surfaces by CSI, then whole-field measurement of absolute surface profile for a composite surface is possible.

4.3 WHOLE-FIELD MEASUREMENT TECHNIQUE OF PHASE OFFSET BY OBLIQUE ILLUMINATION

From the above results, it is clear that the transverse modulation at large angles of incidence is estimated from the change in phase at a single point in the back focal plane for orthogonal polarisation. Here, transverse modulation refers to the variation of phase with respect to azimuth ϕ . The measurement is termed as the single point measurement and the entire back-focal-plane is illuminated with a collimated beam as shown in Figure 4.13(a). Exactly the same information can be retrieved, however, if the sample is *illuminated* by an oblique plane wave and the phase and amplitude of the scattered field is *measured* at all points in the back focal plane as illustrated in Figure 4.13(b). This reverse configuration has the advantage that the point of interest can be selected by multiplying the measurements by an appropriate phase mask and integrating. The reverse configuration is, therefore, a *whole-field* implementation of microellipsometry.

CSI can be considered to be a holographic method that records an interferogram that is a combination of holographic recordings made with plane wave illumination at different angles of incidence and different wavelengths as described in Chapter 3 [16]. Unfortunately, it is not generally possible to separate individual holographic recordings from a CSI

interferogram unless either the spatial frequency content of the illumination field or the measured field is modified.

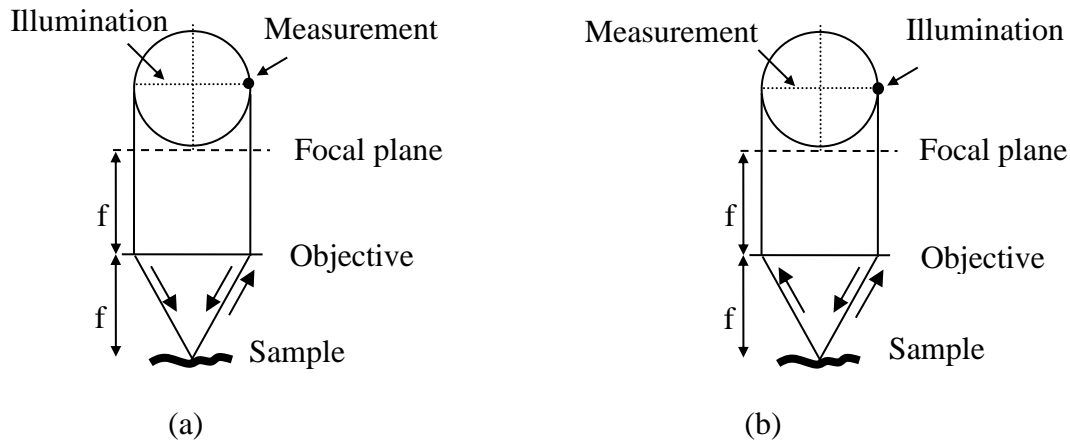


Figure 4.13 Simplified configurations; (a) single-point, (b) whole-field [15]

A configuration similar to CSI capable of the measurement task performed by microellipsometry is shown in Figure 4.13(b). The configuration retains the focused illumination that defines the point of interest on the sample but only the phase of a single, oblique plane wave component of the scattered field is measured. In this way, a CSI instrument would scan the sample through the focus of a conventional Mirau objective for orthogonal polarisation and from the phase difference of the fringe pattern generated in horizontal and vertical polarisations, the phase offset could be computed. Leonhardt *et al* have presented a similar technique with a different analysis method [17, 18].

4.3.1 MODIFIED CSI WITH LASER ILLUMINATION

The modified CSI set-up with a He-Ne laser source is shown in Figure 4.14. The polariser (P) was used to control the illumination and the half-wave plate ($\lambda/2$) rotates the plane of polarization, in a similar way to the microellipsometry set-up. The beam expander collimates the laser beam and the lens (L) is used to focus the beam on the edge of the back-focal plane of the Mirau objective of $N_A = 0.5, \theta_i^{max} = 30^\circ$ (the Mirau objective is a finite conjugate).

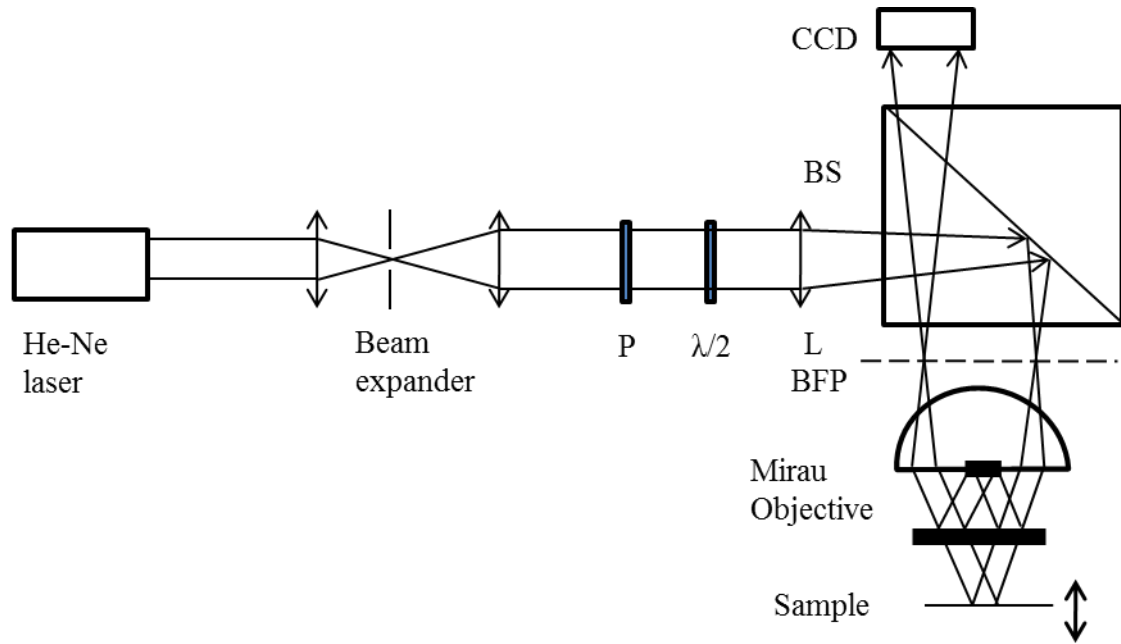


Figure 4.14 Modified CSI system with laser illumination

The light focused in the back focal plane of the Mirau objective formed an oblique plane wave and was used to illuminate a gold coated glass sample. The reference beam coming from the reflector within the Mirau objective and the reflected light from the sample of the object interfere and the resultant fringe pattern was projected onto a CCD. The sample was moved vertically by a piezo-stage to scan it through the focus of the Mirau objective rendering a video interferogram. Two videos were recorded for orthogonal polarisation with the same start and end-height and analysed to find out the surface topography and the phase offset.

4.3.1.1 RESULT AND DISCUSSION

The video is a 3D matrix of stacks of interferograms for a particular polarisation produced by the scan along the vertical direction, considered as the Z -axis with reference to Figure 4.15. If the unit vector along the Z -axis is \hat{z} and the wavelength of the He-Ne source is $\lambda_0 = \frac{1}{k_0} = 0.633 \mu m$, then the spatial frequency of the oblique plane wave is $k_i = \vec{k}_i \cdot \hat{z} = k_0 \cos \theta_i^{max} = 0.87k_0$. The effective wavelength of the reference wave along Z -axis, therefore, is given by $\lambda_i = \frac{1}{k_i} = \frac{\lambda_0}{0.87} = 0.727 \mu m$.

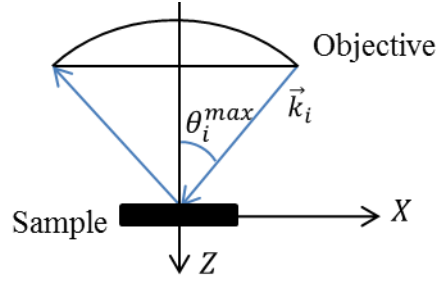


Figure 4.15 The spatial frequency of the oblique plane wave

The reflected wave from the flat sample, after superposition with the reference wave, will be the recorded interference pattern $I(x, y, z)$, which for a particular pixel (x_0, y_0) is shown in Figure 4.16(a) along Z -axis. The steps of the vertical stage of resolution $0.1 \mu\text{m}$ are effectively sampling the fringe data of fringe frequency of $\frac{\lambda_i}{2}$ along Z -axis. The scanning speed was adjusted such that at least 3 frames per cycle is obtained to meet the Nyquist requirement. If the reference field is given by a plane wave $e^{-j2\pi\vec{k}_i \cdot \vec{z}}$, emanating from the reflector of the Mirau objective in a similar manner to equation 4.16, the intensity $I(x, y, z)$ can be expressed as,

$$I(x, y, z) = C(x, y, z) + E_p(x, y, z)e^{-j2\pi\vec{k}_i \cdot \vec{z}} + E_p^*(x, y, z)e^{j2\pi\vec{k}_i \cdot \vec{z}} \quad (4.23)$$

where, $C(x, y, z)$ is the dc term and $E_p(x, y, z)$ is the reflected field for orthogonal polarisation. By taking the Fourier transform of $I(x, y, z)$, in the spatial frequency domain the intensity $\tilde{I}(k_x, k_y, k_z)$ can be expressed as,

$$\tilde{I}(k_x, k_y, k_z) = \tilde{C}(k_x, k_y, k_z) + \tilde{E}_p(k_x, k_y, k_z - k_i) + \tilde{E}_p^*(k_x, k_y, k_z + k_i) \quad (4.24)$$

where, k_x, k_y, k_z ($k_x = \frac{1}{\lambda_x}$ etc) are spatial frequencies along X, Y and Z-axis, respectively.

Since the modified CSI is illuminated by a He-Ne laser, $\tilde{I}(k_x, k_y, k_z)$ is modulated in the Z -direction by a carrier frequency $k_z = k_i$ as shown in Figure 4.16(a) and 4.16(b). After selecting the plane $k_z = k_i$, the field can be written as $\tilde{E}_p(k_x, k_y, k_i)$. The carrier frequency k_i is a constant; therefore, according to the shift theorem, inverse Fourier transform of $\tilde{E}_p(k_x, k_y, k_i)$ produces a 3D interference pattern $E_p(x, y)e^{-j2\pi\vec{k}_i \cdot \vec{z}}$ [12]. Here, the reflected field $E_p(x, y)$ is modulated in Z -axis by a sinusoid $e^{-j2\pi\vec{k}_i \cdot \vec{z}}$. From this 3D interference

pattern, a particular frame at $z = z_0$ (30th frame) is selected along Z-axis (selected for relatively low noise surface height maps) and at this frame the field is given by $E_p(x, y)e^{-j2\pi k_i z_0}$. The factor $e^{-j2\pi k_i z_0}$ adds a constant phase to $E_p(x, y)$ and the field $E_p(x, y)$ that retains the phase and amplitude information can be estimated. This operation is performed for both horizontal and vertical polarisations and the respective reflected field are denoted as $E_p^h(x, y)$ and $E_p^v(x, y)$. The phase of the fields for each polarisation are obtained just by taking the argument of $E_p^h(x, y)$ and $E_p^v(x, y)$, respectively.

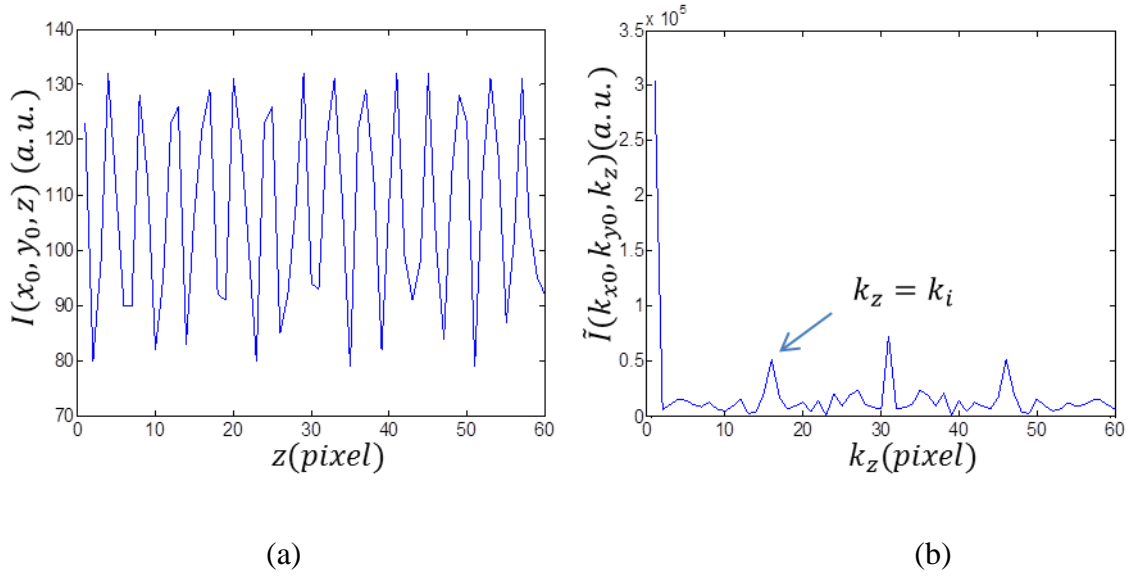


Figure 4.16 (a) Intensity along z-direction for a particular pixel and (b) absolute value of intensity along k_z (peak at 16th plane, $k_z = k_i$); both diagrams are for horizontal polarisations

The phase map for $E_p^h(x, y)$ is converted in terms of height variation by multiplying the phase map with the proportionality constant $\frac{\lambda_i}{4\pi}$ as shown in Figure 4.17. This height variation map is not surface topography since it has an arbitrary phase factor added to it. The presence of high frequency ripples is quite evident in Figure 4.17, especially on the glass surface. This is due to the high coherence length of the He-Ne laser source, which causes back reflection from the glass surfaces.

In figure 4.18, the polarisation of the beam in the back focal plane of the Mirau objective is presented schematically. Clearly, if the incident field amplitude for both the polarisations is given by E_0 then, the reflected fields $E_p^h(x, y)$ and $E_p^v(x, y)$ can be written as,

$$\left. \begin{aligned} E_p^h(x, y) &= \mathbf{r}_p \cdot E_0 \cdot e^{-j2\pi k_i z_0} \\ E_p^v(x, y) &= \mathbf{r}_s \cdot E_0 \cdot e^{-j2\pi k_i z_0} \end{aligned} \right\} \quad (4.25)$$

including the constant phase factor within the expressions.

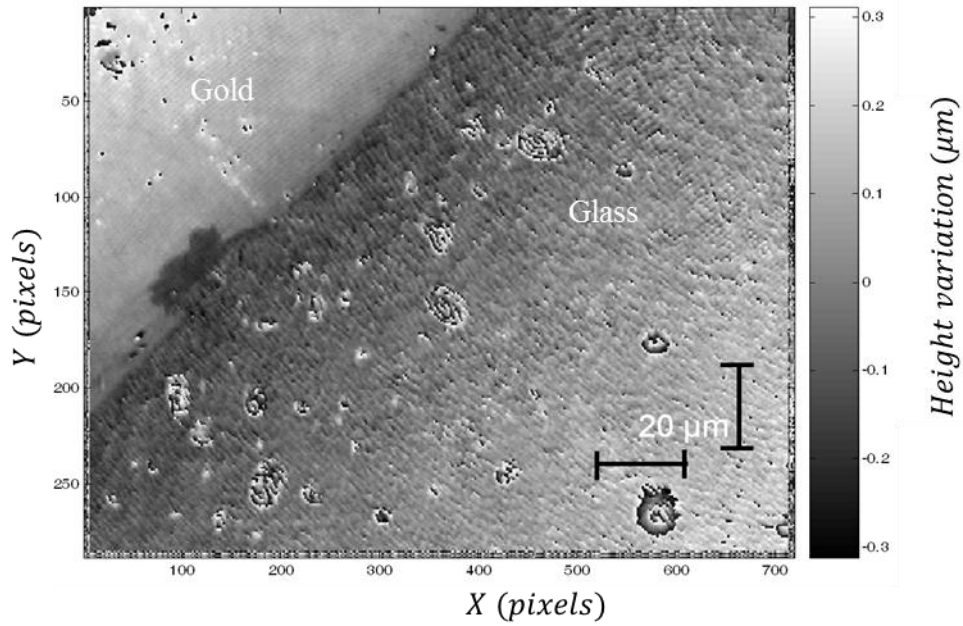


Figure 4.17 Height variations in horizontal polarisation of gold interface

For illumination with the horizontal polarisation the orientation is along the p – component whereas for the vertical polarisation, it is along the s – component. The reflected beams for both of these cases are, therefore, linearly polarised. Two sets of the phase maps for $E_p^h(x, y)$ and $E_p^v(x, y)$ were generated both of which have same phase factor. Therefore, subtracting the two phase maps will produce the phase difference of complex reflection coefficients r_p and r_s which at an incidence angle 30° is about 10.7° . The phase factor being same for both the cases, does not affect the phase difference. Compared to the phase difference for a gold surface, the phase shift from glass is theoretically zero.

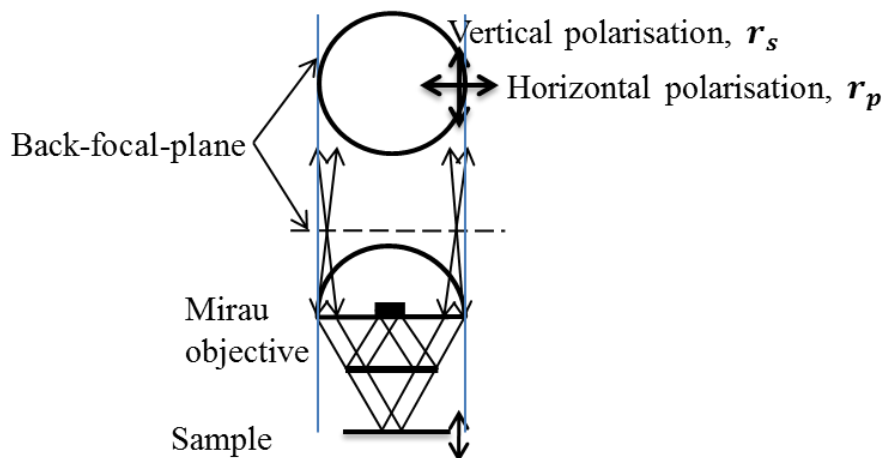


Figure 4.18 The orientations of the incident polarisations in the back-focal-plane

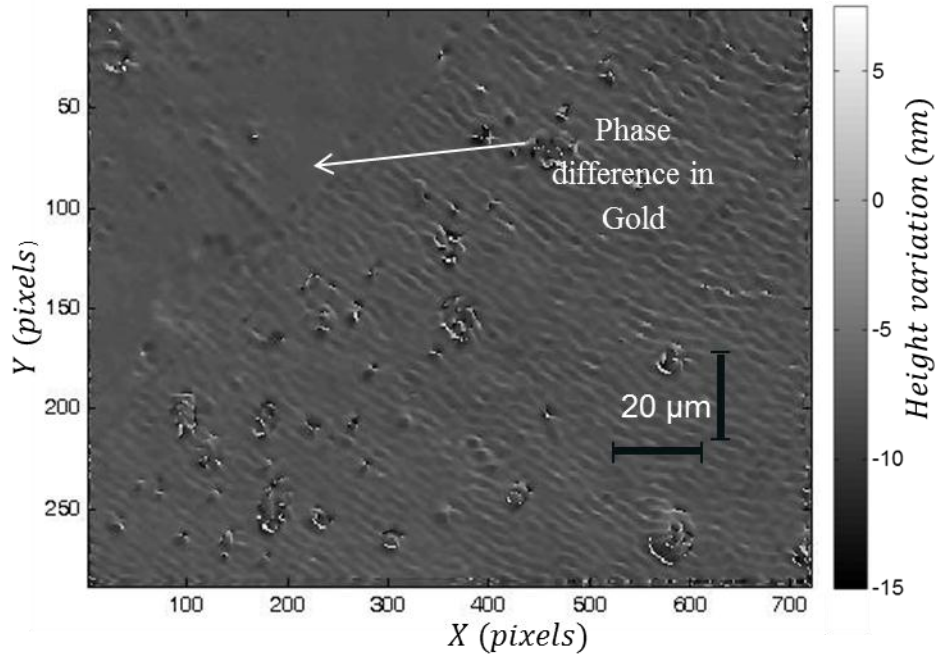


Figure 4.19 Relative height difference between gold and glass surface

The relative phase difference can again be converted to height difference by multiplying $\frac{\lambda_i}{4\pi}$ and for gold it is about 10.8 nm corresponding to a phase difference of 10.7° . Figure 4.19 shows this relative height difference for the gold interface. The height difference varies between $10 \text{ nm} - 15 \text{ nm}$ and it is not clear enough throughout the gold surface. This discrepancy is due to the ripples, which contribute to the phase noise that makes part of the glass surface to appear higher than expected. In the next section the same set-up was built with an LED source (broad-band light) and better results were obtained due to the absence of the ripples.

4.3.2 MODIFIED CSI WITH INCOHERENT ILLUMINATION

In Section 4.3.1, a whole-field method using a Mirau objective with an oblique illumination set-up with He-Ne laser was discussed in detail. The phase maps, obtained from orthogonal polarisations, had multiple ripples and the phase offset map was not constant over the entire metal surface. These ripples were caused by interference between back-reflected waves from glass surfaces due to the high coherence length of the He-Ne laser source. Use of a low coherent source reduces this noise and provides a much better surface profile. The previous set-up though provides the phase offset of the metal surface, but the true surface topography cannot be obtained from the result. Therefore, a similar experimental set-up with

an LED source is now discussed. Leonhardt *et al* also published two similar papers on this topic already mentioned [17, 18], which came to my notice after the initial experimental results were obtained.

The experimental set-up of this modified CSI is similar to the whole-field with oblique illumination set-up (Figure 4.14) but with an LED source with central wavelength $\lambda_m = 635 \text{ nm}$ with a spectral width of $\Delta\lambda = 40 \text{ nm}$. Since, in this case $N_A = 0.5$ is not very high, from Section 2.2, the central wavelength is assumed to be the effective wavelength $\bar{\lambda}$. Here, a flat sample is illuminated by an oblique plane wave from the back-focal-plane and two interferograms are recorded for orthogonal polarisations. The intensity recorded $I(x, y, z)$ can be thought of as superposition of the reflected field from the object comprised of a gold-glass interface $E_p(x, y, z)$ and from the reference field from the reflector of the Mirau objective $E_r = e^{-j2\pi\vec{k}_i\cdot\vec{z}}$, which is just an oblique plane wave. Therefore, the intensity $I(x, y, z)$ is given by,

$$I(x, y, z) = C(x, y, z) + \int_{-\infty}^{\infty} S(k_0)E_p(x, y, z)e^{-j2\pi\vec{k}_i\cdot\vec{z}}dk_0 + \int_{-\infty}^{\infty} S(k_0)E_p^*(x, y, z)e^{j2\pi\vec{k}_i\cdot\vec{z}}dk_0 \quad (4.26)$$

where, $C(x, y, z)$ is the dc term and $S(k_0)$ is the spectral variation of the LED source in general can be considered to be Gaussian function w.r.t the spatial frequency.

From equation 4.26, it is evident that for the case of broad-band LED illumination, the interferogram is a simultaneous superposition of the object wave and the reference wave in all wavelengths. After the usual frequency domain filtering as described in Section 4.3.2, the complex interference term $\int_{-\infty}^{\infty} S(k_0)E_p(x, y, z)e^{-j2\pi k_i z}dk_0$ was obtained. This is plotted in magnitude, an envelope and phase, a ramp between π to $-\pi$, for a particular pixel along Z -axis in Figure 4.20. The position of the peak magnitudes closest to zero phase positions for all pixels are computed to get the surface topography as discussed in Section 2.3.3. In this case for horizontal polarisation the position is at Z -frame $z_0 = 188$, where the phase is 0.0278 rad and the envelope for horizontal polarisation is given by,

$$I_{fh}(x_0, y_0, z) = \left| \int_{-\infty}^{\infty} S(k_0)E_p(x_0, y_0, z)e^{-j2\pi k_i z}dk_0 \right| \quad (4.27)$$

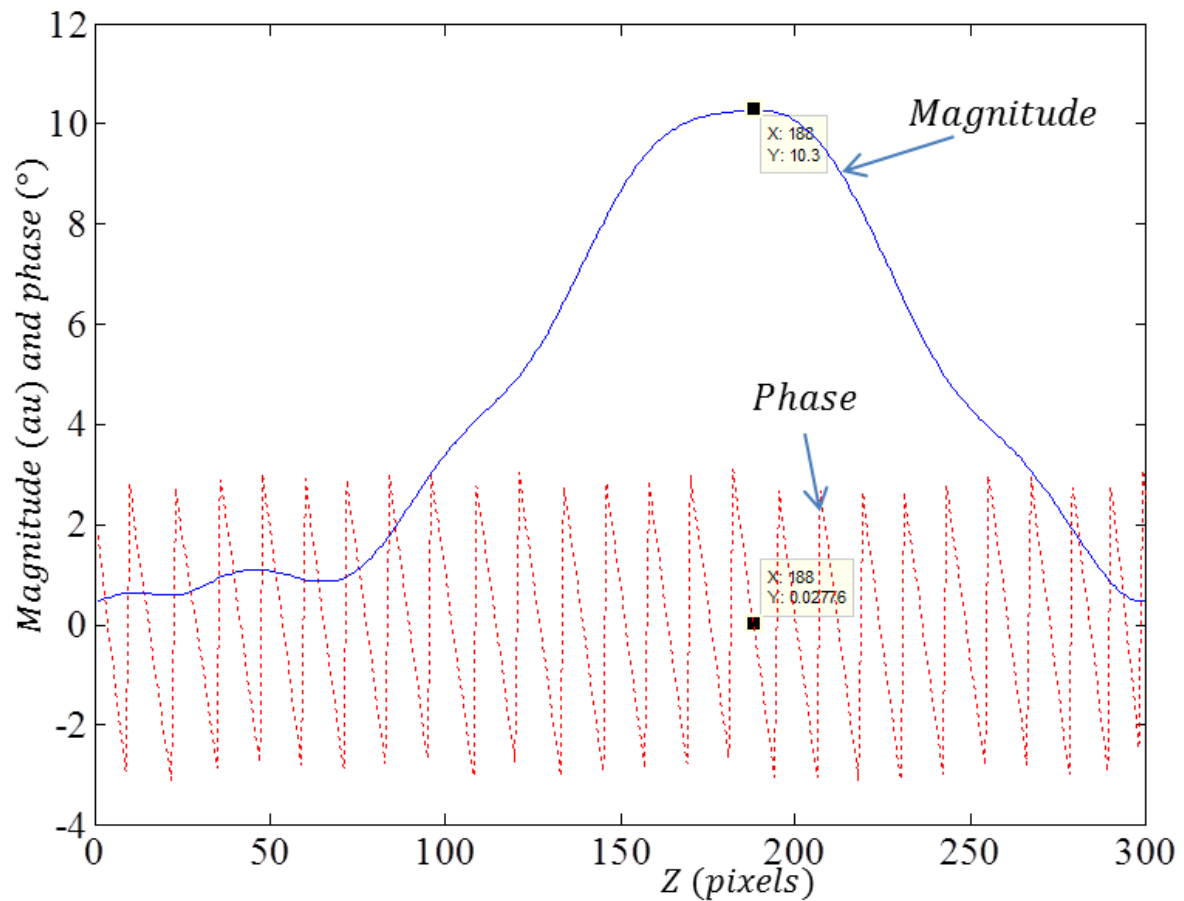


Figure 4.20 Magnitude and phase pattern of the interferogram along z-direction for a pixel

In this way, the surface topography map of the gold interface for horizontal polarisation is shown in Figure 4.21. Unlike the interferogram obtained by whole-field method with laser illumination, in this case with broadband, finding the peak of the envelope provides an accurate measurement of the surface profile. According to the Figure 4.21, the gold surface is about 300 nm above the glass surface and the presence of ripples is significantly reduced. Therefore, the phase noise is less in the topography measurement in Figure 4.21, as expected.

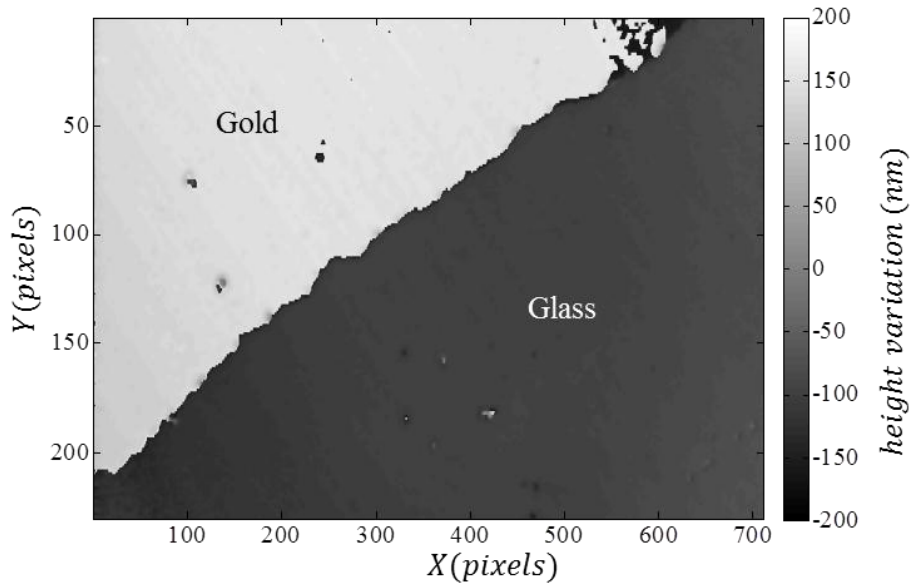


Figure 4.21 Surface height map of gold interface

In a similar manner, the surface topography for vertical polarisation where the peak of the envelope termed as, $I_{fv}(x, y, z_0)$, can be computed. Subtracting these two topographies one can obtain the relative height difference of gold surface assuming negligible height change in the dielectric glass surface. As discussed in Section 4.3.1.1 from the phase difference of r_p and r_s , theoretically expected height difference for gold is 10.8 nm . About $10 \text{ nm} - 15 \text{ nm}$ of height difference is obtained with this experiment as shown in Figure 4.22.

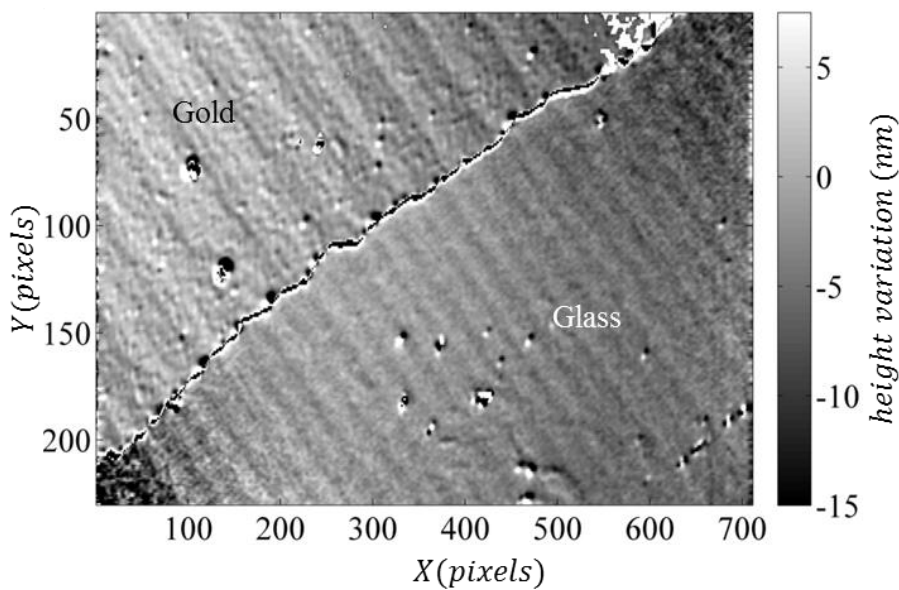


Figure 4.22 Relative height difference between gold and glass surface

Though this matches within experimental error, the result is still not uniform over the entire gold surface. This is due to the fact that sample scan due to orthogonal polarisations are taken separately (with the same start and end position) and potentially vibration and scan movement related errors affect the interferograms separately, resulting in a non-uniformity of phase errors.

CONCLUSION

This chapter discusses the measurement of phase offset due to metallic surface by microellipsometry. Microellipsometry being a single-point technique builds the phase map of a surface by means of lateral scan. A whole-field method with oblique laser illumination from back-focal-plane with polarisation sensitivity was discussed extending the concept of microellipsometry. Both of these techniques can only measure the relative phase difference between orthogonal polarisations. The system with laser illumination suffers from phase noise errors or ripples due to interference between back-reflected glass surfaces. An LED source was later used to determine the true surface topography since that would generate a localised fringe pattern close to the surface. This broadband illumination would also reduce the phase noise. The new set-up is called as polarisation sensitive modified CSI with incoherent illumination that has the capability to measure the surface topography of composite surfaces together with relative phase difference. This new set-up was affected by vibration and mechanical errors due to scan movement. In the next chapter, therefore, a rotationally symmetric polarisation sensitive CSI system with orthogonal circular polarisations set-up is proposed that will reduce all of these errors and a quantitative measurement of the phase offset over the entire object surface with multiple materials will be possible.

REFERENCE

1. R. M. A. Azzam and N. M. Bashara, *Ellipsometry and polarized light*, (North-Holland Publishing Company, 1977).
2. M. Born and E. Wolf, *Principles of Optics*, (Cambridge University Press, 1999).
3. C. W. See, M. G. Somekh and R. D. Holmes, "Scanning optical microellipsometer for pure surface profiling", *Applied Optics*, 35, 34 (1996), 6663- 6668.
4. G. D. Feke, D. P. Snow, R. D. Grober, P. J. de Groot and L. Deck, "Interferometric back focal plane microellipsometry", *Applied Optics*, 37, 10 (1998), 1796-1802.
5. K. Leonhardt, H. Jordan and H. J. Tiziani, "Micro-Ellipso-Height-Profilometry", *Optics Communications*, 80, 3 (1991), 205-209.
6. Q. Zhan and J. R. Leger, "Microellipsometer with radial symmetry", *Applied Optics*, 41, 22 (2002), 4630-4637.
7. R. H. Muller and J. C. Farmer, "Fast, self-compensating spectral-scanning ellipsometer", *Review of Scientific Instruments*, 55, 3 (1984), 371-374.
8. Y. T. Kim, R. W. Collins, and K. Vedam, "Fast scanning spectroelectrochemical ellipsometry: In-situ characterization of gold oxide", *Surface Science*, 233 (1990), 341-350,
9. H. Fujiwara, *Spectroscopic Ellipsometry: Principles and applications*, (John Wiley & Sons. Ltd, 2007)
10. K. Vedam, "Spectroscopic ellipsometry: a historical overview," *Thin Solid Films*, 313-314 (1998), 1-9.
11. K. Vedam, "Characterization of defects in real surfaces by ellipsometry," *Surface Science*, 56 (1976), 221-236.
12. E. Hecht, *Optics*, (Pearson Education, 2008).
13. D. Goldstein, *Polarised Light*, (Marcel Dekkar Inc., 2003)
14. T. Kreis, *Handbook of holographic interferometry*, (John Wiley & Sons. Ltd, 2005)
15. K. Palodhi, J. M. Coupland and R. K. Leach, "Measurement of complex refractive index using microellipsometry and its relevance to surface measurement using coherence scanning interferometry", *Met&Props, Metrology and Properties of Engineering Surfaces*, London, 2011
16. J. M. Coupland and J. Lobera, "Holography, tomography and 3D microscopy as linear filtering operations," *Measurement Science and Technology*, 19 (2008), 1-12.
17. K. Leonhardt, U. Droste and H. J. Tiziani, "Interferometry for ellipso-height-topometry part 1: Coherence scanning on the base of spatial coherence", *Optik*, 113, 12 (2003), 513-519.
18. K. Leonhardt, "Interferometry for ellipso-height-topometry part 2: Measurement of the ellipsometric data, material identification, and correction of the measured height", *Optik* 121 (2003), 623-632.

CHAPTER 5: POLARISATION SENSITIVE COHERENCE SCANNING INTERFEROMETRY

INTRODUCTION

In the previous chapter the experimental set-ups presented used linearly polarised light to obtain the phase introduced on reflection from metallic samples. Both the single-point technique of microellipsometry and a whole-field CSI configuration with oblique illumination were examined. The disadvantage of microellipsometry was the need for lateral scanning of the sample to build the height map. For the case of CSI with oblique illumination tilt of the sample can result in reflected light not reaching the detector and no measurement will be obtained. Therefore, a new configuration of CSI, called polarisation sensitive coherence scanning interferometry (PS-CSI) was investigated. PS-CSI uses circular polarisation which has the advantage of being rotationally symmetric and consequently, it eliminates the need of oblique illumination from a point at the back focal plane of the Mirau objective. The configuration is quite straight forward to achieve in practice.

This set-up contains two configurations of orthogonal polarisations. In the first, the sample is effectively kept within crossed circular polarisers and this is referred to as the “block” case. Circular polarisers are kept in uncrossed position for the second configuration and this is referred to as the “pass” case. This configuration has been used in a polarisation microscope known as Pol-scope by Inoue, Shribak and Oldenborge, used a similar crossed circular polarisation to measure birefringence of biological tissues and to identify grain boundaries of metals in an alloy [1-3]. The interferograms are recorded at each height step of the sample as the sample is scanned sequentially between these two configurations. Comparing these two cases first refractive indices, and subsequently, the phase offset introduced upon reflection at each point on the object can be calculated and. The phase offset will be compensated to provide the true surface topography.

5.1 EXPERIMENTAL SET-UP

The experimental PS-CSI set-up is shown in Figure 5.1. Two LED sources (details given in Appendix) with the same spectral characteristics – a central wavelength at 635 nm with a bandwidth of $\pm 20\text{ nm}$ are used. Light from both LEDs pass through diffusers (D1 and D2) and the beams are collimated by collimating lenses (L1 and L2). The collimated beams pass through the polarisers (P1 and P2) and are incident on the pellicle beam splitter BS1. The beams pass through the quarter wave plate, a Fresnel Rhomb (FR1) in this case, and are incident on the second pellicle beam splitter (BS2). Köhler illumination is used for the set-up and consequently, the diffusers are imaged ($D1'$ and $D2'$) at the back focal plane. Each point in the back focal plane acts as an incoherent source and the sample is illuminated with all possible plane waves within the numerical aperture of the Mirau objective. The reflected plane waves from the sample within the objective passes through the BS2 and second Fresnel Rhomb (FR2) to render the fringe modulated image (component details in Appendix).

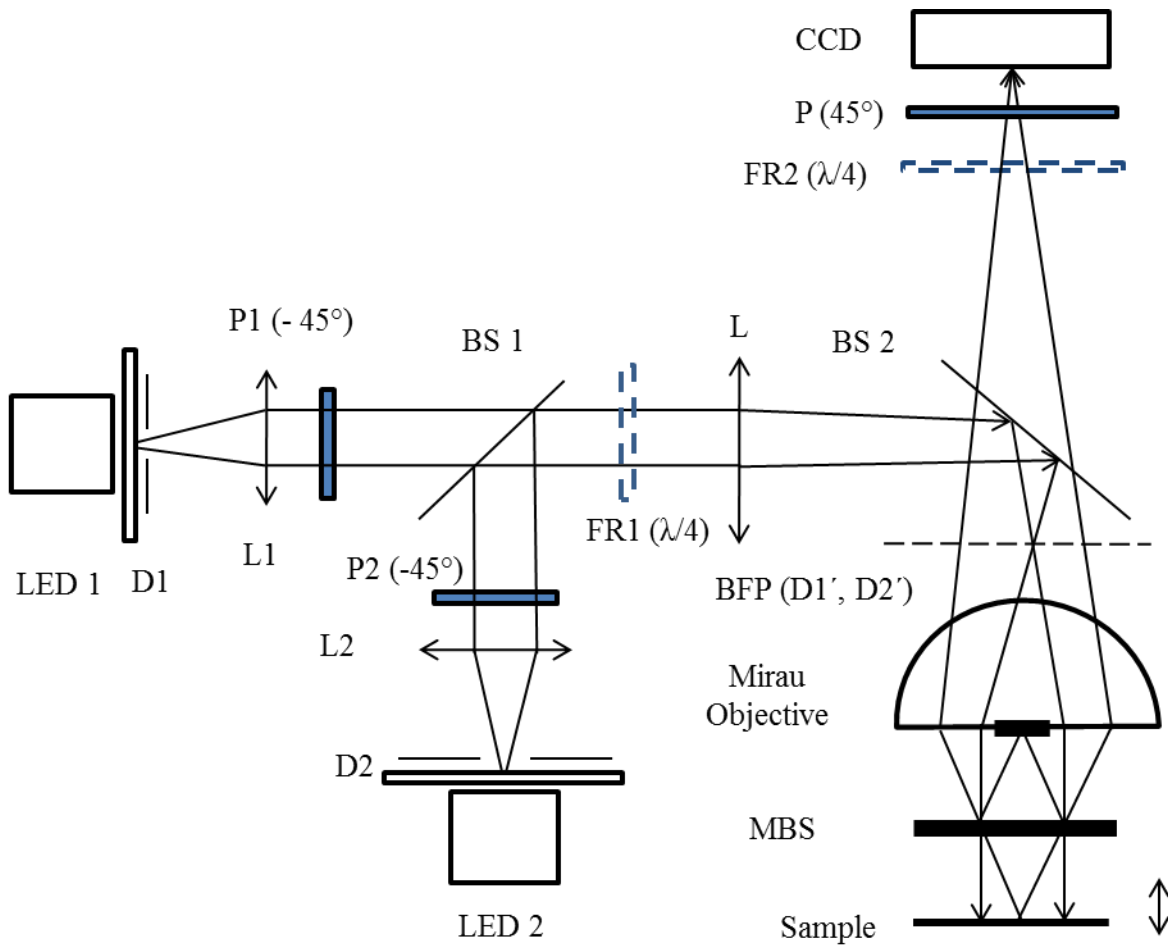


Figure 5.1 Polarisation sensitive coherence scanning interferometer (PS-CSI)

The polarisation states for metallic samples at the centre and at the edge of the aperture, for both block and pass configuration are illustrated in Figure 5.2 and Figure 5.3, respectively. The illumination arm containing LED1 is linearly polarised at -45° (Figure 5.2) by polariser P1. After passing through the FR1, it becomes right circularly polarised (RCP) due to phase introduced to the p-component. The RCP beam becomes left circularly polarised (LCP) by reflection from BS2 and is focussed at the back-focal-plane of the Mirau objective. At each point in the back focal plane, incident circularly polarised light ensures the rotational symmetry of the set-up. For normal incidence the reflected beam from both metals and dielectrics becomes RCP, therefore, the reflected beam at the centre becomes RCP whereas the reflected beams for all other angles become right elliptically polarised (REP). The ellipticity of the polarisation increases with increase in angle of reflection, which means that the ellipticity is more at the edge of the beam cross-section [4, 5]. The combination of quarter-wave plate (FR2) followed by the linear polariser (P) at 45° blocks any RCP passing through it and lets LCP through. Therefore, the central part of the reflected beam (RCP) would be blocked from CCD but REP beam from the edge of the aperture passes through forming the image superposed with the fringe pattern on the CCD. The image brightness will be low since a significant central part of the light is blocked.

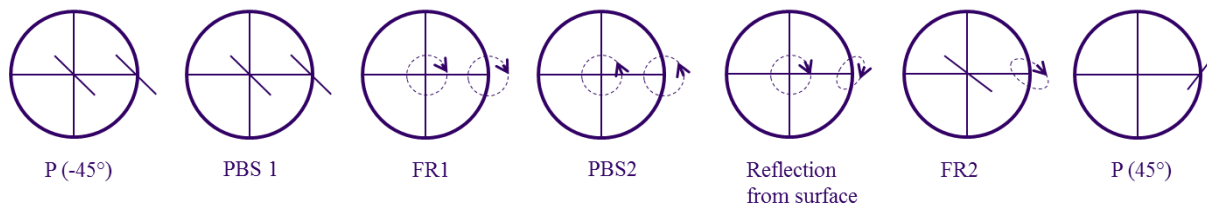


Figure 5.2 polarisation states at different positions for the block case

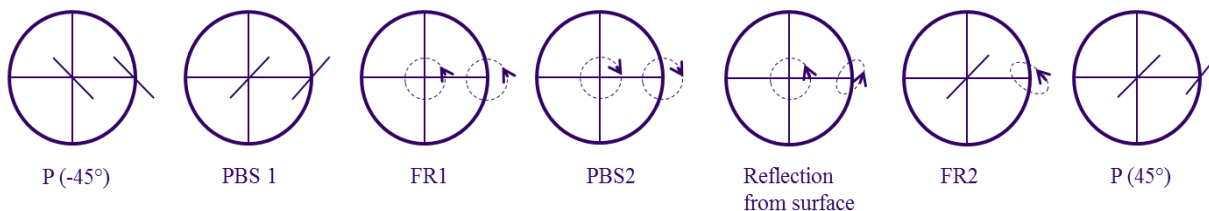


Figure 5.3 polarisation states at different positions for the pass case

The Mirau objective consists of a reflector made of an unknown material and a beam splitter (MBS) as shown in Figure 5.1. For LED1 illumination arm, the polarisation state following reflection from the Mirau reflector will be similar to 5.2. The back focal plane viewed after FR2 and P(45°) with reflection only from Mirau reflector, produces an annular pattern as shown in Figure 5.4(a). A similar pattern is expected, if the light only from the sample is viewed after the FR2 and P(45°) combination. Therefore, for the first illumination arm containing LED1, the object superposed with fringe pattern due to two annular reflected beams coming from Mirau and from the sample is recorded by the CCD. This case is referred to as the “block” configuration from the fact that the central portion of the light is blocked.

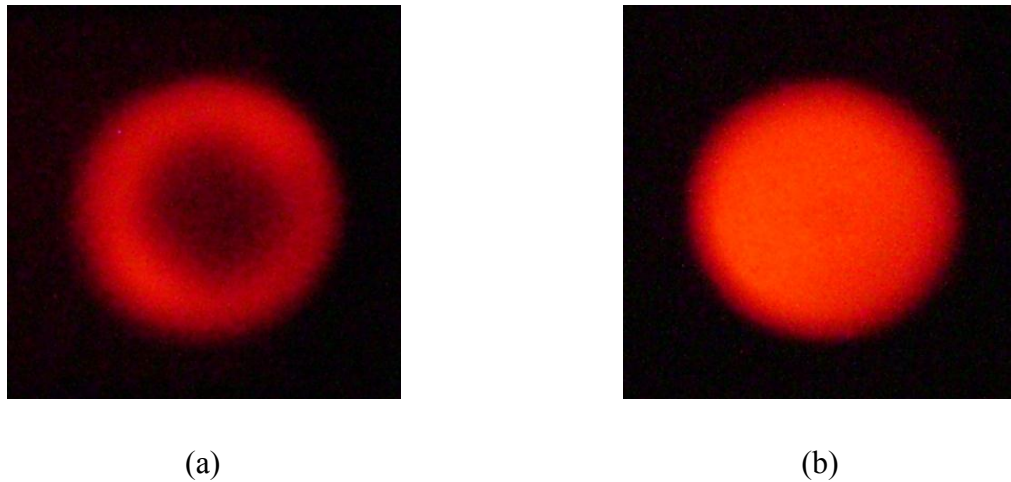


Figure 5.4 (a) Image of the reflected beam after FR2 and P combination for LED1 arm and (b) image of the reflected beam after FR2 and P combination for LED2 arm

For the illumination arm of the set-up containing LED2, the polarisation states at different components are illustrated in Figure 5.3. The light reflected from the sample, in this case, is LCP for normal incidence (central part) and with increase in angle of reflection again the polarisation becomes more and more elliptic as shown in Figure 5.3. Since the FR2 and P combination lets through LCP, the central portion in this case will be transmitted. The intensity of the beam, due to departure from ideal LCP at the edge of the aperture, reduces the intensity slightly as shown in Figure 5.4(b). This case is referred to as the “pass” configuration.

5.2 THEORY OF PS-CSI

In this section the expressions for intensities of the block and the pass cases are deduced from the electric field components according to Fresnel equations. Consider the two LEDs have amplitudes l_1 and l_2 per unit solid angle, respectively. The unit vectors along x and y in the plane perpendicular to light propagation (considered as z direction) are given as \hat{x} and \hat{y} . Here, the polarisation of light at each stage will be described. After the collimating lenses L1 and L2 a plane parallel beam will propagate towards the sample and a plane parallel beam can be described by

$$\vec{E} = \vec{E}_{xy} e^{j(2\pi kz - \omega t)} \quad (5.1)$$

where, \vec{E}_{xy} is the light amplitude, $k = 1/\lambda$ is the wave-number, \vec{r} is position vector, ω is angular frequency of the light and t is the time. The phase term $(2\pi kz - \omega t)$ will be the same for all of the polarisation states and can be dropped, leaving,

$$\vec{E} = \vec{E}_{xy} = E_x \hat{x} + E_y \hat{y}. \quad (5.2)$$

where, x & y directions are considered to coincide with p & s directions, respectively.

5.2.1 ANALYSIS OF THE BLOCK CASE

In the block case the field after the light passes through P1 (-45°) is given by

$$\begin{aligned} \vec{E}_{b1} &= (l_1). (-\cos 45 \hat{x} + \sin 45 \hat{y}) \\ \text{or, } \vec{E}_{b1} &= (l_1/\sqrt{2}). (-\hat{x} + \hat{y}). \end{aligned} \quad (5.3)$$

The transmission coefficient and reflection coefficient of the identical pellicle beam-splitters BS1 and BS2 are given by t and r over the operating wavelength range ($615 \text{ nm} - 655 \text{ nm}$). After transmission through BS1 no change of polarisation state occurs and the field \vec{E}_{b2} is given by,

$$\vec{E}_{b2} = (l_1 t/\sqrt{2}). (-\hat{x} + \hat{y}). \quad (5.4)$$

After FR1 where linear polarised light becomes RCP, the field \vec{E}_{b3} is given by,

$$\vec{E}_{b3} = (l_1 t/\sqrt{2}). \left(-\hat{x} \cdot \exp\left(\frac{j\pi}{2}\right) + \hat{y}\right), \quad (5.5)$$

After reflection from BS2 the direction of propagation changes and a relative phase change of π is added to the orthogonal components that changes the polarisation to LCP, which is given by \vec{E}_{b4} ,

$$\begin{aligned}\vec{E}_{b4} &= (l_1 t / \sqrt{2}) \cdot (-\hat{x} \cdot j \cdot (+r) + \hat{y} \cdot (-r)), \\ \vec{E}_{b4} &= (l_1 t r / \sqrt{2}) \cdot (-\hat{x} \cdot j - \hat{y}).\end{aligned}\quad (5.6)$$

The negative sign for the y – component is due to the fact that in reflection light returns to the same medium and accordingly, the electric field vector in this case, is expressed by a negative sign [4, 5]. At the back-focal-plane of the Mirau objective the light is LCP after reflection from the object under observation and changes polarisation such that,

$$\begin{aligned}\vec{E}_{b5} &= (l_1 t r / \sqrt{2}) \cdot (-\hat{x} \cdot j \cdot (+\mathbf{r}_p^o) - \hat{y} \cdot (-\mathbf{r}_s^o)), \\ \vec{E}_{b5} &= (l_1 t r / \sqrt{2}) \cdot (-\hat{x} \cdot j \cdot \mathbf{r}_p^o + \hat{y} \cdot \mathbf{r}_s^o)\end{aligned}\quad (5.7)$$

where, \mathbf{r}_p^o and \mathbf{r}_s^o are the Fresnel coefficients for the object which are function of the incidence angle and $\mathbf{r}_p^o = \mathbf{r}_p^o(\theta)$ & $\mathbf{r}_s^o = \mathbf{r}_s^o(\theta)$, θ is incidence angle. After reflection the beams passes through PBS2 with no polarisation change and the field \vec{E}_{b6} is given by,

$$\vec{E}_{b6} = (l_1 t^2 r / \sqrt{2}) \cdot (-\hat{x} \cdot j \cdot \mathbf{r}_p^o + \hat{y} \cdot \mathbf{r}_s^o) \quad (5.8)$$

Passing through FR2 a reflective phase change of $\frac{\pi}{2}$ is added and the field \vec{E}_{b7} is given by,

$$\begin{aligned}\vec{E}_{b7} &= (l_1 t^2 r / \sqrt{2}) \cdot \left(-\hat{x} \cdot j \cdot \mathbf{r}_p^o \cdot \exp\left(\frac{j\pi}{2}\right) + \hat{y} \cdot \mathbf{r}_s^o\right) \\ \vec{E}_{b7} &= (l_1 t^2 r / \sqrt{2}) \cdot (\hat{x} \cdot \mathbf{r}_p^o + \hat{y} \cdot \mathbf{r}_s^o)\end{aligned}\quad (5.9)$$

Now, the analyser (P) after FR2 is oriented 45° to block the light coming from normal incidence. Assuming a unit vector \vec{u} along 45°

$$\vec{u} = (\cos 45 \hat{x} + \sin 45 \hat{y}) = (1/\sqrt{2}) \cdot (\hat{x} + \hat{y}) \quad (5.10)$$

The electric field component at the CCD plane will therefore, be given by,

$$\mathbf{E}_b^o = \vec{E}_{b7} \cdot \vec{u} = \left(\frac{l_1 t^2 r}{2}\right) \cdot (\mathbf{r}_p^o(\theta) + \mathbf{r}_s^o(\theta))$$

$$\mathbf{E}_b^o = b.(\mathbf{r}_p^o(\theta) + \mathbf{r}_s^o(\theta)) \quad (5.11)$$

where, $b = (l_1 t^2 r / 2)$ and \mathbf{E}_b^o is the final electric field component that returns from the object at the image plane for object in the block case. Here, the dependence of the reflection coefficients on the incidence angle is written explicitly. Simultaneously, the component reflected from the Mirau reflector is,

$$\mathbf{E}_b^m = b.(\mathbf{r}_p^m(\theta) + \mathbf{r}_s^m(\theta)) \quad (5.12)$$

where, \mathbf{E}_b^m is the final electric field component for the Mirau reflector. It can be seen that for normal incidence, where $\mathbf{r}_p(0^\circ) = -\mathbf{r}_s(0^\circ)$, the component \mathbf{E}_b^o for the block case becomes null. With increase in incidence angle, for components propagating further away from the centre of the objective aperture the field will become more and more elliptic and light will start to pass through the FR2 and P combination, as shown in Figure 5.4(a).

Each object point corresponds to an image point (pixel) on the CCD and all possible rays within the maximum aperture angle θ_{max} contribute to this image point. This is illustrated in Figure 5.5(a) with a conventional microscope for simplicity.

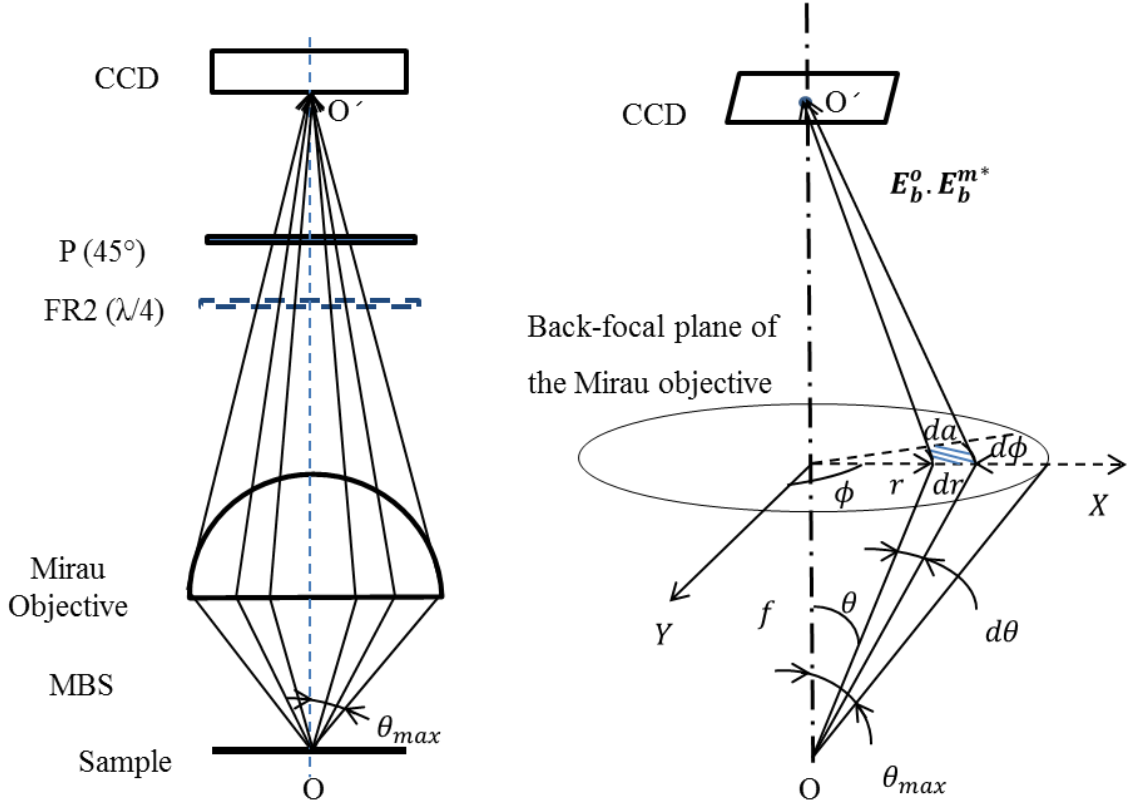


Figure 5.5 (a) Interferogram recording in PS-CSI; (b) Resultant polarisation due to elemental area da

Rays at different incidence angles are shown to form the image O' for an object point O . With change in incidence angles, the polarisations of the rays are changed and for the object point O , the resultant effect due to the rays within the entire aperture is recorded in O' . In reality, each ray is representative of interference occurring between rays coming from sample and Mirau reflector. To compute the resultant effect, therefore, the interference for each ray needs to be integrated over the entire aperture. Consider a set of rays coming from O at radius r , inclination angle θ and azimuth ϕ that form an elemental area da at the back focal plane as shown in Figure 5.5(b). The set of rays from the elemental area da meet at O' as shown in Figure 5.5(b). For this elemental area, the resultant interference at O' is $E_b^o E_b^{m*} da$. Therefore, in analogy to equation 3.34 in Chapter 3, a complex analytic function I_b due to the fringe pattern measured at the CCD for the entire object can be written as,

$$I_b = \iint_{aperture} E_b^o E_b^{m*} da, \quad (5.13)$$

where, $da = dr \cdot r d\phi$ is the elemental aperture area at back-focal-plane and f is the focal length (remains constant). The elemental aperture area in the back-focal-plane can be written as,

$$da = f \tan \theta \sec^2 \theta d\theta d\phi \quad (5.14)$$

Substituting values for the field components and elemental area,

$$\begin{aligned} I_b &= C_b' \iint_{\phi=0}^{2\pi} \iint_{\theta=0}^{\theta_{max}} (\mathbf{r}_p^o + \mathbf{r}_s^o) \cdot (\mathbf{r}_p^m + \mathbf{r}_s^m)^* w(\theta) d\theta d\phi \\ &= C_b' \int_{\theta=0}^{\theta_{max}} (\mathbf{r}_p^o + \mathbf{r}_s^o) \cdot (\mathbf{r}_p^m + \mathbf{r}_s^m)^* w(\theta) d\theta \int_0^{2\pi} d\phi \\ I_b &= C_b' \int_{\theta=0}^{\theta_{max}} (\mathbf{r}_p^o + \mathbf{r}_s^o) \cdot (\mathbf{r}_p^m + \mathbf{r}_s^m)^* w(\theta) d\theta \end{aligned} \quad (5.15)$$

where, including 2π within the constant,

$$C_b' = \pi f \left(\frac{l_1 t^2 r}{\sqrt{2}} \right)^2 \quad (5.16)$$

$$\text{and, } w(\theta) = \tan \theta \sec^2 \theta. \quad (5.17)$$

Equation 5.15 represents the complex analytic function of the block case and it depends on the sum of the reflection coefficients. It is complex due to the presence of the complex reflection coefficients \mathbf{r}_p^o and \mathbf{r}_s^o .

5.2.2 ANALYSIS OF THE PASS CASE

The mathematical formulation for this case is similar to the previous case, only the polarisation states at different positions of the set-up are different. The electric field components for different incidence angle at the image plane are expressed separately for the object and Mirau reflector with quantities are subscripted with “p” to refer to the pass case and they can be written as,

$$\mathbf{E}_p^o = p \cdot (\mathbf{r}_p^o - \mathbf{r}_s^o) \quad (5.18)$$

$$\& \quad \mathbf{E}_p^m = p \cdot (\mathbf{r}_p^m - \mathbf{r}_s^m) \quad (5.19)$$

where, $p = \frac{l_2 tr^2}{2\sqrt{2}}$.

Change in the expression of p compared to b is due to the fact that for the pass case a) the illumination is from source LED2 and b) the light is transmitted once and reflected twice from the pellicle beam-splitters (For the block case the light is transmitted twice and reflected once). Again, for another complex analytic function I_p for the pass case for a pixel is given by the integrated effect due to all the incidence angles and therefore, can be written similar to equation 5.13,

$$I_p = \iint_{aperture} \mathbf{E}_p^o \mathbf{E}_p^{m*} da, \quad (5.20)$$

where, da refers to the elemental aperture area (shown in Figure 5.5(b)). Again, the integrand does not depend on φ and substituting all the quantities, the complex analytic function for the pass case can be expressed as,

$$I_p = C_p' \int_{\theta=0}^{\theta=\theta_{max}} (\mathbf{r}_p^o - \mathbf{r}_s^o) \cdot (\mathbf{r}_p^m - \mathbf{r}_s^m)^* w(\theta) d\theta, \quad (5.21)$$

where,

$$C_p' = \pi f \left(\frac{l_2 tr^2}{\sqrt{2}} \right)^2. \quad (5.22)$$

Equation 5.21 is the representative equation of the interference pattern incident on the CCD for the pass case which depends on difference of the reflection coefficients. The pass case is similar to an ordinary CSI with circularly polarised source and in this case, the phase introduced due to polarisation is much less compared to the block case.

5.2.3 EVALUATION OF THE RATIO OF THE COMPLEX ANALYTIC FUNCTIONS DUE TO BLOCK AND PASS CASES

Let us consider the phase and amplitude plots of polarisation components $r_p^o + r_s^o$ and $r_p^o - r_s^o$, (equation 5.11 and 5.18) of the block case and the pass case with respect to the incidence angle. Figure 5.6 to 5.9 show the plots up to the maximum aperture angle for $N_A = 0.7$ ($\theta_{max} = 44^\circ$) for glass, gold, silver and aluminium.

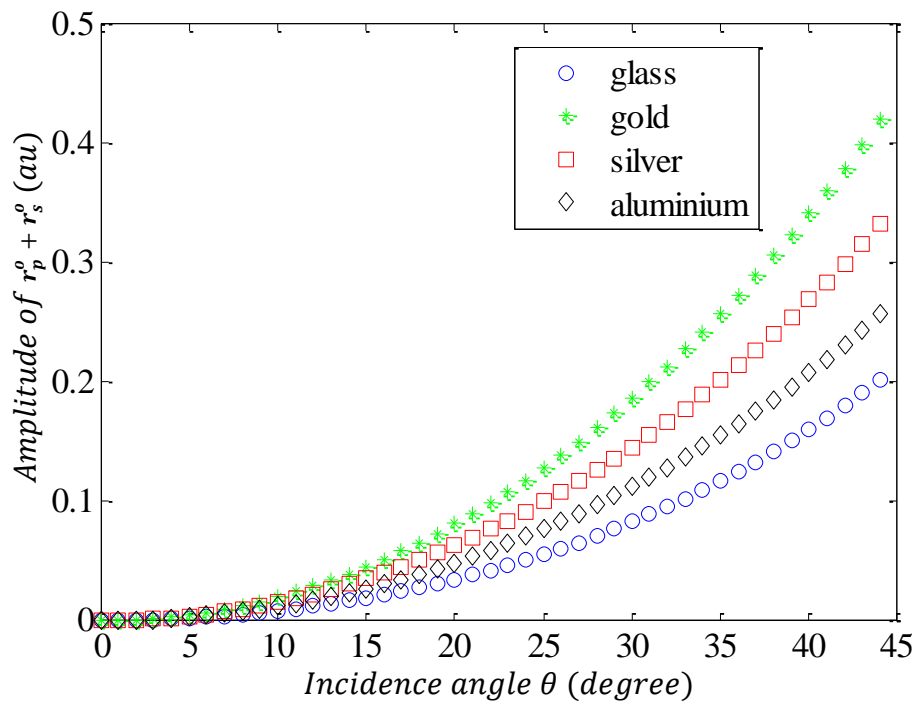


Figure 5.6 Amplitude plot w.r.t incidence angle for $r_p^o + r_s^o$

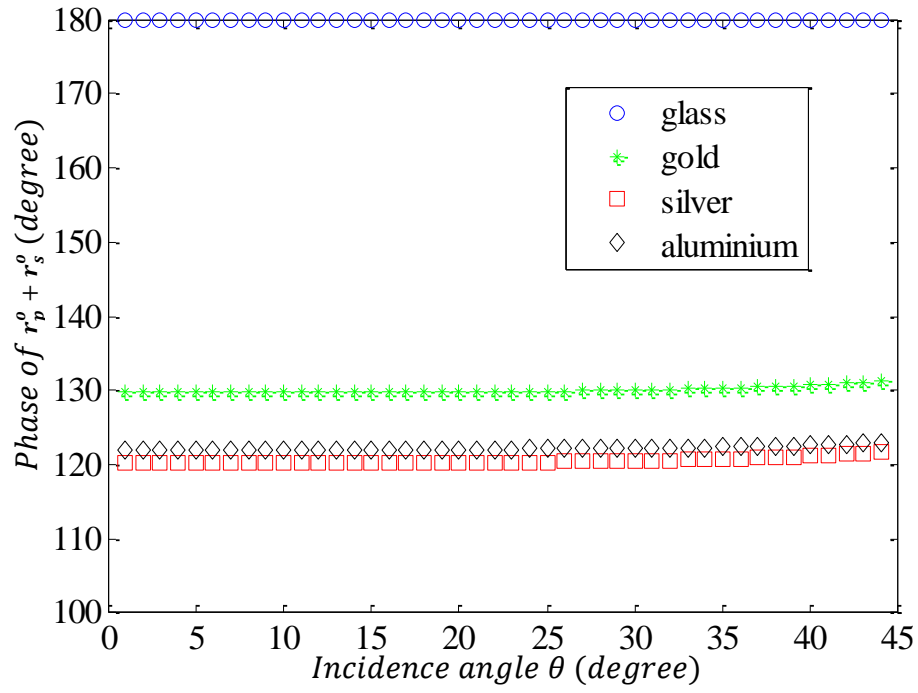


Figure 5.7 Phase plot w.r.t incidence angle for $r_p^o + r_s^o$

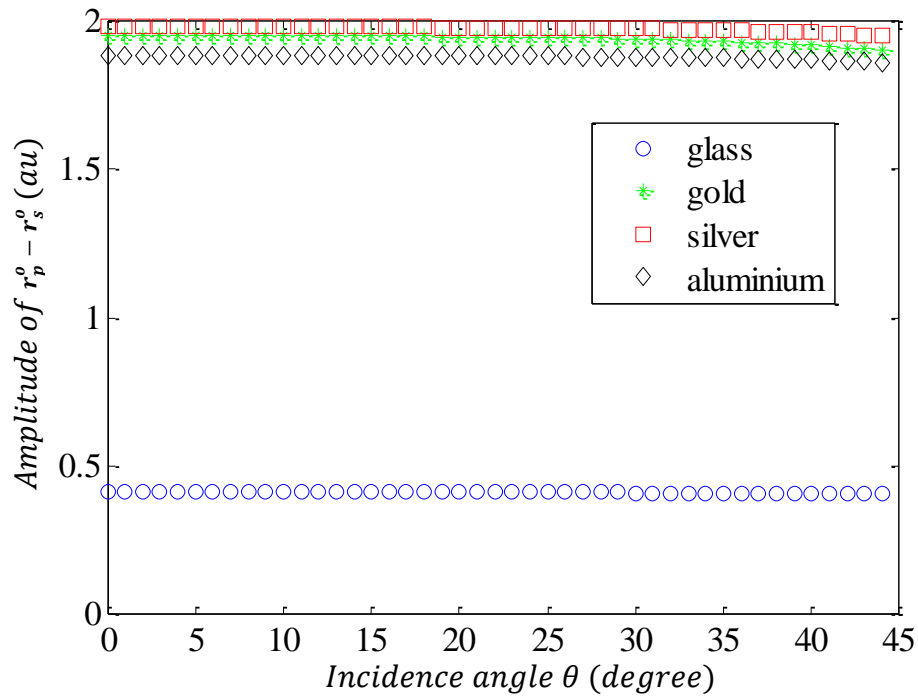


Figure 5.8 Amplitude plot w.r.t incidence angle for $r_p^o - r_s^o$

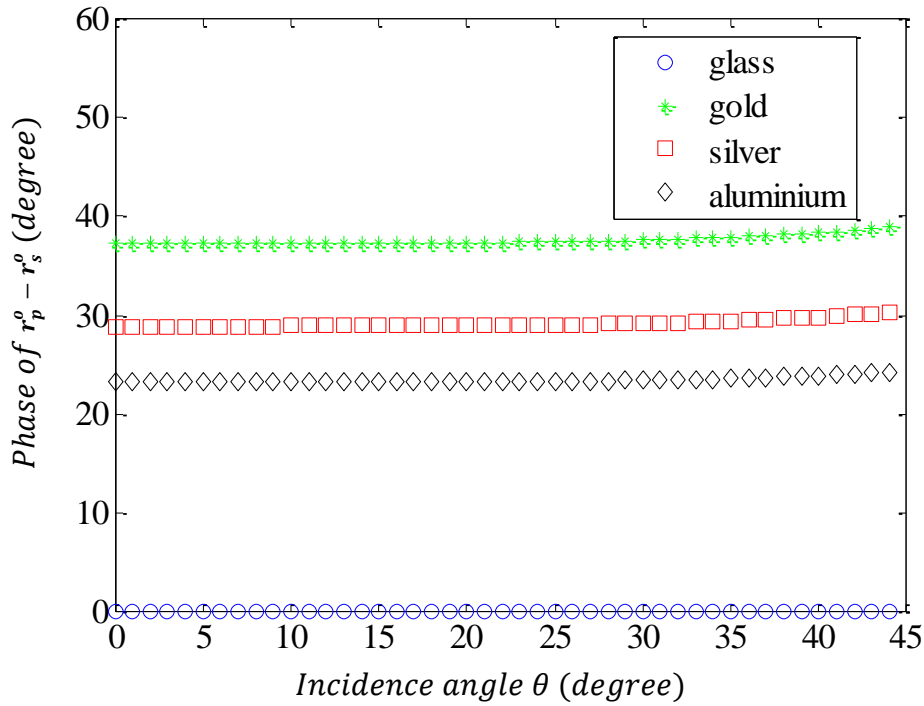


Figure 5.9 Phase plot w.r.t incidence angle for $r_p^o - r_s^o$

It can be seen from Figure 5.7 that the phase of glass (and all dielectric materials) remains constant at 180° throughout the angular range for the block case. For the metals, it varies very slightly (within 2°) and could be assumed to be constant within the angular range for all practical purposes. Similarly, for the pass case the phases of different materials can be assumed to be constant with the variation remaining within 2° (Figure 5.9). The representative phase values for all the materials for both the block and the pass cases are taken to be the values at $\theta_m = 40^\circ$ as described in Table 5.1. The reason for this choice will be explained later in Section 5.2.4. The corresponding change in height is also presented in Table 5.1. The height is calculated using an effective wavelength $\bar{\lambda}$ which is calculated as discussed in section 5.3.2.2 for this set up.

Table 5.1 Phase values over the aperture for the block and the pass cases

Materials	Phase of the block case at $\theta_m = 40^\circ$ ($r_p^o + r_s^o$)		Phase of the pass case at $\theta_m = 40^\circ$ ($r_p^o - r_s^o$)	
	(Degree)	(nm)	(Degree)	(nm)
Gold	130.1°	117.2	37.6°	33.9
Silver	120.5°	108.5	29.2°	26.3
Aluminium	122.2°	110.1	23.4°	21.1
Glass	180°	162.1	0°	0

The amplitude plots of the block case (Figure 5.6) and the pass case (Figure 5.8) reveal that the plots of the materials are of the same nature. The sum and the differences of reflection coefficients $(r_p^o + r_s^o)$ and $(r_p^o - r_s^o)$ for gold, silver and aluminium can be expressed as complex constants multiplied by the sum and the differences of reflection coefficients for glass $(r_p^{glass} + r_s^{glass})$ and $(r_p^{glass} - r_s^{glass})$, respectively, over the aperture. Therefore, the ratio of the sum and the difference of the reflection coefficients for different materials to that of glass are two complex constants that are to a good approximation constant for all incidence angle and they are given by,

$$\mathbf{z}_b^o = \frac{(r_p^o + r_s^o)^{material}}{(r_p^o + r_s^o)^{glass}} \quad (5.23)$$

$$\mathbf{z}_p^o = \frac{(r_p^o - r_s^o)^{material}}{(r_p^o - r_s^o)^{glass}} \quad (5.24)$$

A similar set of constants, \mathbf{z}_b^m and \mathbf{z}_p^m are assumed for the Mirau objective.

$$\mathbf{z}_b^m = \frac{(r_p^m + r_s^m)^{material}}{(r_p^m + r_s^m)^{glass}} \quad (5.25)$$

$$\mathbf{z}_p^m = \frac{(r_p^m - r_s^m)^{material}}{(r_p^m - r_s^m)^{glass}} \quad (5.26)$$

An interesting point to be noted here is that these two complex constants have fixed phase difference that is the same as the average phase difference between the block and the pass cases. Consequently, the integral equations from 5.15 and 5.21 for block and pass cases can be re-written as,

$$\mathbf{I}_b = C_b' \cdot \mathbf{z}_b^o \cdot \mathbf{z}_b^{m*} \int_{\theta=0}^{\theta_{max}} |r_p^{glass}(\theta) + r_s^{glass}(\theta)|^2 w(\theta) d\theta, \quad (5.27)$$

$$\mathbf{I}_p = C_p' \cdot \mathbf{z}_p^o \cdot \mathbf{z}_p^{m*} \int_{\theta=0}^{\theta_{max}} |r_p^{glass}(\theta) - r_s^{glass}(\theta)|^2 w(\theta) d\theta, \quad (5.28)$$

Equation 5.27 and 5.28 are *the forward model* of this experimental set-up. From the interferograms recorded during the experiments these complex analytic functions can be computed. In interferometric techniques, it is always better to measure the amplitude ratio and phase difference rather than absolute amplitude and phase since it would cancel out the

common mode errors. Accordingly, the ratio of the block and pass analytic functions for each pixel obtained from the experiments can be expressed as,

$$\frac{I_b}{I_p} \Big|_{expt} = \frac{C_b'}{C_p'} \cdot \frac{z_b^o}{z_p^o} \cdot \frac{z_b^{m*}}{z_p^{m*}} \cdot \frac{\int_{\theta=0}^{\theta_{max}} |r_p^{glass} + r_s^{glass}|^2 w(\theta) d\theta}{\int_{\theta=0}^{\theta_{max}} |r_p^{glass} - r_s^{glass}|^2 w(\theta) d\theta} = \mathbf{R}_{expt}^{material} \quad (5.29)$$

where, $\mathbf{R}_{expt}^{material}$ is the ratio due to the experiments for different materials mentioned above.

Equation 5.29 can be expressed in terms of four ratios as shown below.

$$\mathbf{R}_{expt}^{material} = R_{expt}^{il} \mathbf{R}_{calc}^{obj} \mathbf{R}_{expt}^{mirau} R_{calc}^{glass} \quad (5.30)$$

where, each of the ratios are given as,

$$R_{expt}^{il} = \frac{C_b'}{C_p'}, \text{ the ratio of illumination constants of the block and the pass (equation}$$

5.16 and 5.22),

$$\mathbf{R}_{calc}^{obj} = \frac{z_b^o}{z_p^o}, \text{ the ratio of the complex constants of the object of the block and the pass,}$$

(equation 5.23 and 5.24)

$$\mathbf{R}_{expt}^{mirau} = \frac{z_b^{m*}}{z_p^{m*}}, \text{ the ratio of the complex constants of the Mirau objective of the block}$$

and the pass (equation 5.25 and 5.26) and

$$R_{calc}^{glass} = \frac{\int_{\theta=0}^{\theta_{max}} |r_p^{glass} + r_s^{glass}|^2 w(\theta) d\theta}{\int_{\theta=0}^{\theta_{max}} |r_p^{glass} - r_s^{glass}|^2 w(\theta) d\theta}, \text{ the ratio of the integral of the glass parameters.}$$

The suffix *calc* suggests quantities to be calculated and *expt* suggests quantities to be obtained experimentally. In equation 5.30, the ratios R_{expt}^{il} and $\mathbf{R}_{expt}^{mirau}$ are unknown since a) the exact illumination level of only the sample cannot be measured due to the presence of the Mirau reflector and Mirau beam splitter and b) there is no data available about the material of the Mirau reflector and the coating layers of the Mirau beam-splitter. Depending on the Mirau reflector and beam-splitter coating material, additional phase and amplitude can be added to the overall phase and amplitude of $\mathbf{R}_{expt}^{material}$. These ratios, thus, needs to be determined experimentally to evaluate $\mathbf{R}_{expt}^{material}$. From experimental measurements by an ellipsometer at *National Physical Laboratory*, UK (Variable angle spectroscopic ellipsometer, J. A. Woollam Co.), the refractive indices of the gold, silver and aluminium

coated samples are known. From that by calculating the Fresnel coefficients, the complex constants from equation 5.23 and 5.24 can be evaluated. From these calculations the following ratio can be calculated.

$$\mathbf{R}_{calc}^{material} = \mathbf{R}_{calc}^{obj} \mathbf{R}_{calc}^{glass} = \frac{z_b^o \int_{\theta=0}^{\theta_{max}} |r_p^{glass} + r_s^{glass}|^2 w(\theta) d\theta}{z_p^o \int_{\theta=0}^{\theta_{max}} |r_p^{glass} - r_s^{glass}|^2 w(\theta) d\theta} \quad (5.31)$$

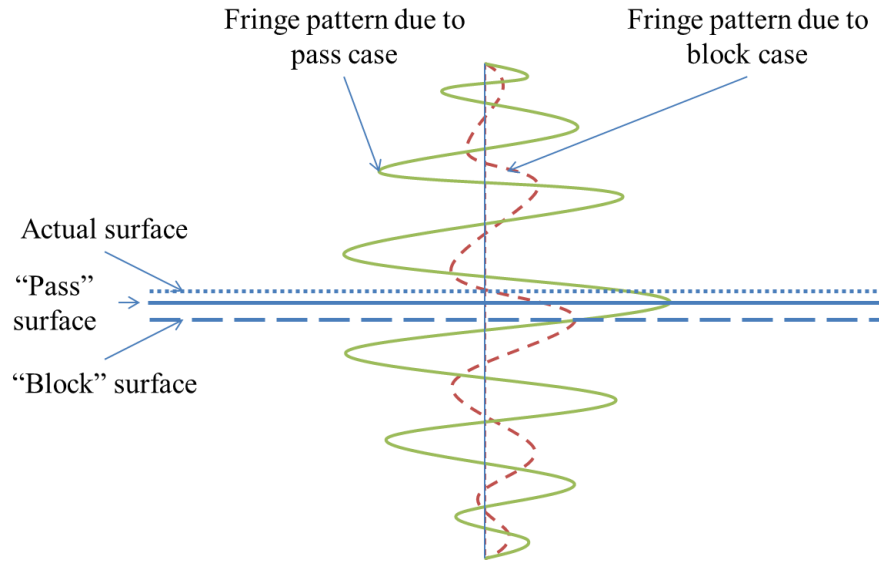
Theoretical values of $\mathbf{R}_{calc}^{material}$ for gold, silver, aluminium and glass are presented in Table 5.2. In this table the magnitude and phase of this ratio are mentioned separately for comparison. The equivalent height for the phase calculated for the equivalent wavelength $\bar{\lambda} = 648.6 \text{ nm}$, obtained from Section 5.3.2.2, is provided once again.

Table 5.2 The theoretical values of the ratio of block and pass analytic functions for different materials

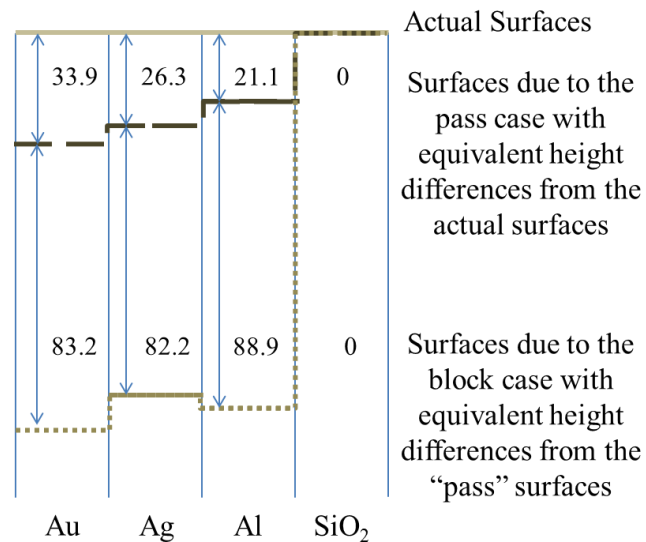
Materials	Refractive indices measured by ellipsometer	$\mathbf{R}_{calc}^{material}$	Amplitude of $\mathbf{R}_{calc}^{material}$ (<i>au</i>)	Phase of $\mathbf{R}_{calc}^{material}$	
				(<i>degrees</i>)	(<i>nm</i>)
Gold	0.13 + 2.96j	-0.0018+0.0429j	0.0429	92.4	83.2
Silver	0.09 + 3.88j	-0.0007+0.0322j	0.0322	91.3	82.2
Aluminium	0.74 + 4.76j	-0.0039+0.0257j	0.0260	98.7	88.9
Glass	1.517	0.0905	0.0905	180	162.1

From Table 5.2, it can be seen that this ratio is greatest for glass. Comparing the metals, gold has the biggest amplitude, then silver and then aluminium. The phases of $\mathbf{R}_{calc}^{material}$ essentially represent the phase differences between the complex constants z_b^o and z_p^o from equation 5.31. In other words, it is the phase difference between the block and the pass case (equation 5.23 and 5.24), if the complex constants for the Mirau objective z_b^m and z_p^m are real values i.e. the Mirau reflector is dielectric. The phases of $\mathbf{R}_{calc}^{material}$ for the metals are close to quarter of a fringe (90°) but for dielectric it is 180° . To illustrate the effect, a diagram in Figure 5.10(a) is presented that shows the actual surface and the positions of the respective surfaces due to the pass and block cases for a single material. For metals, there would be a near quarter wave fringe shift ($\sim 90^\circ$) between these two fringes e.g. for gold this fringe shift is equivalent to a phase shift of 92.44° (from Table 5.2). For dielectric, this is a

half a fringe shift or 180° phase change but if the reflector of the Mirau objective is dielectric, then 180° phase change is introduced again and there won't be any shift. Again, equivalent heights calculated from Table 5.1 and 5.2 for the block and the pass cases can be shown as a deviation from the actual surface. Figure 5.10(b) presents these deviated surfaces for gold, silver, aluminium and glass.



(a)



(b)

Figure 5.10 (a) The position of the actual surface, the pass surface and the block surface with respect to the white light fringe pattern along vertical axis through a pixel; (b) deviation of the surfaces for the pass and the block cases from the actual positions of surfaces for different materials (values are in nanometres)

To determine the ratios R_{expt}^{il} and R_{expt}^{mirau} one has to assume a reference material. Experimentally, I_b and I_p can be obtained from the interferogram of a material and their ratio will provide $R_{expt}^{material}$ but these two unknown ratios will remain within it. In principle, if the sample provides no significant change in fringe pattern or in other words, the phase shift of the fringe pattern then the ratios R_{expt}^{il} and R_{expt}^{mirau} can be computed if $R_{calc}^{material}$ is known. For this case, gold is chosen as the reference material since it is stable and does not oxidise in the atmosphere. Here, the assumption is that the refractive index obtained from the ellipsometer in NPL for gold is correct.

The values of R_{calc}^{gold} is already known and R_{expt}^{gold} can be obtained from experiment, therefore, the product of the unknown ratios can be computed as shown below.

$$R_{expt}^{il} R_{expt}^{mirau} = \frac{C_b}{C_p} \cdot \frac{z_b^{m*}}{z_p^{o*}} \Big|_{PS-CSE} = \frac{R_{expt}^{gold}}{R_{calc}^{gold}} \quad (5.32)$$

Once the unknown ratios are determined from equation 5.32, the ratio of the complex constants $R_{calc}^{obj} = \frac{z_b^o}{z_p^o}$ for the other materials can be determined using equation 5.31 such that,

$$R_{calc}^{obj} = \frac{z_b^o}{z_p^o} = \frac{R_{expt}^{material}}{R_{expt}^{il} R_{expt}^{mirau} R_{calc}^{glass}} \quad (5.33)$$

For a particular material, say, for silver, this is given by,

$$R_{calc}^{silver} = \frac{z_b^{silver}}{z_p^{silver}} = \frac{R_{expt}^{silver}}{R_{expt}^{il} R_{expt}^{mirau} R_{calc}^{glass}} \quad (5.34)$$

Substituting the calculation for the unknown ratios in equation 5.34,

$$\frac{z_b^{silver}}{z_p^{silver}} = \frac{R_{expt}^{silver}}{\left(\frac{R_{expt}^{gold}}{R_{calc}^{gold}} \right) \cdot R_{calc}^{glass}} \quad (5.35)$$

This means the ratio of the complex constants for different materials can be calculated and the corresponding refractive indices can be calculated as shown in Section 5.2.4.

5.2.4 CALCULATION OF THE REFRACTIVE INDICES

To calculate refractive indices for different materials, the ratio of the complex constants $\left(\frac{z_b^o}{z_p^o}\right)$ is reused. If equation 5.35 is written explicitly then,

$$\mathbf{R}_{calc}^{obj} = \frac{z_b^o}{z_p^o} = \frac{(r_p^o + r_s^o)^{material}}{(r_p^o + r_s^o)^{glass}} / \frac{(r_p^o - r_s^o)^{material}}{(r_p^o - r_s^o)^{glass}} \quad (5.36)$$

Manipulating equation 5.36 the following can be derived.

$$\frac{(r_p^o + r_s^o)^{material}}{(r_p^o - r_s^o)^{material}} = \frac{z_b^o}{z_p^o} \cdot \frac{(r_p^o + r_s^o)^{glass}}{(r_p^o - r_s^o)^{glass}} = \mathbf{R}_{calc}^{obj} \cdot R_{gl} \quad (5.37)$$

where, $R_{gl} = \left. \frac{(r_p^o + r_s^o)^{glass}}{(r_p^o - r_s^o)^{glass}} \right|_{\theta_m=40^\circ}$ and From equation 5.37, the ratio of the reflection

coefficients can be written as,

$$\left. \frac{r_p}{r_s} \right|^{material} = \frac{\mathbf{R}_{calc}^{obj} \cdot R_{gl} + 1}{\mathbf{R}_{calc}^{obj} \cdot R_{gl} - 1} = \boldsymbol{\rho}(\theta_m = 40^\circ) \quad (5.38)$$

In this case, $\boldsymbol{\rho}$ is calculated at $\theta_m = 40^\circ$, the angle at which the phases of the block and the pass are evaluated (Table 5.1). In a similar manner to the derivation presented in Chapter 4, the complex refractive index can be calculated using equation 5.39 (from equation 4.6) since the complex refractive index is given by,

$$\mathbf{n} = \left(\mathbf{n}_o^2 \sin^2 \theta_o \left[1 + \left(\frac{1-\boldsymbol{\rho}}{1+\boldsymbol{\rho}} \right)^2 \tan^2 \theta_o \right] \right)^{1/2} \quad (5.39)$$

where, \mathbf{n}_o & θ_o are the refractive index and incidence angle for the medium from which light is incident [6].

To compute the complex refractive index, the incidence angle θ_o should be the same as $\theta_m = 40^\circ$. After computing the refractive indices for each material, $\mathbf{r}_p(\theta_m)$ and $\mathbf{r}_s(\theta_m)$ are calculated (equation 4.1 and 4.3) at $\theta_m = 40^\circ$. The phase due to the pass case can be computed from the sum of the two i.e. $(\mathbf{r}_p(\theta_m) + \mathbf{r}_s(\theta_m))$. From the topography of the pass case, therefore, at each pixel the equivalent height offset of the phase introduced due to the polarisation needs to be taken off. This means that from the “pass” surface in Figure 5.10(a)

the height compensation will generate the actual surface. The phase offset and the corresponding height offset calculated using the effective wavelength of LED $\bar{\lambda}$ (Section 5.3.2.2) that needs to be taken off is given by,

$$\left. \begin{aligned} \Delta\phi_c &= \arg\left(\mathbf{r}_p(\theta_m) + \mathbf{r}_s(\theta_m)\right) \\ \Delta h_c &= \frac{\bar{\lambda}}{4\pi} \Delta\phi_c \end{aligned} \right\} \quad (5.40)$$

5.3 EXPERIMENTAL RESULTS

In this section only smooth surfaces are considered and coated samples are used. To create a composite object with two different materials, glass slides were coated with two different metals. For our purpose samples of a) gold – silver and b) gold – aluminium are investigated. A cleaned glass slide is also measured separately to compare the results of metals with dielectric.

Before going to the details of the experiment a step by step guide is provided below to understand the process of experimentation, data processing and obtaining absolute surface topography for a composite material.

- i. Simultaneous data acquisition of both the block and the pass fringe patterns in the same interferogram using PS-CSI set-up is described in Figure 5.1.
- ii. Fringe patterns for the block and the pass case are separated.
- iii. These interferograms of the block and the pass are filtered to remove noise and to obtain complex analytic functions for the block I_b (equation 5.13) and the pass I_p (equation 5.20).
- iv. The effective wavelength is obtained by measuring the length of the central fringe from I_f (analytic function obtained from experimental fringe pattern) and doubling it.
- v. The uncompensated surface height map from the pass analytic function using envelope detection with phase estimation (Section 2.3.3) for each pixel is calculated.
- vi. At each pixel, the phase difference between the pass and the block cases, where the pass is at the peak position of the envelope, is calculated from step v.
- vii. The product of $R_{expt}^{il} \mathbf{R}_{expt}^{mirau}$ (equation 5.32) (gold used as reference material) is calculated.

- viii. The complex data representing $R_{calc}^{material} |_{expt}$ i.e. amplitude and phase of the block to pass ratio at the peak (equation 5.41) using the data obtained from step v – step vii is calculated.
- ix. $R_{calc}^{material} |_c$ i.e. the product of the R_{expt}^{il} and R_{expt}^{mirau} corrected for polarisation variation over the aperture from theory (equation 5.45 and Section 5.3.4) is calculated.
- x. The ratio $\left(\frac{r_p}{r_s}\right)$ for each material from the above data (step viii – step ix) using equation 5.48 is calculated.
- xi. The complex refractive index (equation 5.39) for each material at each point on the object is calculated and refractive indices maps for the samples (gold – silver and gold – aluminium interface, Figure 5.15) are computed.
- xii. The height offset Δh_c in the surface height maps is calculated and compensated to obtain absolute surface topography.

5.3.1 DETAILS OF THE EXPERIMENT

Two samples (gold – silver and gold – aluminium) have coating thicknesses of the order of few micrometres. Therefore, they can be considered to be thick as assumed in the theoretical computations. Considering any one sample, the interface between the two materials are imaged simultaneously. Fringe data were acquired by the CCD with vertical stage moving upwards and each scan length was about $10 \mu m$ (total 800 frames per scan).

5.3.1.1 SYNCHRONOUS SOURCE AND VERTICAL STAGE

LED1 and LED2 were adjusted to glow with the same square wave ($20 V_{p-p}$) with opposite phases (i.e. LED1 was bright when LED2 was dark) with a frequency of $3.125 Hz$ and this was synchronised with the steps of the vertical stage. The frequency of $3.125 Hz$ was chosen because a) it is a direct even multiple of the frame rate of the CCD which is $25 fps$ and b) the relay system used for this purpose could not be adjusted for more than $8 Hz$. With this frequency 4 frames of data are recorded at a particular vertical stage position for each of the LEDs. Therefore, for a complete square wave consisting of a) bright LED1 with dark LED2 for the positive half of the square wave and b) dark LED1 with bright LED2, the vertical stage would be at the same position.

5.3.1.2 SAMPLING RATE AND LED WAVELENGTH

The sampling rate in the vertical direction was another consideration for choosing the LED wavelength to be $0.635 \mu m \pm 0.020 \mu m$. Each step in the vertical direction is $0.1 \mu m$ and therefore, to be on the safe side three points per cycle is needed to reconstruct the wave.

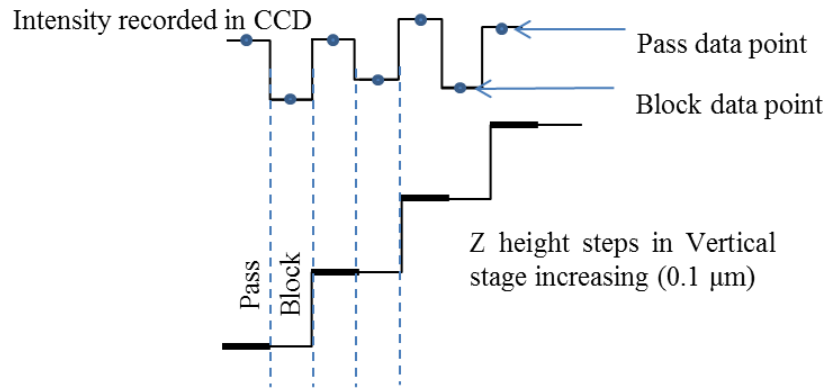
5.3.2 CALCULATION OF SURFACE HEIGHT AND PHASE DUE TO POLARISATION

The steps required to calculate the absolute surface height are described in the following. The signal processing starts after separating out the data recorded by the synchronised source and vertical stage.

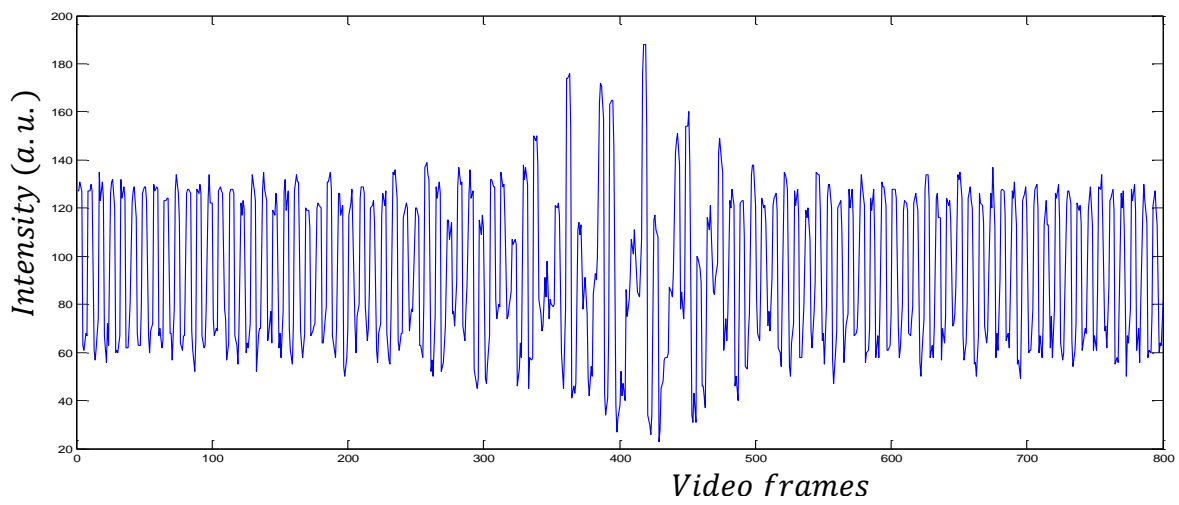
5.3.2.1 SEPARATION OF THE INTERFEROGRAMS OF THE BLOCK AND THE PASS

With the total frames captured considering each eight frames (at a time 8, 16, 24 , etc.): the first four belonged to the pass case and second four to the block case as shown in Figure 5.11(a). In general, the block case has less intensity compared to the pass case. Among the frames captured for each step for the block and the pass the middle frames (2nd and 3rd within 4 frames) are separated to produce separate block and pass data sets. These points are shown as dots in Figure 5.11(a). Figure 5.11(b) shows an actual intensity recorded along a pixel and the block and the pass produce different intensities at each step. Figure 5.11(c) shows the separated data which clearly looks like interference fringe data along Z. The intensity of the block case is less compared to the pass case and the fringes spread out a little more compared to the pass.

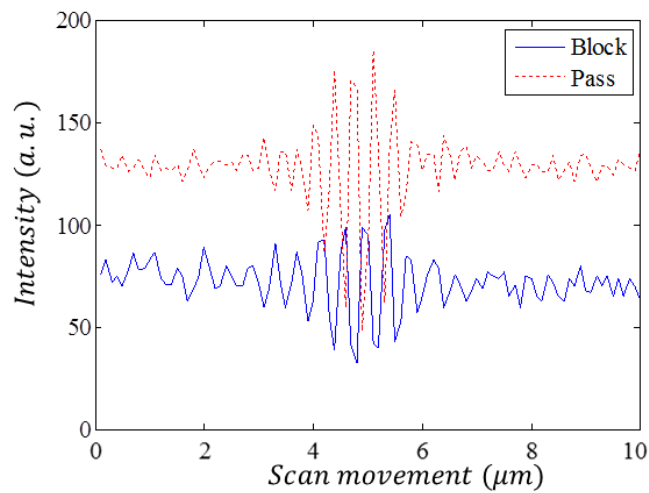
To illustrate this method let us consider the first eight frames first four belong to pass and second four to block. Among these four frames the first and last (i.e. 1st and 4th for pass) are not taken since then the LED or the stage are changing state and 2nd or 3rd frame is taken for pass and 6th or 7th frame is taken for block and this continues for all other steps. Therefore, method of separation of block and pass fringes is asynchronous.



(a)



(b)



(c)

Figure 5.11 (a) Recording of intensity with each vertical step height increase for pass and block, (b) total set of data for a pixel; four consecutive steps for block and the next four for pass and (c) after separating out block and pass data by choosing points from the total set mentioned above; top – pass and bottom – block

5.3.2.2 PROCESSING OF THE INTERFEROGRAMS FOR THE BLOCK AND THE PASS

After the entire data volume is obtained, it is subjected to frequency domain filtering to reduce noise as explained in section 4.2.1, equation 4.17. Figure 5.12 shows the filtered complex analytic function $I_f(x, y, z)$ for both the pass and the block cases. The signal has improved if one compares to Figure 5.11 (c) and the vertical resolution is 3.4 nm for this case.

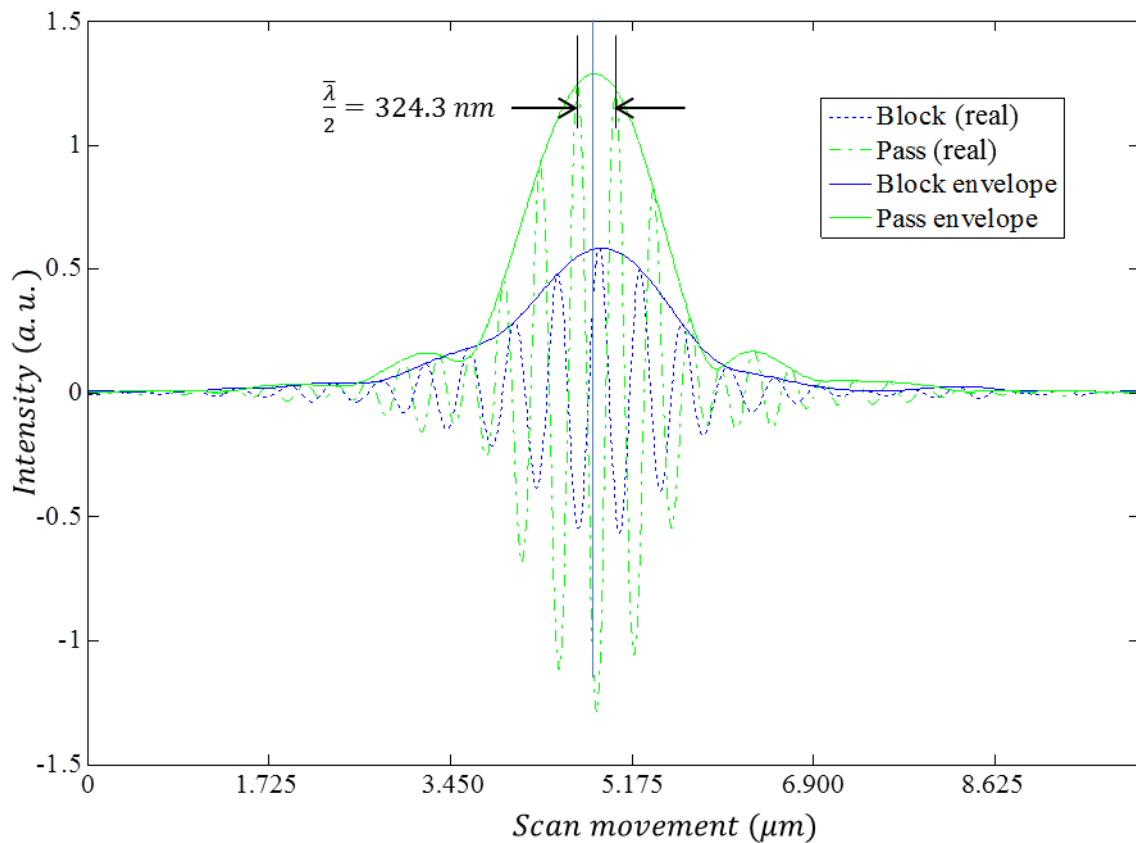


Figure 5.12 Real and absolute value of $I_f(x, y, z)$ for a pixel for both the pass (with higher peak) and the block

From the complex analytic function $I_f(x, y, z)$ of both block and pass data for each pixel, the coherence envelope functions can be computed as shown in Figure 5.12. In a similar manner to that determined in Section 2.3.3 (envelope detection with phase estimation, equation 2.5 and 2.6), the surface height is computed from the pass interferogram $I_{fp}(x, y, z)$, for each pixel (say (x, y)). It has to be noted that this surface height contains the phase due to the polarisation (phase due to $r_p^o - r_s^o$ given in Table 5.1 and Figure 5.10). For the same pixel at the same vertical height, the coherence peak is obtained for the block interferogram

$I_{fb}(x, y, z)$ and the phase difference between the block to the pass is calculated. In general, the envelope peak of the block should in the same position as shown in Figure 5.13 but the phase will be different due to polarisation. For metals this phase difference is close to 90° as shown in Table 5.2.

From Section 2.2, it is known that the effective wavelength can be calculated by doubling the measured length of the central fringe. Therefore, in this case, the effective wavelength $\bar{\lambda}$ is measured to be 648.6 nm as shown in Figure 5.12.

The following data sets are obtained from the pass and block interferograms.

- a) Uncompensated surface height by calculating envelope peak with phase estimation of pass data as explained in Section 2.3.3,
- b) complex data representing $\mathbf{R}_{expt}^{material}$ i.e. amplitude and phase of the block to pass ratio at the peak (equation 5.30) for both materials and
- c) the effective wavelength $\bar{\lambda} = 648.6 \text{ nm}$.

5.3.3 INITIAL RESULTS: METALLIC OBJECTS

First, the ratio $\mathbf{R}_{expt}^{material}$ for gold (\mathbf{R}_{expt}^{gold}) is computed and from Table 5.2 \mathbf{R}_{calc}^{gold} is obtained. The product of the unknown ratios due to illumination and Mirau objectives ($\mathbf{R}_{expt}^{il} \mathbf{R}_{expt}^{mirau}$) can then be calculated from \mathbf{R}_{expt}^{gold} and \mathbf{R}_{calc}^{gold} using equation 5.32. From equation 5.31 and Table 5.2 theoretical values of $\mathbf{R}_{calc}^{material}$ can be obtained. The same ratio, however, can also be obtained from the experimental values of $\mathbf{R}_{expt}^{material}$ and then ratios can be compared for the materials used. Let us call this new ratio as $\mathbf{R}_{calc}^{material} |_{expt}$ given by,

$$\mathbf{R}_{calc}^{material} |_{expt} = \frac{\mathbf{R}_{expt}^{material}}{\mathbf{R}_{expt}^{il} \mathbf{R}_{expt}^{mirau}} \quad (5.41)$$

A representative region of gold from the gold – silver interface, shown in Figure 5.13, is chosen by taking average of 16 pixels near the middle region of coated gold area. The ratio $\mathbf{R}_{expt}^{gold} = 0.46 \exp\left(-j \frac{164\pi}{180}\right)$ is calculated and divided with $\mathbf{R}_{calc}^{gold} = 0.0429 \exp\left(j \frac{92.4\pi}{180}\right)$ from Table 5.2. Therefore, the product of the unknown ratios can be computed as,

$$\mathbf{R}_{expt}^{il} \mathbf{R}_{expt}^{mirau} = 10.72 \exp\left(j \frac{103.6\pi}{180}\right) \quad (5.42)$$

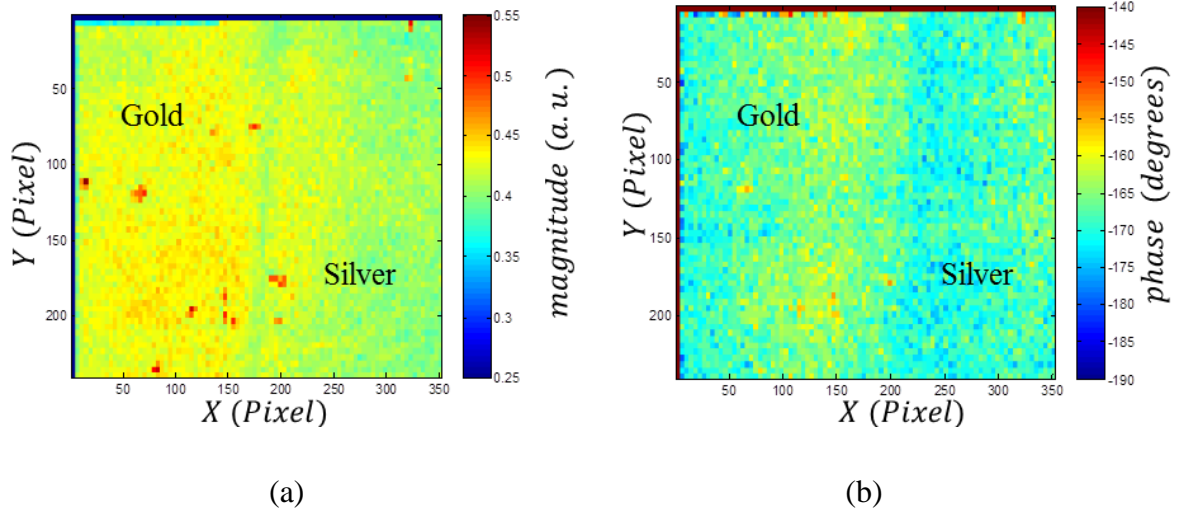


Figure 5.13 Experiment results of the ratio $R_{expt}^{material}$ for gold and silver sample (gold left and silver right) the magnitude (a.u.) and (b) the phase values (degrees)

The results of this calculation are shown Table 5.3. Clearly, for metals and glass the phase angles do not match. In fact for glass (dielectric), the phase should be zero. The amplitude values match their theoretical values better but the discrepancy remains significant. The reason for this is discussed in the following section (Section 5.3.4).

Table 5.3 Results of comparison of experimental and theoretical block to pass ratios (presented in polar form)

Materials	Experiment		Theory
	$R_{expt}^{material}$	$R_{calc}^{material} _{expt}$ $\left(\frac{R_{expt}^{material}}{R_{expt}^{il} R_{expt}^{mirau}} \right)$	$R_{calc}^{material}$ (from Table 5.2)
Silver	$0.41 \exp\left(-j \frac{168\pi}{180}\right)$	$0.0382 \exp\left(j \frac{88.4\pi}{180}\right)$	$0.0322 \exp\left(j \frac{91.3\pi}{180}\right)$
Aluminium	$0.38 \exp\left(-j \frac{173\pi}{180}\right)$	$0.0354 \exp\left(j \frac{83.4\pi}{180}\right)$	$0.0260 \exp\left(j \frac{98.7\pi}{180}\right)$
Glass	0.16	$0.0149 \exp\left(-j \frac{103.6\pi}{180}\right)$	-0.0905

5.3.4 CORRECTIONS FOR THE CHANGE IN POLARISATION AT THE EDGE OF THE APERTURE OF MIRAU OBJECTIVE

According to the theory, the amplitude of the glass ratio (R_{calc}^{glass}) is expected to be more than the amplitude of the ratio of the metals (R_{calc}^{metal}) but the experimental measurements do not show this. This result indicates that the polarisation state of the beam is altered in some way during transmission. To test the polarisation state of the beam coming out of the Mirau objective an experiment was performed as shown in Figure 5.14. The polarisation states of the central beam and the beams observed at the edge are shown in the figure.

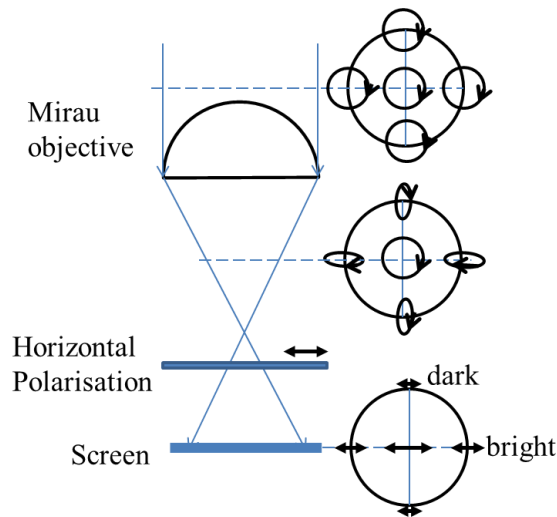


Figure 5.14 Experiment to check the polarisation state of the beam coming out from Mirau

In this experiment, a circularly polarised beam was incident on the Mirau objective and the beam coming out was passed through a linear horizontal polariser. The beam after the polariser was found to be darker towards the edge compared to the central region. As shown in polarisation states just after the Mirau objective, around the edge the horizontal sides are brighter compared to the vertical sides. This can only happen, if during the passage of the beam through the Mirau objective, the circular polarisation is changed. It is postulated that the presence of multiple lenses and the beam-splitter inside the Mirau, changes the polarisation of the rays that are transmitted as a function of incident angles. The effect is predominant at the edge of the aperture since the Fresnel transmission coefficients for glass and coating materials reduce with increase in incidence angle and towards the edge the beam

linear polarisation increased. Therefore, a correction factor needs to be introduced for obtaining the right $\mathbf{R}_{calc}^{material}$, now termed as $\mathbf{R}_{calc}^{material}|_c$.

Consider equation 5.29 – 5.31 ($\mathbf{R}_{expt}^{material}$ and $\mathbf{R}_{calc}^{material}$) where the polarisation change is not considered during light transmission through the Mirau objective. Fresnel transmission coefficients (t_p, t_s) for glass need to be incorporated to these equations to include this effect. Let us consider that a number a signifies number of lens elements within the Mirau and each of the rays is assumed to traverse twice through the Mirau, once during illumination and second after reflection. Therefore, the final electric components for both the block and pass cases considering the transmission coefficients of the glass can be written as,

$$\left. \begin{aligned} \mathbf{E}_b^o|_c &= b. (\mathbf{r}_p^o(\theta). t_p^{4a} + \mathbf{r}_s^o(\theta). t_s^{4a}) \\ \mathbf{E}_p^o|_c &= p. (\mathbf{r}_p^o(\theta). t_p^{4a} - \mathbf{r}_s^o(\theta). t_s^{4a}) \end{aligned} \right\} \quad (5.43)$$

Subsequently, following the same procedure as before (equation 5.13 -5.30) the ratio of the block and pass analytic functions $\mathbf{R}_{expt}^{material}$ and the corrected $\mathbf{R}_{calc}^{material}$ newly termed as, $\mathbf{R}_{calc}^{material}|_c$ could be written as,

$$\mathbf{R}_{expt}^{material} = \frac{C_b.z_b^o.z_b^{m*} \int_{\theta=0}^{\theta_{max}} |r_p^{glass}.t_p^{4a} + r_s^{glass}.t_s^{4a}|^2 w(\theta)d\theta}{C_p.z_p^o.z_p^{m*} \int_{\theta=0}^{\theta_{max}} |r_p^{glass}.t_p^{4a} - r_s^{glass}.t_s^{4a}|^2 w(\theta)d\theta} \text{ and} \quad (5.44)$$

$$\mathbf{R}_{calc}^{material}|_c = \frac{z_b^o \int_{\theta=0}^{\theta_{max}} |r_p^{glass}.t_p^{4a} + r_s^{glass}.t_s^{4a}|^2 w(\theta)d\theta}{z_p^o \int_{\theta=0}^{\theta_{max}} |r_p^{glass}.t_p^{4a} - r_s^{glass}.t_s^{4a}|^2 w(\theta)d\theta} \quad (5.45)$$

It should be noted here, the experimental values of $\mathbf{R}_{expt}^{material}$ obtained from the block and the pass interferogram remain unchanged.

Equation 5.30 and 5.31 for $\mathbf{R}_{expt}^{material}$ are now substituted by equation 5.44 and 5.45. Again, first the block to pass ratio $\mathbf{R}_{calc}^{material}$ with correction factor $\mathbf{R}_{calc}^{material}|_c$ is calculated using equation 5.44 assuming $a = 4$, which means that there are four lens elements within the Mirau objective. This assumption is based on the phase measurement obtained from the experimental ratio $\mathbf{R}_{expt}^{material}$ (Table 5.3 and Table 5.4). Using equation 5.41, it is compared to the same ratio $\mathbf{R}_{calc}^{material}|_{expt}$ calculated from $\mathbf{R}_{expt}^{material}$ (computed from the interferogram). For gold the theoretical ratio is calculated to be $\mathbf{R}_{calc}^{gold}|_c = 0.0085 \exp\left(-j\frac{149\pi}{180}\right)$ and the

experimental ratio $R_{expt}^{gold} = 0.46 \exp\left(-j\frac{164\pi}{180}\right)$ obtained from averaging 16 pixels of the gold surface. Therefore, the product of the unknown ratios $R_{expt}^{il} R_{expt}^{mirau}$ is calculated to be

$$R_{expt}^{il} R_{expt}^{mirau} = 54 \exp\left(-j\frac{15\pi}{180}\right) \quad (5.46)$$

From these values the block to pass ratios for silver, aluminium and glass with the correction factors are compared again in the Table 5.4 similar to Table 5.3.

Table 5.4: Results of comparison of experimental and theoretical block to pass ratios after corrections

Materials	Experiments		Theory
	$R_{expt}^{material}$ (same as Table 5.3)	$R_{calc}^{material} _{expt}$ $\left(\frac{R_{expt}^{material}}{R_{expt}^{il} R_{expt}^{mirau}}\right)$	$R_{calc}^{material} _c$
Silver	$0.41 \exp\left(-j\frac{168\pi}{180}\right)$	$0.0076 \exp\left(-j\frac{153\pi}{180}\right)$	$0.0085 \exp\left(-j\frac{154\pi}{180}\right)$
Aluminium	$0.38 \exp\left(-j\frac{173\pi}{180}\right)$	$0.0071 \exp\left(-j\frac{158\pi}{180}\right)$	$0.0077 \exp\left(-j\frac{157\pi}{180}\right)$
Glass	0.16	0.0030	0.0033

From Table 5.4 it is seen that the phase and the amplitude values match quite well for all the materials. Differences between the experimental and theoretical values are within 0.6% for the phase are and within 10% for the amplitude. Importantly, this model and the assumption of $a = 4$ (i.e. four lens elements) explains why the ratio for the glass is much smaller than previously expected.

5.3.5 CORRECTED REFRACTIVE INDEX CALCULATION AND SURFACE HEIGHT COMPENSATION

Since the results of the experimental and theoretical ratios now show good agreement, the refractive indices and subsequently, the compensated phases can be computed. To

calculate the refractive indices first the complex constants for all the materials, needs to be determined again. The complex constants can be written as,

$$\frac{z_b^o}{z_p^o} = \frac{(r_p^o \cdot t_p^{4a} + r_s^o \cdot t_s^{4a})^{material}}{(r_p^o \cdot t_p^{4a} - r_s^o \cdot t_s^{4a})^{material}} / \frac{(r_p^o \cdot t_p^{4a} + r_s^o \cdot t_s^{4a})^{glass}}{(r_p^o \cdot t_p^{4a} - r_s^o \cdot t_s^{4a})^{glass}} \quad (5.47)$$

From equation 5.47 and substituting $\frac{z_b^o}{z_p^o} = R_{calc}^{obj}$ from equation 5.30,

$$\left(\frac{r_p}{r_s}\right)^{material} = \left(\frac{R_{calc}^{obj} \cdot R_{gl}^a}{R_{calc}^{obj} \cdot R_{gl}^{a-1}}\right) \cdot \left(\frac{t_p^{glass^{4a}}}{t_s^{glass^{4a}}}\right) = \rho|_{\theta_m=40^\circ} \quad (5.48)$$

$$\text{where, } R_{gl}^a = \left. \frac{(r_p^o \cdot t_p^{4a} + r_s^o \cdot t_s^{4a})^{glass}}{(r_p^o \cdot t_p^{4a} - r_s^o \cdot t_s^{4a})^{glass}} \right|_{\theta_m=40^\circ}$$

Equation 5.48 can be compared to the equivalent equation of 5.38. In equation correction factor due to the transmission within Mirau objective is introduced. For each pixel after calculating ρ evaluated at $\theta_m = 40^\circ$ from equation 5.48, equation 5.39 is used to calculate refractive indices (\mathbf{n}) for different materials. From the refractive index values for each pixel the exact phase for normal incidence can be calculated and that phase is compensated for each pixel (equation 5.40). In the Table 5.5, the refractive indices and the height compensation details are given (averaged over 100 pixels). The comparison is between the results obtained from ellipsometry and PS-CSI experiment and the variance of real (σ_r^2) and imaginary parts (σ_i^2) are also given.

Table 5.5 Comparison of Refractive index

Material	Refractive index measured by ellipsometry	Average refractive index measured from PS-CSI experiment
Gold	0.13 + 2.96j	0.31+2.89j ($\sigma_r^2 = 0.13, \sigma_i^2 = 0.58$)
Silver	0.09 + 3.88j	0.88+3.88j ($\sigma_r^2 = 0.20, \sigma_i^2 = 1.14$)
Aluminium	0.74 + 4.76j	1.55+4.78j ($\sigma_r^2 = 0.78, \sigma_i^2 = 4.35$)

From Table 5.5, it can be seen that the imaginary parts of the refractive indices are very closely matched and the maximum error in imaginary part, seen for gold, is of the order of 0.02 %. For real parts, the errors are significantly high with maximum error seen for silver where the real part obtained from the experiment is approximately 10 times higher. This phenomenon is again similar to microellipsometry shown in Table 4.1 where the measurements by microellipsometry show more closely matched imaginary parts compared to the real parts. As noted in Section 4.2.2, however, it is the imaginary values that are critical to the phase offset measurements and height offset measurements.

Figure 5.15(a) and 5.15(b) show the real and the imaginary parts of the refractive indices map, respectively, for the gold – silver sample. Similarly, Figure 5.15(c) and Figure 5.15(d) show the real and the imaginary parts of the refractive indices map, respectively, for the gold – aluminium sample. In both the real and imaginary maps the samples are separated clearly.

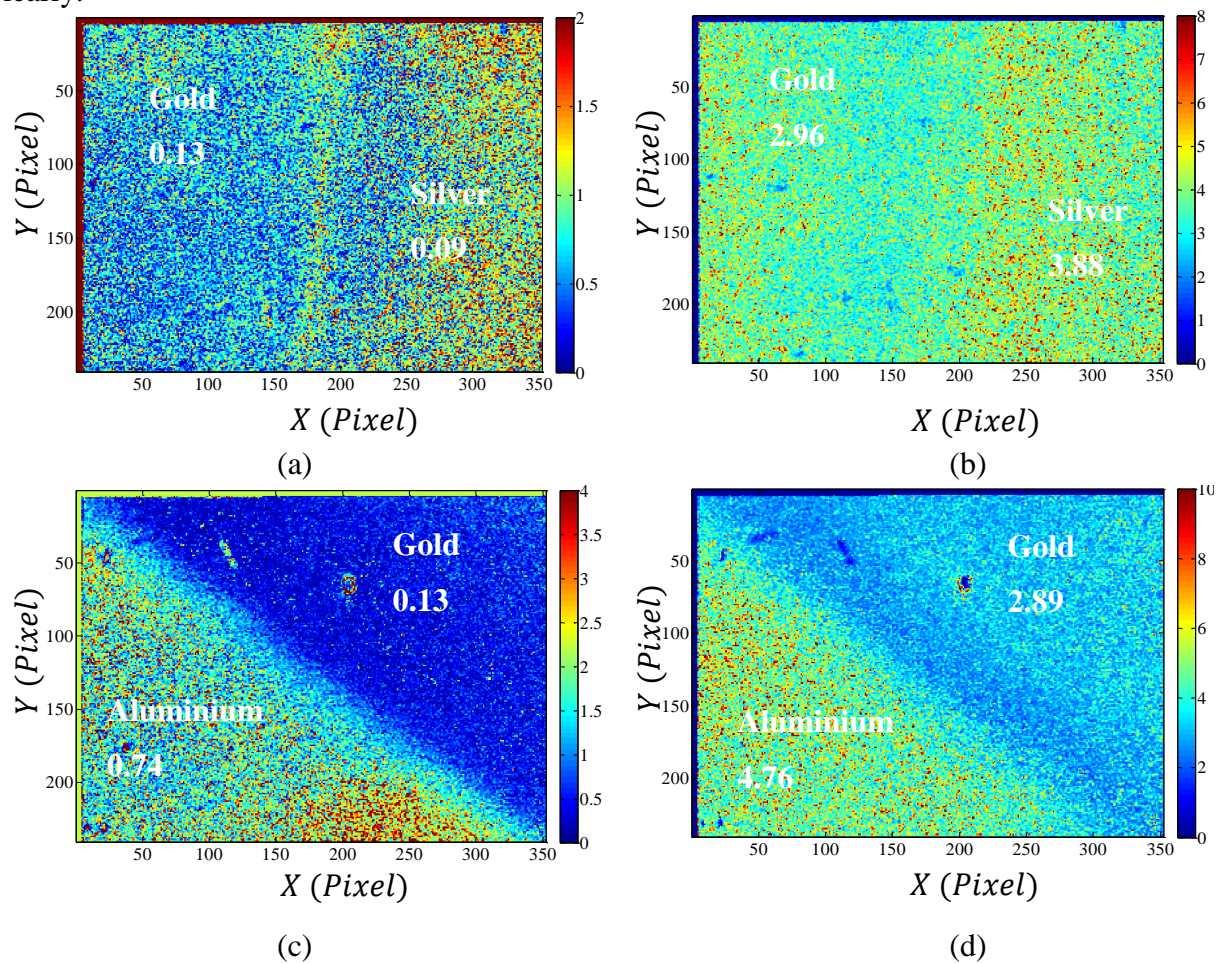


Figure 5.15 (a) Real part of the refractive indices and (b) imaginary part of refractive indices of gold – silver sample (gold on the left);(c) Real part of the refractive indices and (d) imaginary part of refractive indices of gold – aluminium (gold right) sample (theoretical values measured by ellipsometry from Table are 5.5 shown)

As far as the amplitude part is concerned, the non-uniformity of the LED light over the entire aperture and the change introduced in the reference beam caused by the unknown reflectivity of the Mirau reflector and beam-splitter can generate amplitude noise. This can be seen in Figure 5.15. The real part is susceptible more to the amplitude noise since for metals, it is significantly less than the imaginary part. This is similar to the discussion of the results from microellipsometry in Section 4.2.2 where it is shown that the deviation in the real part of the refractive index does not affect the phase appreciably.

Finally, as discussed in Section 5.2.4 (equation 5.40) the surface height offset needs to be compensated to obtain true surface topography. The surface height maps are calculated with respect to the computation of peak of the envelope obtained from the intensity of the pass case (I_p). After the corrections are made, the new phase offset and corresponding height offsets considering $\bar{\lambda} = 648.6 \text{ nm}$ (Section 5.3.2.2) for the pass case can be written as,

$$\left. \begin{aligned} \Delta\phi_c &= \arg(\mathbf{r}_p^o(\theta_m) \cdot t_p^{Aa} - \mathbf{r}_s^o(\theta_m) \cdot t_s^{Aa}) \\ \Delta h_c &= \frac{\bar{\lambda}}{4\pi} \Delta\phi_c \end{aligned} \right\} \quad (5.49)$$

A comparison is presented in Table 5.6 where height offset before correction (equation 5.40, Table 5.1), height offset due to normal incidence and height offset after correction factors incorporated (equation 5.49) are shown.

Table 5.6 Total height compensation for different materials

Material	Height compensation due to offset obtained from the pass case without correction (equation 5.40, Table 5.1) (nm)	Height offset obtained from PS-CSI with corrections Δh_c (equation 5.49) (nm)
Gold	33.9	37.3
Silver	26.3	27.2
Aluminium	21.1	21.2

Therefore, for each pixel after calculating the complex refractive indices, equation 5.49 is evaluated at $\theta_m = 40^\circ$. The offset Δh_c introduced due to the pass intensity is

calculated for each material and that is taken off from the height obtained from each pixel. Figure 5.16(a) and 5.16(b) show uncompensated and compensated surface height maps, respectively. By uncompensated height map, it is meant that the surface height is computed by the envelope detection with phase estimation method on the pass intensity. Looking at the two different surfaces on average about 200 nm surface height difference can be seen (gold is higher). Figure 5.16(c) shows only the compensated height for the entire surface.

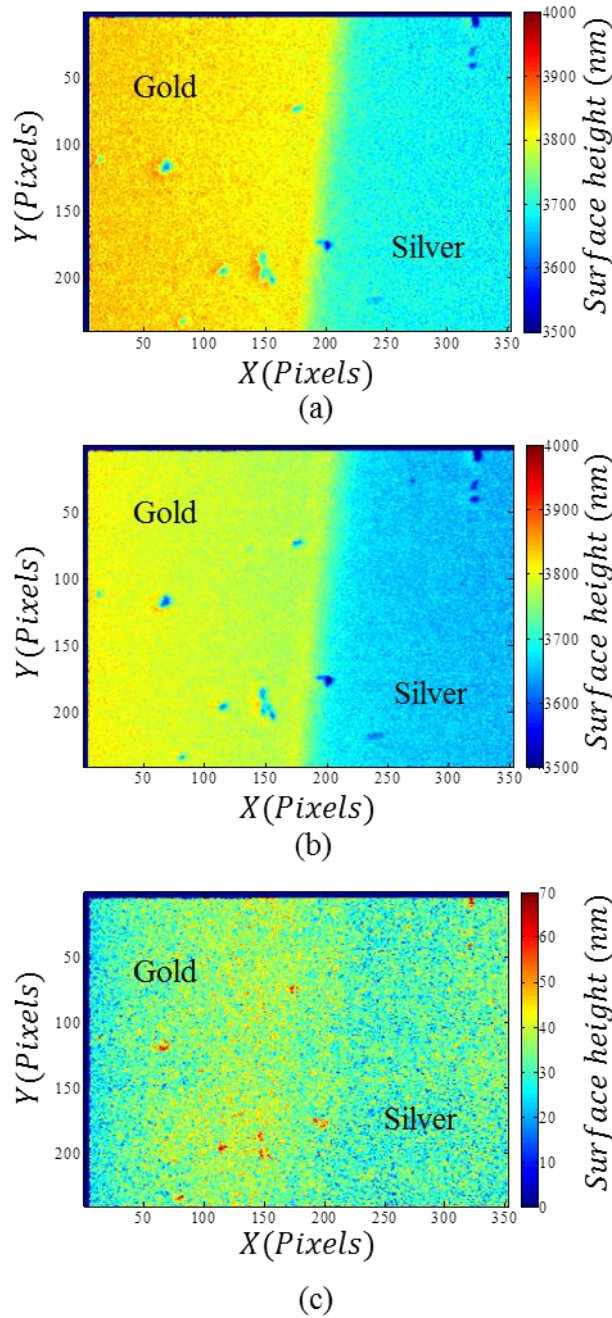


Figure 5.16 For gold-silver sample, (a) uncompensated height map, (b) compensated height map and (c) only height offset from the difference of the uncompensated and compensated height maps

The values are compared to the height offset Δh_c . The height difference between the compensated and uncompensated one clearly shows that for gold there compensation is more compared to silver as shown in Table 5.6. This is consistent with the experiment since gold was coated on the silver surface. Similarly for gold – aluminium surface clearly it can be seen that there is a diagonal variation of height as shown in Figure 5.17(a) and 5.17(b). The height offset obtained from equation 5.49 and compensated for to obtain true surface topography is shown in 5.17(c).

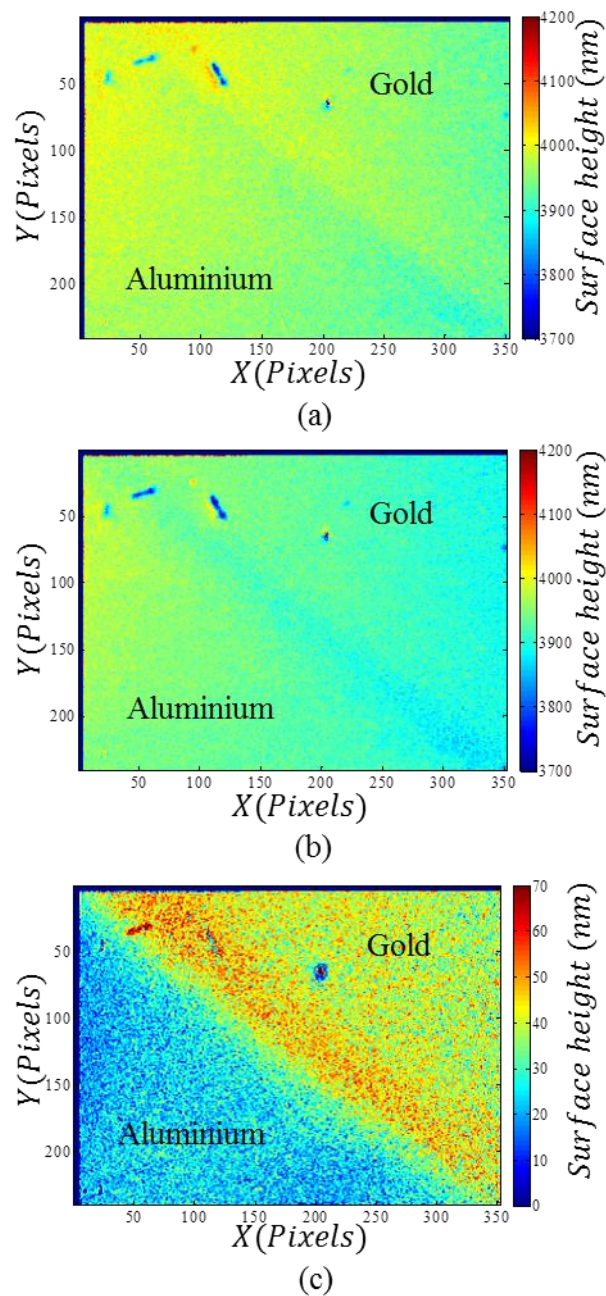


Figure 5.17 For gold-aluminium sample, (a) uncompensated height map, (b) compensated height map and (c) only height offset from the difference of the uncompensated and compensated height maps

It seems that the surface has a tilt along the primary diagonal of the frame. The gold surface is about 100 *nm* higher compared to aluminium. This is consistent with the experiment since the gold was coated over the aluminium surface.

CONCLUSION

In this chapter a novel optical profilometer is proposed and developed which can identify the different materials contained within a single object. Circular polarised incident light within crossed circular polarisers is used to obtain the phase information of two composite objects. The surface height ambiguity due to the different phases introduced by the presence of different materials is calculated, compensated and an absolute surface topography is obtained. The results show good agreement between the theory and experiment and the method can be applied to solve different industrial and research problems.

REFERENCE

1. R. Oldenbourg, "A new view on polarization microscopy", *Nature Communication*, 381 (1996), 811-812.
2. R. Oldenbourg, "Polarized light field microscopy: an analytical method using a microlens array to simultaneously capture both conosopic and orthoscopic views of birefringent objects", *Journal of Microscopy*, 231, 3 (2008), 419-432.
3. S. Inoué and W. L. Hyde, "Studies on depolarization of light at microscope lens surfaces", *Journal of Biophysical and Biochemical Cytology*, 3, 6 (1957), 831-838.
4. E. Hecht, *Optics*, (Pearson Education, 2008).
5. M. Born and E. Wolf, *Principles of Optics*, (Cambridge University Press, 1999).
6. H. Fujiwara, *Spectroscopic Ellipsometry: Principles and applications*, (John Wiley & Sons. Ltd, 2007)

CHAPTER 6: CONCLUSIONS AND FUTURE WORK

INTRODUCTION

In this thesis a novel method based on CSI with polarisation sensitivity was introduced and demonstrated as a means to determine the refractive index and compensate for the height offset introduced by multiple materials within a single object. In this configuration, orthogonal circularly polarised light states are sequentially incident on a composite object through an interferometric objective. An analyser in the observation path is used to block one of these states upon (normal) reflection. An interferogram is recorded as the object is swept through focus. With a change in polarisation, the phase difference between the interferograms is used to calculate the local refractive index and an estimate of the height offset can be measured and subsequently compensated. The technique is rotationally symmetric and termed polarisation sensitive CSI (PS-CSI).

6.1 DISCUSSION OF KEY FINDINGS

This thesis can be separated into two parts. The first part (Chapter 1 – 3) of the thesis discusses the configuration and theory of CSI instrumentation, while the second part (Chapter 4 and 5) discusses the problem of measuring complex refractive index and obtaining absolute surface topography in the case of a composite object.

Chapter 3 presents a new 3D theory of CSI that casts the technique as a 3D linear filtering process that is characterised by the 3D point spread function (PSF) in the space domain or equivalently the transfer function in the frequency domain or k -space. From this theory, the 3D PSF was computed for an ideal system. It was shown that a smoothly varying object could be considered to be a “foil – like” surface and the 3D PSF convolved with this surface would replicate 3D fringe pattern. Reflection from the foil surface depended on Fresnel reflection coefficient and for each material a particular phase would be introduced in the interference fringe pattern. Therefore, a material dependent height offset is observed while measuring surface topography with CSI.

In Chapters 4&5 the polarising properties of the sample surfaces are investigated to determine the height offset introduced by different materials. Microellipsometry and CSI configurations based on microellipsometry with laser and LED illuminations were described. In both of these techniques, the phase difference between the illuminations with orthogonal linear polarisation states was measured. It was shown that the measured height offset is within experimental noise (of the order of 3 nm) when compared to ellipsometric measurement of the same surfaces. Microellipsometry is a single point technique and to build an absolute surface topography, lateral scanning of the entire surface is required. The titled illumination CSI configuration provides a whole-field method of height offset measurement. The surface tilt, however, can affect the measurement since, for a tilted surface light may not be collected by the objective.

A new configuration overcomes these difficulties. In Chapter 5, a novel method of polarisation sensitive CSI (PS-CSI) set-up with rotationally symmetric orthogonal circular polarised LED light was described. A detailed analysis of the height offset measurement and compensation was also presented. Here, two samples, each containing two different materials were investigated. Four different materials were investigated with three metals gold, silver and aluminium and a dielectric, glass. The complex refractive indices of these materials are measured by this technique and subsequently, the height offsets are computed, both of which were found to closely match ellipsometric measurements. As discussed in Section 4.2.2, the discrepancy in real part of the refractive index did not affect the height compensation since the predominant contribution in the height offset results from the imaginary part of the refractive index.

The new PS-CSI configuration retains the attractive features of high vertical and lateral resolutions of the CSI set-up and compared to previous tilted illumination CSI set-ups in Chapter 4, has high SNR. It was noted in this work that for systems of large numerical aperture the polarisation state is significantly altered by transmission through the objective and the effect of the lens must be calibrated using an object of known refractive index. In Chapter 5, a method to do this is explained and subsequently, PS-CSI can be used to map the refractive indices of unknown surfaces and to compensate for associated height offset without *a-priori* knowledge of the refractive indices of the materials within sample.

Although the potential of PS-CSI has been demonstrated for a limited number of planar samples there are a number of areas that require further attention, which are discussed in the following section.

6.2 FUTURE WORK

The future works proposed on these measurement techniques are subdivided into two parts. The first part (section 6.2.1 – 6.2.3) discusses improvements to the existing technique while the second part (section 6.2.4) discusses an exciting application of PS-CSI.

6.2.1 THE EFFECT OF SAMPLE TILT

Although it was stated that a significant advantage of the PS-CSI method over the tilted illumination technique originally proposed by Leonhardt *et al* was its ability to measure the refractive index of tilted surfaces, due to time constraints the author was unable to demonstrate or put this into practice [1, 2]. The results presented are strictly only true for a surface whose normal is co-linear with the optical axis of the objective. In this case all of the illuminating rays are collected by the objective and the resultant phase change is the weighted sum of all the various contributions across the whole aperture as discussed in Chapter 4. If the sample is tilted however, only a portion of the illuminating rays are collected by the objective as illustrated in Figure 6.1.

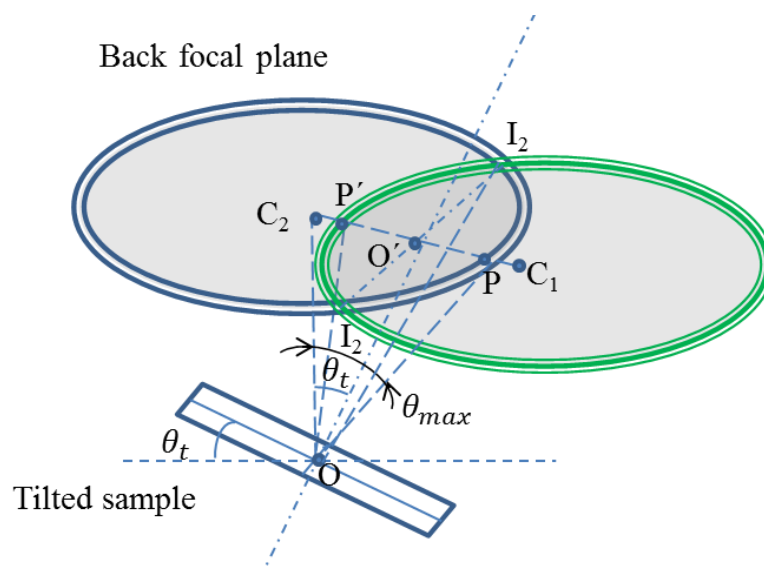


Figure 6.1 Shift of light cone for a tilt in the sample at the back focal plane

Here the spatial frequencies that define the illuminating rays in the back focal plane of the objective lie within the bounds of the blue circle, while those that define the scattered rays lie within the green circle. It is noted that only those rays that lie within the intersection of these rays go on to form the interference image. It is clear that a weighting function that is applied to the spatial frequencies and hence the phase difference between the block and the pass cases depends on the surface tilt. With the assumption that the phase change due to the material properties is less than that due to changes in surface height, the local gradient can be found and in principle, the height can be compensated accordingly.

The process of tilt compensation is quite complex however. Care must be taken to include both the geometric weighting shown in Figure 6.1 and the effects of transmission through the objective that was found to significantly change the polarisation state of the marginal rays (at the edge of the aperture) as described in Chapter 6. Since the latter depends on the (unknown) geometry of the objective, it is proposed that the combined effect is calibrated using a known metallic sample such as a sphere.

6.2.2 LATERAL RESOLUTION

Chapter 3 presented a 3D linear model of CSI in which the method was treated as a linear filtering operation applied to the “foil model” of the surface. The filter was characterised by the PSF in the space domain or equivalently by the TF in the frequency domain. The foundation of this theory is the scalar diffraction theory defined by the Helmholtz equation. It was shown that an ideal CSI where the full aperture of the objective is exploited for illumination and observation results in a PSF that resembles a cigar shaped packet of fringes (Figure 3.6 in Chapter 3). The lateral dimensions of the PSF effectively define the lateral resolution while the axial resolution is set by the fringe spacing (half the effective wavelength) together with the phase discrimination of the system.

It is clear however, that the PS-CSI method does not generally exploit the full aperture of the objective as shown in figures 5.4(a) and 5.4(b). For the pass case there is a small role off of the response at the edge of the aperture, however, this is not expected to affect the resolution significantly. For the block case the centre of the aperture does not contribute to the measurement and the resolution is expected to be reduced accordingly. Once again, time constraints prevented a full vector analysis of the PS-CSI configuration and it remains as an objective for further work. Once again it is noted that in order to calculate this,

however, the polarising characteristics of the objective must be taken into account and some sort of calibration method (for example a metallic sphere measurement) should be undertaken for this purpose.

6.2.3 MULTIPLE SCATTERING

Gao *et al* in their conference proceedings show with a simple ray trace analysis using a silicon V-groove that CSI tends to overestimate the surface roughness [3, 4]. To illustrate the point, a ray-trace incident on a V-groove and the topography estimated is shown in Figure 6.1. It can be seen that an inverted “V” is measured at the bottom of the groove. Since dents or scratches surfaces are likely to take the form of small grooves as shown in Figure 6.2, this type of error would result in an overestimate of surface height.

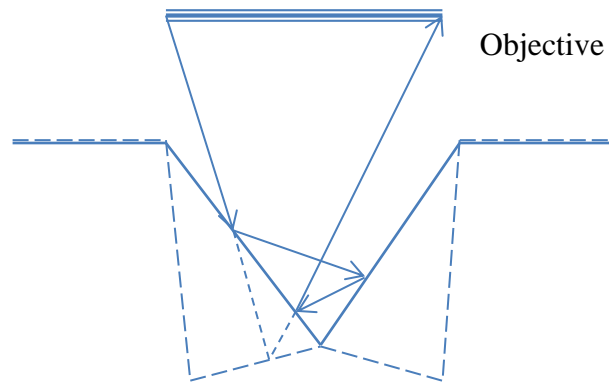


Figure 6.2 Actual V-groove (solid) with overestimated V-groove (dashed)

With PS-CSI the polarisation state must be considered. It is clear that with each reflection the phase and height offset will increase. Furthermore, it is noted that with each reflection the polarity of the polarisation would change (i.e. right handed becomes left handed) and this will have a profound effect on the ratio of block to pass analytic functions ($R_{expt}^{material}$ in Section 5.2.3). With an even number of reflections the polarity of the circular polarisation would change but with odd number of reflection, polarisation would remain the same, but in both cases surfaces will be overestimated due to multiple scattering. This will change the intensity and phase resulting in a measurement with significant error.

To remove this error one needs to first carry out estimates (simulations) of topography errors possible due to simple structures such as V-grooves (as shown in Figure 6.2) or trenches. Secondly, these areas with dents or scratches need to be separated out as “regions of

interest” and with the knowledge of their height difference, quantitatively, the structure of defect areas can be identified. With the structure, a ray-trace model can be created from which the number of scattering events can be computed. At each scattering point on the metal surface, a phase offset will be introduced and their sum provides the total phase to be compensated. In this way a surface model can be built to explain the PS-CSI measurements.

6.2.4 GRAIN ORIENTATION MEASUREMENT

Crystalline materials such as metal alloys form a certain lattice structure such as bcc or fcc and their grain boundary orientation and uniformity provide valuable information about the structural integrity of the parts made with them. Different methods such as orientation imaging microscopy and polarisation microscopes have been applied to image individual grains and grain boundaries [5, 6]. As mentioned in Chapter 5, the polarisation microscope developed by Inoué, Shribak and Oldenbourg has a crossed circular polariser configuration that is similar to PS-CSI [7]. Operating in a reflective mode, this technique can detect the grain structure with appropriate grain boundaries with a lateral resolution of the order of micrometre of anodised aluminium by measuring birefringence using a circularly polarised light [7]. With PS-CSI similar methodology is used to unravel the height offset. In principle, therefore, it should be able to detect the grain structures and measure the surface height of a particular grain. It is proposed that this information could be used to investigate deformation of ductile metals.


REFERENCE

1. K. Leonhardt, U. Droste and H. Tiziani, "Interferometry for ellipso-height-topometry Part 1: Coherence scanning on the base of spatial coherence", *Optik - International Journal for Light and Electron Optics*, 113, 12 (2003), 513-519.
2. K. Leonhardt, "Interferometry for ellipso-height-topometry Part 2: Measurement of the ellipsometric data, material identification, and correction of the measured height", *Optik*, 121 (2010), 623-632.
3. F. Gao, J. M. Coupland and J. Petzing, "V-Groove Measurements using White Light Interferometry", *Photon06*, Manchester (2006).
4. F. Gao, R. K. Leach, J. Petzing and J. Coupland, "Surface measurement errors using commercial scanning white light interferometers", *Measurement science and technology*, 19, 015303 (2008).
5. Brent L Adams, "Orientation imaging microscopy: application to the measurement of grain boundary structure", *Material Science and Engineering*, A166 (1993). 59-66.
6. S. Inoué, "Exploring Living Cells and Molecular Dynamics with Polarized Light Microscopy" in *Optical imaging and microscopy*, Peter Török and Fu-Jen Kao eds., (Springer, 2007)
7. R. Oldenbourg, "A new view on polarization microscopy", *Nature Communication*, 381 (1996), 811-812.


APPENDIX

LED

Details of the LED are copied from Thorlabs catalogue.



LED with Ball Lens




LED635L

Description

The LED635L emits light with a spectral output centered at 635 nm. This LED is encased in a TO-39 package with a Ball Lens.

Specifications



Electrical Specifications		
	Typical	Maximum Ratings
Power Dissipation	-	500 mW
DC Forward Current	350 mA	500 mA
Forward Voltage @ 350 mA	2.3 V	3.0 V
Reverse Voltage	-	10.0 V
Operating Temperature	-	-55 to 100° C
Storage Temperature	-	-55 to 100° C

*Note: All maximum measurements specified are at 25° C.

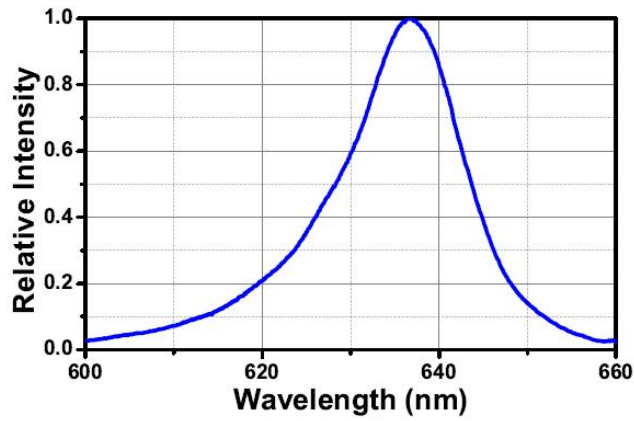
Optical Specifications	
	Typical
Center Wavelength	635 nm
FWHM	15 nm
Half Viewing Angle	7°
Optical Power (Minimum/Typical) @ 350 mA	80 mW/170 mW

Soldering Specifications	
	Conditions
Lead Soldering Temperature	260° C maximum, 1/16 inch (1.6 mm) from case for 5 seconds with soldering iron

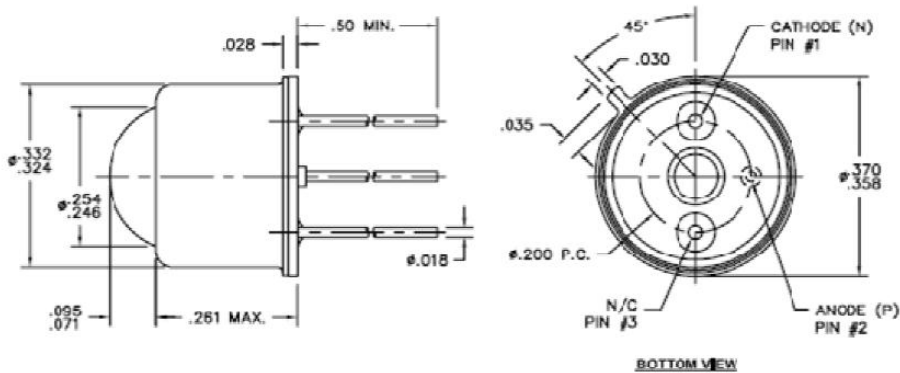
Cleaning Solvents							
Solvent	Ethyl Alcohol	Isopropyl Alcohol	Propanol	Acetone	Chloroseen	Trichloroethylene	MKS
Approved	Yes	Yes	Yes	No	No	No	No

(0)1353-65440
22513486

Typical Spectral Intensity Distribution



Drawing



US, Canada, & South America: +1-973-300-3000 | Europe: +49 (0) 8131-5956-0 | UK & Ireland: +44 (0)1353-65440
 France: +33 (0) 970 44 48 44 | Scandinavia: +46-31-733-30-00 | Japan & Asia: +81-3-5979-8889 | China: +86 (0)21-32513486

Specifications Subject to Change without Notice

May 2, 2011
 22351-S01, Rev A

MIRAU OBJECTIVE

The Mirau objective (100X Nikon CF IC Epi Plan DI Interferometry Objective) details are obtained from Edmund optics website. (<http://www.edmundoptics.com/microscopy/infinity-corrected-objectives/nikon-interferometry-objectives/2797>)

Magnification	100x
Numerical Aperture NA	0.7
Working Distance (mm)	2
Focal Length FL (mm)	2
Resolving Power (μm)	0.4
Depth of Focus (μm)	0.56
Field of View, 25 Diameter Field Eyepiece (mm)	0.25
Field of View, 20 Diameter Field Eyepiece (mm)	0.2
Field of View, 2/3" Sensor (mm)	0.011 x 0.08
Field of View, 1/2" Sensor (mm)	0.08 x 0.06
Mount	C-Mount
Mounting Threads	RMS
Weight (g)	200
RoHS	Compliant

FRESNEL RHOMB

Details obtained from Comar Optics catalogue.

8.6 Achromatic retarders

[Customise](#) 

The Fresnel rhomb is unique among retarders in giving a fractional-wave retardation nearly independent of wavelength, the variation due to change of index with wavelength being less than $\pm 1\%$ through the visible (450-700nm) and within $\pm 4\%$ throughout the range of transparency (350-2500nm). The variation with angle is also small (less than $\pm 6\%$ over $\pm 5^\circ$) and spurious stress birefringence is reduced by use of a fine-annealed grade of glass. The single (quarter-wave) rhomb gives an output parallel to the input but laterally displaced. The double (half-wave) rhomb has input and output coaxial.

Specification

Aperture	16 x 16mm
Lateral offset (single rhomb)	21.6mm
Angles	$55^\circ 20' \pm 5'$
Material	BK7 (see p.2)

Catalogue No.	Type	Length (mm)
01 JR 16	single ($\lambda/4$)	31.3
02 JR 16	double ($\lambda/2$)	62.6

